Biosynthesis

Green synthesis of iron oxide nanoparticles for biomedical application and environmental remediation: a review

Biomaterials

Bioadsorption of lead(II) over the pulp of *Acrocomia aculeata*

Amino acids

Variability levels of selected amino acids among mandarins produced in Uruguay

Potential model

Effect of the deformation parameter on the nonrelativistic energy spectra of the *q*-deformed Hulthen-quadratic exponential-type potential

UNIVERSIDADE ESTADUAL PAULISTA

Reitor

Pasqual Barretti

Vice-Reitora

Maysa Furlan

Pró-Reitora de Graduação

Celia Maria Giacheti

Pró-Reitora de Pós-Graduação

Maria Valnice Boldrin

Pró-Reitor de Pesquisa

Edson Cocchieri Botelho

Pró-Reitor de Extensão Universitária e Cultura

Raul Borges Guimarães

Pró-Reitor de Planejamento Estratégico e Gestão

Estevão Tomomitsu Kimpara

INSTITUTO DE QUÍMICA

Diretor

Sidney José Lima Ribeiro

Vice-Diretora

Denise Bevilaqua

Editorial Team

Editorial

Looking forward to better days coming, the editors of Eclet. Quim. Journal cordially welcome the readers of our journal to the fourth edition of this year which contains publications of excellent level. We wish you a pleasant read of the findings described in the articles.

Starting the last issue of 2021 there is a review study on embodied ferrous oxide nanoparticles (IONPs) formed from plant materials. These particles have distinctive properties - biocompatibility, low toxicity, catalytic behavior and multi reaction mechanism - which enabled several biomedical applications. This review significantly summarized the synthesis, optimum conditions and characterization techniques involved in the synthesis of IONPs and presented in great detail their uses as antimicrobial and anticancer therapeutic agents. In sequence appears a study on the adsorption of lead in aqueous solution onto *Acrocomia aculeata* pulp. By adding sodium azide to the solution, the pulp's thermal stability increases to 200 °C. The removal efficiency reached a maximum of 91.9% when a solution of 50 ppm of lead was placed in contact with the pulp for 30 min. The column experiments revealed a theoretical maximum adsorption capacity of 11.97 mg g^{-1}. Research on the nutraceutical properties of mandarins produced in Uruguay raised great interest by the presence of free amino acids in addition to their high vitamin C content and flavonoids. A targeted metabolomics study in 'Ellendale', 'Willowleaf' and 'Page' mandarin varieties was performed; the concentration levels of the amino acids separated well apart the three varieties. The amino acids with higher levels in mature samples were histidine, asparagine, glutamine, and glutamic acid. Another research obtained an approximate solution of the Schrödinger equation for the q-deformed Hulthen-quadratic exponential-type potential model within the framework of the Nikiforov–Uvarov method. This method finds many applications in quantum chemistry, atomic and molecular physics. The authors analyzed in detail the graphical and numerical effect of the deformation parameters and other potential parameters on the energy spectra of the system. The energy eigenvalues expressions agreed with that obtained in literature.

The Editor and the team of Eclet. Chem. J. are immensely grateful to the authors and reviewers' dedication, who spared no effort for the successful completion of this issue.

Assis Vicente Benedetti
Editor-in-Chief of EQJ

Citation databases: Ecletica Quim. J. is indexed

*Click on the images to follow the links.
EBSCO has no link available. The address is for subscribers only.

INSTRUCTIONS FOR AUTHORS

BEFORE YOU SUBMIT

1. Check Eclet. Quim. J.'s focus and scope

Eclética Química Journal is a peer-reviewed quarterly publication of the Institute of Chemistry of São Paulo State University (UNESP). It publishes original researches as articles, reviews and short reviews in **all areas of Chemistry**.

2. Types of papers

  a. Original articles
  b. Reviews
  c. Short reviews
  d. Communications
  e. Technical notes
  f. Articles in education in chemistry and chemistry-related areas

Manuscripts submitted for publication as full articles and communications must contain original and unpublished results and should not have been submitted elsewhere either partially or whole.

a. Original articles

The manuscript must be organized in sections as follows:

1. Introduction
2. Experimental
3. Results and Discussion
4. Conclusions
References

Sections titles must be written in bold and sequentially numbered; only the first letter should be in uppercase letter. Subsections, numbered as exemplified, should be written in normal and italic letters; only the first letter should be in uppercase letter.

Example:

1. Introduction
1.1 History

2. Experimental
2.1 Surface characterization
2.1.1 Morphological analysis

b. Reviews

Review articles should be original and present state-of-the-art overviews in a coherent and concise form covering the most relevant aspects of the topic that is being revised and indicate the likely future directions of the field. Therefore,

before beginning the preparation of a Review manuscript, send a letter (one page maximum) to the Editor with the subject of interest and the main topics that would be covered in the Review manuscript. The Editor will communicate his decision in two weeks. Receiving this type of manuscript does not imply acceptance to be published in **Eclet. Quím. J.** It will be peer-reviewed.

c. Short reviews

Short reviews should present an overview of the state-of-the-art in a specific topic within the scope of the Journal and limited to 5,000 words. Consider a table or image as corresponding to 100 words. Before beginning the preparation of a Short Review manuscript, send a letter (one page maximum) to the Editor with the subject of interest and the main topics that would be covered in the Short Review manuscript.

d. Communications

Communications should cover relevant scientific results and are limited to 1,500 words or three pages of the Journal, not including the title, authors' names, figures, tables and references. However, Communications suggesting fragmentation of complete contributions are strongly discouraged by Editors.

e. Technical notes

Descriptions of methods, techniques, equipment or accessories developed in the authors' laboratory, as long as they present chemical content of interest. They should follow the usual form of presentation, according to the peculiarities of each work. They should have a maximum of 25 pages, including figures, tables, diagrams, etc.

f. Articles in education in chemistry and chemistry-correlated areas

Research manuscript related to undergraduate teaching in Chemistry and innovative experiences in undergraduate and graduate education. They should have a maximum of 25 pages, including figures, tables, diagrams, and other elements.

3. Special issues

Special issues with complete articles dedicated to Symposia and Congresses and to special themes or in honor of scientists with relevant contributions in Chemistry and correlate areas can be published by **Eclet. Quim. J.** under the condition that a previous agreement with Editors is established. All the guides of the journal must be followed by the authors.

4. Approval

Ensure all authors have seen and approved the final version of the article prior to submission. All authors must also approve the journal you are submitting to.

ETHICAL GUIDELINES

Before starting the submission process, please be sure that **all ethical aspects mentioned below were followed**. Violation of these ethical aspects may preclude authors from submitting or publishing articles in **Eclet. Quim. J.**

   a. Coauthorship: The corresponding author is responsible for listing as coauthors only researchers who have really taken part in the work, for informing them about the entire manuscript content and for obtaining their permission to submit and publish it.

b. Nonauthors: Explicit permission of a nonauthor who has collaborated with personal communication or discussion to the manuscript being submitted to **Eclet. Quím. J.** must be obtained before being cited.

c. Unbiased research: Authors are responsible for carefully searching for all the scientific work relevant to their reasoning irrespective of whether they agree or not with the presented information.

d. Citation: Authors are responsible for correctly citing and crediting all data taken from other sources. This requirement is not necessary only when the information is a result of the research presented in the manuscript being submitted to **Eclet. Chem. J.**

e. Direct quotations: The word-for-word reproduction of data or sentences as long as placed between quotation marks and correctly cited is not considered ethical deviation when indispensable for the discussion of a specific set of data or a hypothesis.

f. Do not cite: Master's Degree dissertations and PhD theses are not accepted; instead, you must cite the publications resulted from them.

g. Plagiarism: Plagiarism, self-plagiarism, and the suggestion of novelty when the material was already published are unaccepted by **Eclet. Quim. J.** Before reviewing a manuscript, the **Turnitin antiplagiarism software** will be used to detect any ethical deviation.

h. Simultaneous submissions of the same manuscript to more than one journal is considered an ethical deviation and is conflicted to the declaration has been done below by the authors.

i. Studies with humans or other animals: Before submitting manuscripts involving human beings, materials from human or animals, the authors need to confirm that the procedures established, respectively, by the institutional committee on human experimentation and Helsinki's declaration, and the recommendations of the animal care institutional committee were followed. Editors may request complementary information on ethical aspects.

COPYRIGHT NOTICE

PUBLICATION CHARGES

Eclética Química Journal is supported by the Institute of Chemistry/UNESP and publication is free of charge for authors.

MANUSCRIPT PREPARATION

COVER LETTER

We provide a template to help you prepare your cover letter. To download it, click **here**.

The cover letter MUST include:

1. Identification of authors

a. The authors' full names (they must be written in full and complete, separated by comma)

~~João M. José~~   Incorrect
~~J. M. José~~   Incorrect
João Maria José   Correct!

b. E-mail addresses and affiliations (**neither more nor less than two instances**) of all authors;
c. ORCID ID links;
d. A plus sign (+) indicating the corresponding author.

Example:

Author Full Name[1+], Author Full Name[2]

1. University, Faculty or Institute, City, Country.
2. Company, Division or Sector or Laboratory, City, Country.

+ Author 1: address@mail.com, ORCID: https://orcid.org/xxxx-xxxx-xxxx-xxxx
Author 2: address@mail.com, ORCID: https://orcid.org/xxxx-xxxx-xxxx-xxxx

2. Authors' contribution

We request authors to include author contributions according to CRediT taxonomy standardized contribution descriptions. CRediT (Contributor Roles Taxonomy) is a high-level taxonomy, including 14 roles, that can be used to represent the roles typically played by contributors to scientific scholarly output. The roles describe each contributor's specific contribution to the scholarly output.

a. Please, visit this link (https://casrai.org/credit/) to find out which role(s) the authors fit into;
b. Do not modify the role names; do not write "all authors" in any role. Do not combine two or more roles in one line.
c. If there are any roles that no author has engaged in (such as funding in papers that were not funded), write "Not applicable" in front of the name of the role;
d. Write the authors' names according to the **American Chemistry Society (ACS) citation style**.

Example:

Conceptualization: Foster, J. C.; O'Reilly, R. K.
Data curation: Varlas, S.; Couturaud, B.; Coe, J.; O'Reilly, R. K.
Formal Analysis: Foster, J. C.; Varlas, S.
Funding acquisition: Not applicable.

Investigation: Foster, J. C.; O'Reilly, R. K.
Methodology: Coe, J.; O'Reilly, R. K.
Project administration: O'Reilly, R. K.
Resources: Coe, J.
Software: Not applicable.
Supervision: O'Reilly, R. K.
Validation: Varlas, S.; Couturaud, B.
Visualization: Foster, J. C.
Writing – original draft: Foster, J. C.; Varlas, S.; Couturaud, B.; Coe, J.; O'Reilly, R. K.
Writing – review & editing: Foster, J. C.; Varlas, S.; Couturaud, B.; Coe, J.; O'Reilly, R. K.

4. Indication of reviewers

We kindly ask the authors to suggest **five** suitable reviewers, providing full name, affiliation, and email.

5. Other information

a. The authors must write one paragraph remarking the novelty and relevance of the work;
b. The corresponding author must declare, on behalf of the other authors, that the manuscript being submitted is original and its content has not been published previously and is not under consideration for publication elsewhere;
c. The authors must inform if there is any conflict of interest.

6. Acknowledgements and funding

Acknowledgements and funding information will be requested after the article is accepted for publication.

7. Data availability statement

A data availability statement informs the reader where the data associated with your published work is available, and under what conditions they can be accessed. Therefore, authors must inform if:

Data will be available upon request;
All dataset were generated or analyzed in the current study; or
Data sharing is not applicable.

MANUSCRIPT

We provide a template to help you prepare your manuscript. To download it, click **here**.

1. General rules

Only manuscripts written in English will be accepted. British or American usage is acceptable, but they should not be mixed. Non-native English speakers are encouraged to have their manuscripts professionally revised before submission.

Manuscripts must be sent in editable files as *.doc, *.docx or *.odt. The text must be typed using font style Times New Roman and size 12. Space between lines should be 1.5 mm and paper size A4, top and bottom margins 2.5 cm, left and right margins 2.0 cm.

All contributions must include an **abstract** (170 words maximum), **three to five keywords** and a **graphical abstract** (8 cm wide × 8 cm high).

Supplementary information: all type of articles accepts supplementary information (SI) that aims at complementing the main text with material that, for any reason, cannot be included in the article.

TITLE

The title should be concise, explanatory and represent the content of the work. The title must have only the first letter of the sentence in uppercase. The following are not allowed: acronyms, abbreviations, geographical location of the research, en or em dashes (which must be replaced by a colon). Titles do not have full point.

ABSTRACT

Abstract is the summary of the article. The abstract must be written as a running text not as structured topics, but its content should present background, objectives, methods, results, and conclusion. It cannot contain citations. The text should be written in a single paragraph with a **maximum of 170 words**.

KEYWORDS

Keywords are intended to make it easier for readers to find the content of your text. As fundamental tools for database indexing, they act as a gateway to the text. The correct selection of keywords significantly increases the chances that a document will be found by researchers on the topic, and consequently helps to promote the visibility of an article within a myriad of publications.

FIGURES, TABLES AND EQUATIONS

Figures, tables and equations must be written with initial capital letter followed by their respective number and period, in bold, without adding zero "**Table 1**", preceding an explanatory title. Tables, Figures and Equations should appear after the first citation and should be numbered according to the ascending order of appearance in the text (1, 2, 3...).

Figures, tables, schemes and photographs already published by the same or different authors in other publications may be reproduced in manuscripts of **Eclet. Quim. J.** only with permission from the editor house that holds the copyright.

Nomenclature, abbreviations, and symbols should follow IUPAC recommendations.

DATA AVAILABILITY STATEMENT

The data availability statement informs the reader where the data associated with your work is available, and under what conditions they can be accessed. They also include links (where applicable) to the data set.

a. The data are available in a data repository (cite repository and the DOI of the deposited data);
b. The data will be available upon request;
c. All data sets were generated or analyzed in the current study;
d. Data sharing is not applicable (in cases where no data sets have been generated or analyzed during the current study, it should be declared).

GRAPHICAL ABSTRACT

The graphical abstract must summarize the manuscript in an interesting way to catch the attention of the readers. As already stated, it must be designed with 8 cm wide × 8 cm high, and a 900-dpi resolution is mandatory for this journal. It must be submitted as *.jpg, *.jpeg, *.tif or *.ppt files as supplementary file.

We provide a template to help you prepare your GA. To download it, click **here**.

SUPPLEMENTARY INFORMATION

When appropriate, important data to complement and a better comprehension of the article can be submitted as Supplementary File, which will be published online and will be made available as links in the original article. This might include additional figures, tables, text, equations, videos or other materials that are necessary to fully document the research contained in the paper or to facilitate the readers' ability to understand the work.

Supplementary material should be presented in appropriate .docx file for text, tables, figures and graphics. All supplementary figures, tables and videos should be referred in the manuscript body as "Table S1, S2…", "Fig. S1, S2…" and "Video S1, S2 …".

At the end of the main text the authors must inform: This article has supplementary information.

Supplementary information will be located following the article with a different DOI number from that of the article, but easily related to it.

CITATION STYLE GUIDE

From 2021 on, the **Eclet. Quim. J.** will follow the **ACS citation style**.

Indication of the sources is made by authorship and date. So, the reference list is organized alphabetically by author.

Each citation consists of two parts: the in-text citation, which provides brief identifying information within the text, and the reference list, a list of sources that provides full bibliographic information.

We encourage the citation of primary research over review articles, where appropriate, in order to give credit to those who first reported a finding. Find out more about our commitments to the principles of San Francisco Declaration on Research Assessment (DORA).

What information you must cite?

    a. Exact wording taken from any source, including freely available websites;
    b. Paraphrases of passages;
    c. Summaries of another person's work;
    d. Indebtedness to another person for an idea;
    e. Use of another researchers' work;
    f. Use of your own previous work.

You do not need to cite **common knowledge**.

Example:

Water is a tasteless and odorless liquid at room temperature (common knowledge, no citation needed)

In-text citations

You can choose the cite your references within or at the end of the phrase, as showed below.

Within the cited information:

One author: Finnegan states that the primary structure of this enzyme has also been determined (2004).
Two authors: Finnegan and Roman state that the structure of this enzyme has also been determined (2004).
Three or more authors: Finnegan et al. state that the structure of this enzyme has also been determined (2004).

At the end of the cited information:

One author: The primary structure of this enzyme has also been determined (Finnegan, 2004).
Two authors: The primary structure of this enzyme has also been determined (Finnegan and Roman, 2004).
Three or more authors: The primary structure of this enzyme has also been determined (Finnegan et al., 2004).

If you need to cite more than one reference in the same brackets, separate them with semicolon and write them in alphabetic order:

The primary structure of this enzyme was determined (Abel et al., 2011; Borges, 2004; Castro et al., 2021).

Bibliographic references

Article from scientific journals
Foster, J. C.; Varlas, S.; Couturaud, B.; Coe, J.; O'Reilly, R. K. Getting into Shape: Reflections on a New Generation of Cylindrical Nanostructures' Self-Assembly Using Polymer Building Block. *J. Am. Chem. Soc*. **2019**, *141* (7), 2742−2753. https://doi/10.1021/jacs.8b08648

Book
Hammond, C. *The Basics of Crystallography and Diffraction*, 4th ed.; International Union of Crystallography Texts on Crystallography, Vol. 21; Oxford University Press, 2015.

Book chapter
Hammond, C. Crystal Symmetry. In *The Basics of Crystallography and Diffraction*, 4th ed.; International Union of Crystallography Texts on Crystallography, Vol. 21; Oxford University Press, 2015; pp 99−134.

Book with editors
Mom the Chemistry Professor: Personal Accounts and Advice from Chemistry Professors Who Are Mothers, 2nd ed.; Woznack, K., Charlebois, A., Cole, R. S., Marzabadi, C. H., Webster, G., Eds.; Springer, 2018.

Website
ACS Publications Home Page. https://pubs.acs.org/ (accessed 2019-02-21).

Document from a website
American Chemical Society, Committee on Chemical Safety, Task Force for Safety Education Guidelines. *Guidelines for Chemical Laboratory Safety in Academic Institutions*. American Chemical Society, 2016. https://www.acs.org/content/dam/acsorg/about/governance/committees/chemicalsafety/publications/acs-safety-guidelines-academic.pdf (accessed 2019-02-21).

Conference proceedings
Nilsson, A.; Petersson, F.; Persson, H. W.; Jönsson, H. Manipulation of Suspended Particles in a Laminar Flow. In Micro Total Analysis Systems 2002, Proceedings of the µTAS 2002 Symposium, Nara, Japan, November 3−7, 2002; The Netherlands, 2002; pp 751−753. https://doi.org/10.1007/978-94-010-0504-3_50

Governmental and legislation information
Department of Commerce, United States Patent and Trademark Office. Section 706.02 Rejection of Prior Art [R-

07.2015]. *Manual of Patent Examining Procedure (MPEP)*, 9th ed., rev. 08.2017, last revised January 2018. https://www.uspto.gov/web/offices/pac/mpep/s706.html#d0e58220 (accessed 2019-03-20).

Patent
Lois-Caballe, C.; Baltimore, D.; Qin, X.-F. Method for Expression of Small RNA Molecules within a Cell. US 7 732 193 B2, 2010.

Streaming data
American Chemical Society. Game of Thrones Science: Sword Making and Valyrian Steel. *Reactions*. YouTube, April 15, 2015. https://www.youtube.com/watch?v=cHRcGoje4j4 (accessed 2019-02-28).

For more information, you can access the ACS Style Quick Guide and the Williams College LibGuides.

SUBMITTING YOUR MANUSCRIPT

The corresponding author should submit the manuscript online by clicking **here**. If you are a user, register by clicking **here**.

At the **User home** page, click in **New submission**.

In Step 1, select a section for your manuscript, verify one more time if you followed all these rules in **Submission checklist**, add Comments for the Editor if you want to, and click Save and continue.

In Step 2, you will **upload your manuscript**. Remember it will pass through a double-blind review process. So, do not provide any information on the authorship.

In Step 3, enter **submission's metadata**: authors' full names, valid e-mail addresses and ORCID ID links (with "http" not "https"). Add title, abstract, contributors and supporting agencies, and the list of references.

In Step 4, upload the **cover letter**, the **graphical abstract** and other **supplementary material** you want to include in your manuscript.

In Step 5, you will be able to check all submitted documents in the **File summary**. If you are certain that you have followed all the rules until here, click in **Finish submission**.

REVIEW PROCESS

The time elapsed between the submission and the first response of the reviewers is around three months. The average time elapsed between submission and publication is around seven months.

Resubmission (manuscripts "rejected in the present form" or subjected to "revision") must contain a letter with the responses to the comments/criticism and suggestions of reviewers/editors should accompany the revised manuscript. All modifications made to the original manuscript must be highlighted.

If you want to check our Editorial process, click **here**.

EDITOR'S REQUIREMENTS

Authors who have a manuscript accepted in **Eclet. Quim. J.** may be invited to act as reviewers.

Only the authors are responsible for the correctness of all information, data and content of the manuscript submitted to **Eclet. Quim. J.** Thus, the Editors and the Editorial Board cannot accept responsibility for the correctness of the material published in **Eclet. Quim. J.**

Proofs

After accepting the manuscript, **Eclet. Quim. J.** technical assistants will contact you regarding your manuscript page proofs to correct printing errors only, i.e., other corrections or content improvement are not permitted. The proofs shall be returned in three working days (72 h) via email.

Appeal

Authors may only appeal once about the decision regarding a manuscript. To appeal against the Editorial decision on your manuscript, the corresponding author can send a rebuttal letter to the editor, including a detailed response to any comments made by the reviewers/editor. The editor will consider the rebuttal letter, and if dimmed appropriate, the manuscript will be sent to a new reviewer. The Editor decision is final.

Contact

If you have any question, please contact our team:

Prof. Assis Vicente Benedetti
Editor-in-Chief
ecletica@journal.iq.unesp.br

Letícia Amanda Miguel and Jéssica Odoni
Technical support
ecletica@ctrlk.com.br

SUMMARY

REVIEW ARTICLE

ORIGINAL ARTICLES

Green synthesis of iron oxide nanoparticles for biomedical application and environmental remediation: a review

Sunday Adewale Akintelu[1,2] , Abel Kolawole Oyebamiji[2,3] , Seyifunmi Charles Olugbeko[4] , Aderonke Similoluwa Folorunso[5+]

1. Beijing Institute of Technology, School of Chemistry and Chemical Engineering, Beijing, China.
2. Ladoke Akintola University of Technology, Department of Pure and Applied Chemistry, Ogbomoso, Nigeria.
3. Adeleke University, Department of Basic Sciences, Ede, Nigeria.
4. Ladoke Akintola University of Technology, Department of Agricultural Economics, Ogbomoso, Nigeria.
5. Louisiana State University, Department of Chemistry, Louisiana, United States of America.

+Corresponding author: Aderonke Similoluwa Folorunso, Phone: +2348136872649, Email address: folorunsoaderonkesimi@gmail.com

---

ARTICLE INFO

ABSTRACT: Ferrous oxide nanoparticles (IONPs) formed from plant materials have been considered as chemically friendly materials and have offered extensive applications. The distinctive features of IONPs, such as biocompatibility, low toxicity, catalytic behavior and multi reaction mechanism, have embodied them as good candidate for several biomedical applications. However, the synthesis of IONPs using plant extracts is gaining high popularity and recommendations because plant extracts could act as reducing and stabilizing agents during the process of synthesis. Furthermore, the biological method of synthesizing IONPs using plant extract offer some benefits, such as being simple, economic, environmentally friendly and require less energy when compared with both physical and chemical methods of synthesis. Hence, this review significantly summarized the synthesis, optimum conditions and characterization techniques involved in the synthesis of IONPs using several plant extracts. Consequently, comprehensive information about the applications of green synthesized IONPs as antimicrobial and anticancer therapeutic agents were well presented. The effectiveness of IONPs in environmental treatment of effluent containing dyes and other toxic agents were also properly discussed.
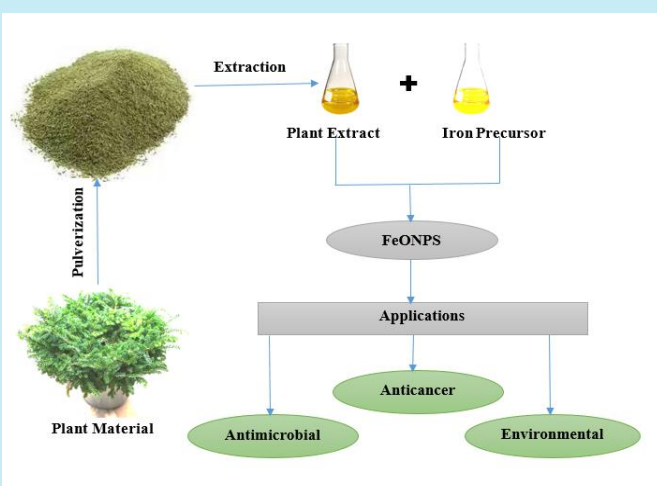
CONTENTS

1. Introduction

Nanoscience and nanotechnology have emerged as an innovative field of research with numerous applications in technological and scientific aspects including medical sciences, applied sciences, material science, catalysis, electronics, biofilm and biotechnology (Assa et al., 2016). The smaller sizes of nanoparticles (NPs) compared with large biomolecules have been reported to enhance their interactions with several biological molecules, which may revolutionize microbial treatment and cancer diagnosis (Alharbi and Al-sheikh, 2014). Among the various kinds of metals and metal oxides NPs, iron oxide NPs are one of the most prominent metal oxide NPs. The exceptional attribute of ferrous oxide nanoparticles (IONPs) has widened its horizon and applications in medical sciences and many other industries, such as gas sensor, electrochemical, magnetic and energy storage (Vallabani and Singh, 2018). The superparamagnetic behavior of iron oxide NPs has promoted its extensive applications in several areas, such as imaging, drug delivery, targeting and biosensors. Furthermore, their unique properties, such as biocompatibility, potent magnetic, low toxicity and catalytic behavior, have contributed massively to its biomedical applications (Vallabani and Singh, 2018). Various types of IONPs, such as maghemite (γ-Fe$_2$O$_3$) hematite (α-Fe$_2$O$_3$) and magnetite (Fe$_3$O$_3$) NPs, have been reported as efficient therapeutic agents against several infections due to their morphological properties (Yadav and Fulekar, 2018). Physical and chemical methods like chemical precipitation, mineralization, sol-gel, flow injection,

microemulsion, hydrothermal technique, biomimetic precipitation, forced hydrolysis technique, sonochemical technique and electrochemical technique have been chosen for the synthesis of IONPs (Gebre and Sendeku, 2019). The biological methods of synthesizing metal and metal oxides have been regarded as the most preferred method due to its cost-effectiveness, safety and easy protocol of synthesis (El Shafey, 2020). However, the biological method of synthesizing IONPs is classified into two main parts; the first category involves the use of microorganisms such as algae, bacteria and fungi as reducing agent while the other form entails the use of plant extracts as reducing and stabilizing agents (Salem et al., 2019; Yew et al., 2020). The capability of plant extracts to function as good reducing and stabilizing agents by reducing particle size and improve reactivity was contributed to the general acceptance of biological synthesis of metal and metal oxides from plant sources (Akintelu and Folorunso, 2019a; Akintelu et al., 2019a; Bashir et al., 2019; Folorunso et al., 2019). Plant extracts used for the synthesis of metal and metal oxides have been reported to show better stability and more acquiescent to large scale production of NPs when compared with the biological approach of synthesis that uses microorganisms (Akintelu and Folorunso, 2019b; Akintelu et al., 2019b; Kamran et al., 2019). The effectiveness of plants extracts as good reducing and stabilizing agents are linked with the presence of biomolecules such as flavonoids, alkaloids, terpenoids, and other hydroxyl containing functional groups which coat the surface of the NPs, prevent agglomeration and aid the production of NPs with uniform particle size (Gunarani et al., 2019).

Therefore, this review primarily focuses on the recent developments in the biosynthesis of IONPs using plant extracts. The various methods used for the synthesis of IONPs were briefly discussed. The mechanism of formation of IONPs using plant extract, the techniques used for the characterization of IONPs were highlighted. Then, the application of biosynthesized IONPs in the biomedicine and environmental waste management is summarized.

2. Synthesis of IONPs

Many reports have shown that the application of IONPs depend largely on the method of synthesis used (Arsalani et al., 2019). The preparation method determines the size distribution, particle sizes, shape and surface morphology which further influenced their applications. Moreover, the preparation method has been reported as the determinant factor for the degree of structural defects and impurity level of IONPs (Roca et al., 2019). Several methods and protocols such as physical, chemical and biological have been designed for the synthesis of IONPs with desired morphological features and magnetic properties (Palma et al., 2018).

2.1 Physical methods

Physical methods are based on the use of electrical fields and some other physical phenomena as the reducing agent during the synthesis of IONPs. The most reoccurring one is particle growth, which is based on physical processes and top-down approach. Examples of such techniques are sonochemical, lithography, sputtering, microwaves irradiation and laser ablation. The sonochemical technique encompasses the sonication of an aqueous ferric solution at ambient conditions and in the presence of air (Nisticò, 2021). Ultrasounds generate irregular compression and expansion acoustic waves which cause the oscillation of the microbubbles (Wu et al., 2015). When the bubbles collapse a localized hot spot is formed at high temperature around 4500 °C and pressure of about 1000 bar which enhanced the conversion of iron precursors into IONPs (Pinkas et al., 2008). The IONPs produced via this technique have high stability and remarkable magnetic properties. Despite the aforementioned advantages it is difficult to control the shape of IONPs produced from this technique (Ali et al., 2016).

Microwaves irradiation approach uses an electromagnetic source with wavelength in the range of 1–103 mm as reducing agent (Nisticò, 2017). The

radiation during this process causes molecules to align with the external field to generate motion that produces internal heating. This process has the advantages of reduction in treatment time and energy consumption. Also purified IONPs are mostly obtained. Notwithstanding, a report has revealed that this technique is limited because IONPs produced have poor morphological features and low surface reactivity (Pascu et al., 2012).

The electrochemical technique encompasses the immersion of galvanic cell with two electrodes (usually made up of iron) into a saline solution (Nisticò, 2021). This process involves iron electro-oxidation and electrolysis of water at the anode, alongside water reduction at the cathode. The electrochemical technique is affected by parameters such as working distance between electrodes, pH, reaction time and temperature. These techniques allow easy control of particle size and IONPs with hydrophilic surfaces are usually obtained (Cabrera et al., 2008).

2.2 Chemical methods

The chemical approach of synthesizing IONPs depends on the growth of iron oxides from the liquid phase via the use of some chemical reagents. Among the several protocols and techniques used for the chemical method of synthesis such as co-precipitation, micro-emulsion, sol-gel and polyol-mediated technique, co-precipitation technique is the most common and simplest (Lenders et al., 2016; Pang et al., 2016). Co-precipitation entails the stoichiometric mixture of iron precursor in presence of a basic conditions, following the given reaction pathway (Eq. 1).

$$2Fe^{3+} + Fe^{2+} + 8OH^- \rightarrow Fe_3O_4 + 4H_2O \qquad (1)$$

Acidic iron ions (Fe^{3+} or Fe^{2+}) when introduced into basic solution precipitates to form IONPs because magnetite is poorly soluble in basic condition. The formation of magnetite or maghemite NPs using the co-precipitation route depends on the ratio of Fe^{3+} or Fe^{2+} used (Nisticò et al., 2017a). The temperature requirement for the co-precipitation route is in the range of (20–250 °C) (Franzoso et al., 2017; Nisticò, 2017b). The following parameters iron precursor and ratio used, ionic strength, temperature, stirring rate and pH influences the size and shape of IONPs synthesized via the co-precipitation technique (Yazdani and Seddigh, 2016). Co-precipitation technique has been reported as the famous chemical methods for

synthesizing IONPs with control size distribution and high yields. However, this process suffers from some disadvantages such as the use of hazardous chemical reagents and difficulties in controlling the shape IONPs (Nisticò et al., 2017a).

The micro-emulsion process is another form of chemical method. In this process iron precursor either in water or oil biphasic system is exploited in the presence of amphiphilic molecules in form of block copolymers or sometimes surfactants such as cetyl trimethyl ammonium bromide or polyvinyl pyrrolidone at the interface (Nisticò, 2017). As a result of the dual nature (i.e., occurrence of both hydrophilic head and hydrophobic tail) of the amphiphiles macro molecules, the species moved at the interface of the two immiscible phases form covalent bonds and also assemble themselves into supramolecular aggregates of various shapes (Nisticò, 2018). The micro-emulsion process has advantages of narrow size IONPs production and easy shape regulation. However, the process has some disadvantages, such as low yield, impure products and formation of agglomeration (Wu et al., 2015).

Sol–gel technique involves acid/based-catalyzed hydrolysis and condensation of precursors from colloidal solutions to produce condensed network of iron oxides (Nisticò et al., 2017b). Iron alkoxides or iron salts are the main precursor for this technique because they can easily react through hydrolysis or condensation to yield oxides (Lemine et al., 2012).

Polyol-mediated technique entail the use of polyols as the reducing and stabilizing agents to aid the shape and size control during the synthesis of IONPs (Nisticò, 2021). This process is based on spreading iron containing precursors such as alkoxides in liquid polyols and heat to its boiling point. A report has shown that IONPs synthesized by polyol-mediated techniques are highly crystalline and can be easily dispersed into polar media due to their hydrophilic surfaces. Conversely, this technique has the limitation of generating toxic byproducts (Wu et al., 2015).

2.3 Biological method

The biological method of synthesizing IONPs is classified into two major routes, namely microorganism and plant based IONPs synthesis.

2.3.1 Microorganism based IONPs synthesis

Synthesis of IONPs using microorganism has gained huge attention over the past few decades due to some advantages over conventional chemical and physical methods of synthesis. The advantages of microorganism based IONPs synthesis include relative abundance of microorganism, production of less toxic byproducts, consumption of less power and energy because synthesis is carried out at room temperature and it tolerates large scale production (Park et al., 2016). Microorganisms such as bacteria, algae, fungi and yeast have been used for the synthesis of IONPs via intracellular or extracellular mechanism. The intracellular mechanism involves the enzymatic reduction of metal ions or metal oxide ion via electrostatic bounding to the cell wall of microorganism, the ions diffused into the cell and cause some interaction with enzymes to form IONPs (Mukherjee, 2017). The extracellular mechanism entails the enzymatic reduction of iron ions, producing small size distribution and well dispersed NPs with genes, peptides or protein that function as reducing agents, which in turn stabilizes and prevent agglomeration of IONPs (Singh et al., 2016).

2.3.2 Plant based IONPs synthesis

This is the process of synthesizing IONPs using extracts obtained from parts of plants, such as back, leaves, root, shoot, stems or the whole plant. In general, the desired plant part is obtained, sorted and washed to remove any impurities (solid or particles), air dried, chopped/mercerized to provide good surface area for extraction (Bolade et al., 2018). The extraction of their chemical constituents is accomplished by soaking the air-dried plant part at room temperature or boiled at elevated temperature to obtain the desired amount of extract (Bolade et al., 2020). This depends on the successful extraction of bioactive constituents in plant extracts. These bioactive constituents (phenols, tannins, saponins, alkaloids, organic acids, flavonoids and vitamins) function as reducing agents during the IONPs synthesis by reacting with the iron precursor (iron chloride, iron nitrate or iron sulphate) to produce IONPs, which are further stabilized by the chemical constituent present in the extract (Sorbiun et al., 2018). Several studies have reported the use of water as extracting solvent in the extraction of bioactive components of plants during the synthesis of IONPs (Prabhakar et al., 2017). Leaves, peel, bark and fruits of green plants have been studied for the eco-friendly synthesis of IONPs, as showed in Tabs. 1 and 2. The methods of synthesizing iron oxide NPs are illustrated in Fig. 1.

Table 1. Characterization techniques of biosynthesized IONPs from some plant materials.

S/N	Plants name	Plants parts	SPR peak/nm	Band/nm Functional group prediction		Techniques for morphological assessment	Shape	Size	References
1	*Punica granatum*	Seeds	372	-	-	UV, XRD, EDX, SEM, AFM	Spherical	25–55	Bibi et al., 2019
2	*Magnifera indica*	Peel	250–280	3334	O-H	XRD, UV, FTIR, XPS, EDX	-	-	Desalegn et al., 2019
				2973	C-H				
				1654	C=O				
3	*Cynara cardunculus*	Leaf	-	3306	O-H	UV–Vis, XRD, FTIR, SEM	Semi-spherical	13.5	Ruíz-Baltazar et al., 2019
				1585	C=C				
4	*Tamarix aphylla*	Stem	390	-	-	XRD, UV, SEM-EDX, TEM	Spherical	-	Ahmad et al., 2020
5	*K. alvarezii*	Whole plant	457	1480	O-H	XRD, UV, FTIR, HRSEM, HRTEM, EDX	Hexagonal	10–30	Arularasu et al., 2018
6	*Moringa oleifera*	Leaf	448	3325	O-H	XRD, FTIR, SEM	Irregular spherical	18–20	Aisida et al., 2021
				1618	C=O				
				1401	C-N				
7	*Amaranthus dubius*	Leaf	214	3250	O-H	SEM, XRDUV, FTIR	Oval	58–530	Harshiny et al., 2015
				1634	C=O				
8	Rhamnella gilgitica	Leaf	341	2979	C-H	SEM, TEM, XRD, DLS, FT-IR, EDX, UV	Spherical	21–25	Iqbal et al., 2020
				1064	C-N				
9	*Terminalia bellirica*	fruit	300	3300–340	O-H	SEM, TEM, XRD, FTIR, UV	Spherical	21.32	Jagadeesan et al., 2019
				1600	C=O				
10	*Stevia rebaudiana*	Leaf	-	-	-	XRD, HRTEM, Fe-SEM, XPS, EDX,	Spherical	20	Khatami et al., 2019
11	*Centella asiatica*	whole plant	-	3416	O-H	TEM, SEM, FTIR, EDX,	Spherical	20–40	Poka et al., 2019
				1621	C=O				
				1387	C-N				
12	*Avecinnia marina*	Flower	298-301	3422	O-H	UV, FTIR, XRD	-	45.09	Karpagavinayagam and Vedhi, 2019
				2923	C-H				
				1630	C=O				
13	Green tea	Leaf		3440	O-H	SEM, EDS, XPS, FT-IR	Spherical	117	Lin et al., 2017
				1629	C=O				
14	Green tea	Leaf	550	-	-	UV, SEM, TEM	Spherical	4.96	Liu et al., 2019
15	*Psidium guavaja*	Leaf	315	3034–3366	O-H	FTIR, UV, SEM, XRD	Spherical	-	Madubuonu et al., 2019
				1669	C=O				
16	*Calliandra haematocephala*	leaf	-	3645	0-H	UV–Vis, XRD, FTIR, TEM, EDS	Spherical	85	Sirdeshpande et al., 2018
				2935	C-H				
				1662	C=C				
17	*Trigonella foenum-graecum*	Seed	387	3428	O-H	FTIR, UV, SEM, EDX		7–14	Radini et al., 2018
				2940	C-H				
				1756	C=O				
				1544	N-H				
									Continue…

No.	Plant	Part		Wavenumber	Bond	Techniques	Shape	Size	Reference
18	*Luffa acutangula*	Peel	-	3446	O-H	FTIR, XRD, SEM, EDX	Spherical	20–35	Cheera et al., 2016
18 / 19	*Luffa acutangula* / *P. guajava*	Peel / Leaf	- / -	2829 / 1605 / 1410	C-H / C=C / O-H	FTIR, XRD, SEM, EDX; XRD, SEM, TEM, HRTEM, EDX, FTIR	Spherical / Irregular	20–35 / 20–30	Cheera et al., 2016 / Rufus et al., 2019
19 / 20	*P. guajava* / *Rheum emodi*	Leaf / Root	- / 320	1640 / 3381	C=O / O-H	XRD, SEM, TEM, HRTEM, EDX, FTIR; XRD, UV, FESEM, TEM, EDX, FTIR, AFM, TGA, VSM	Irregular / Pyramidal	20–30 / 10–30	Rufus et al., 2019 / Sharma et al., 2020
20 / 21	*Rheum emodi* / *Citrus maxima*	Root / Peel	320 / -	2927 / 1614 / 3292	C-H / C=O / O-H	XRD, UV, FESEM, TEM, EDX, FTIR, AFM, TGA, VSM; TEM, EDS, XPS, FTIR, DLS	Pyramidal / Irregular	10–30 / 10–100	Sharma et al., 2020 / Wei et al., 2016
21 / 22	*Citrus maxima* / *Ruellia tuberosa*	Peel / Leaf	- / 405	2927 / 1638 / 3397	C-H / C=O / O-H	TEM, EDS, XPS, FTIR, DLS; DLS, UV, SEM-EDX, TEM, FTIR	Irregular / Rod	10–100 / 20–80	Wei et al., 2016 / Vasantharaj et al., 2019
22 / 23	*Ruellia tuberosa* / *Lawsonia inermis*	Leaf / Whole plant	405 / 224	1629 / 1114 / 3444	N-H / C=O / O-H	DLS, UV, SEM-EDX, TEM, FTIR; UV, SEM-EDX, FTIR	Rod / Spherical	20–80 / 150–200	Vasantharaj et al., 2019 / Chauhan and Upadhyay, 2019
23	*Lawsonia inermis*	Whole plant	224	2962 / 1606	C-H / N-H	UV, SEM-EDX, FTIR	Spherical	150–200	Chauhan and Upadhyay, 2019

Note. Thermogravimetric analysis (TGA), vibrating sample magnetometer (VSM), and atomic force microscopy (AFM).

Table 2. Applications of IONPs synthesized from plants extracts.

| S/N	Plants name	Plants part	Iron precursor	Applications	Activities	References
1	*Parkia speciosa Hassk*	Pod	$FeSO_4$	Photocatalytic activity	The results imply that the nanoparticles have potential use as photocatalysts, with applications in dye-containing wastewater degradation	Fatimah et al., 2020
2	*Eucalyptus robusta*	Leaf	$FeSO_4$	Antibacterial activity	The result potential antibacterial activity against tested organism, but more effectiveness was observed against gram positive bacteria (B. subtilis)	Vitta et al., 2020
3	*Skimma laureola*	Leaf	$FeCl_3$	Antibacterial activity	The result revealed the importance of biosynthesized Fe_2O_3−NPs against phytopathogen Ralstonia solanacearum in vitro and in plant	Alam et al., 2019
4	*Green and black tea*	Leaf	$FeCl_3$	Antimicrobial activity	These results showed that the synthesized NPs could be effective against infections caused by multiple drug resistant pathogens	Asghar et al., 2018
5	*Eucalyptus*	Leaf	$FeCl_3$	Phosphate removal	The study demonstrated that the formation of IONPs improved the efficiency of phosphate removal	Gan et al., 2018
6	*Amaranthus dubius*	Leaf	$FeCl_3$	Antibacterial activity	The study showed that IONPs enhanced the performance of microbial fuel cell	Harshiny et al., 2017
7	*plantain*	Peel	$FeCl_3$	Catalytic activity	The study demonstrates an eco-friendly approach to synthesizing IONPs as a good bio-catalyst for the treatment of effluent waste of industries	Buiyan et al., 2020
8	*Green tea*	Leaf	$FeCl_3$	Organic pollutant remediation	The particles showed effective catalytic activity for removal of organic contaminants	Kheshtzar et al., 2019
9	*Eucalyptus*	Leaf	$FeCl_3$	Catalytic activity	It displayed good efficiency in removing Cr (VI)	Liu et al., 2018
10	*Papaver somniferum*	Pod	$FeSO_4$	anti-cancer activity	Fe_2O_3 NPs displayed superior biocompatibility with human RBCs	Muhammad et al., 2019
11	*Chinese cabbage*	Leaf	$FeCl_2$	Antioxidant	The IONPs showed good synergistic antibacterial, anticandidal and antioxidant activity	Patra and Baek, 2017
12	*Aloe vera*	Leaf	$FeCl_2$	anti-cancer activity	The study reported important *in vitro* cytotoxicity assessments on MCF-7 breast cancer cell line	Rahmani et al., 2020
13	*Amaranthus spinosus*	Leaf	$FeCl_3$	Environmental remediation activities	The IONPs displayed a strong catalytic activity for decolorization of methylene blue and methyl orange	Muthukumar and Matheswaran, 2015
14	*Pisidium guajava*	Leaf	$FeCl_3$	Antibacterial	It is noteworthy that the biosynthesized IONPs are more efficient antibacterial agent	Madubuonu et al., 2020
15	*Murraya koenigii*	Leaf	$FeSO_4$	Hydrogen Production	The photosynthesized IONPs enhanced the production of hydrogen when compared with $FeSO_4$	Mohanraj et al., 2014
16	*Salvadora persica*	Bark	$FeSO_4$	Cytotoxic activity	The IONPs showed cytotoxicity against colon (HT-29) cancer cell lines at concentrations above 125 µg mL^{-1}	Miri et al., 2020
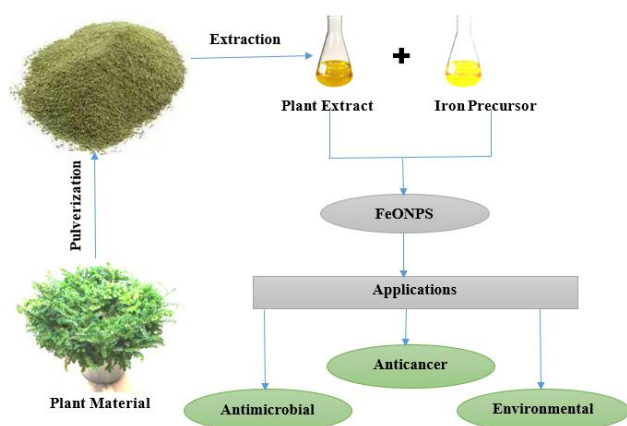
Figure 1. Green synthesis of iron oxide nanoparticles.

2.4 Possible mechanism for the synthesis of IONPs

Three stages, namely activation, growth and termination stage, are involved in the synthesis of IONPs from plant sources. Plant extracts serve as reducing agents for the bio-reduction of iron ion due to the chemical constituents found in plant extract. During synthesis, iron ions react with chemical constituents such as flavonoids, polyphenols and tannins via reduction and oxidation reactions. The electron rich biomolecules with (-OH) functional groups has the efficiency of reducing the iron ions (Fe^{2+} or Fe^{3+}) from divalent or trivalent oxidation state depending on the iron precursor used to metallic form Fe^0. This zerovalent iron will then be converted to IONPs due to some chemical reactivity. Evidently, some reporters have deduced from the functional group identification via Fourier transform infrared spectroscopy (FTIR) analysis that OH functional group in the extract are responsible for bio-reduction (Mohamed et al., 2020). The growth phase occurs during the annealing and segregation of iron atoms which progressively combined to yield IONPs. Finally, the termination step encompasses the stabilization of synthesized IONPs, which occurs when the equivalent amount of function groups found in the extract bind with the surface of the IONPs. Another study has reported the three stages involved in the formation mechanism of IONPs as; complexing of iron cation with hydroxyl functional group, simultaneous bio-reduction of iron cation with hydroxyl functional group to form IONPs and capping of formed IONPs with hydroxyl containing functional group (Thilagavathi et al., 2016). The flow chart illustrating the synthesis of IONPs from plant material is presented in Fig. 1.

3. Optimization

During the synthesis of IONPs some conditions have to be attained to obtain maximum yield and desired morphological features. Such conditions and parameters are ratios of volume of extracting solvent to plant material, temperature, concentration of precursor solution, pH of solution, reaction and incubation time.

3.1 Effect of precursor

Result from previous study had shown different precursors adopted for the green synthesis of IONPs using plant extract. Examples of such precursors are ferric nitrate, ferric chloride, iron acetate, ferrous sulphate, ferric citrate, ammonium ferric citrate. Some mixture of precursors such as mixture of ferrous sulphate and ferric chloride, mixture of potassium ferricyanide and potassium ferrocyanide. The study conducted by Rajendran and Sen (2016) on the effect of precursors on the synthesis of IONPs showed that there was a huge variation in number of days taken for the synthesis of IONPs using different precursors. They stated that the solubility of precursors in water has influence on the reaction kinetics. Furthermore, they concluded that all the precursors showed different morphological features when the IONPs synthesized were compared. Another study had revealed that the nature of the precursor used for the green synthesis of IONPs determine its reaction time, shape and size (Sayed and Polshettiwar, 2015).

3.2 Effect of concentration of precursor

Studies have shown that concentration of precursor influence the time taken for the synthesis of IONPs. Increase in concentration of precursor causes an increase in the rate of synthesis while decrease in concentration of precursor has been linked with delay in bio-reduction process during IONPs. This phenomenon was attributed to inadequate proportion of biomolecules present in the extract to the precursor for growth and nucleation of nanocrystals in the solution (Zhu et al., 2012). The influence of concentration of precursor on particle size has been reported, decrease in concentration of precursor have been found to yield IONPs with decrease particle size and vice versa (Verma and Mehata, 2016). Nucleation and growth models of NPs have been adopted in the explanation of the effect of concentration of precursor on particle size claiming that the number of NPs formed in the solution

increased with increase in precursor concentration. Aside nucleation rate, delay in particle growth was also noted as the concentration of precursor increases resulting to increase in the availability of elemental concentrations of precursor which cause increase in the size of particle (Cho et al., 2016).

3.3 Effect of pH

The pH which determines the level of acidity and basicity of reaction medium has been detected to be an important factor that influences the synthesis of IONPs and other metal oxide NPs from plants materials. The influences of pH of solution medium on size and texture of NPs synthesized from plant extract has been documented (Jacob et al., 2019). Therefore, variation of the pH of solution has been adopted in regulation and control of shape and size of the synthesized NPs (Huang et al., 2015). The pH of basic medium (7 to 9) has been reported as the optimum condition for the synthesis of IONPs *Aeromonas hydrophila* (Lenders et al., 2016). The biosynthesis that occurs at pH 12 and 4 has been reported to completely retard the synthesis of IONPs. This indicated that extreme acidic and basic conditions do not favor the synthesis of IONPs using plant extract (Woźnica et al., 2003).

3.4 Effect of temperature

Temperature is one of the crucial parameters that influences the physical, chemical and biological method of synthesizing IONPs. The temperature requirement for the green synthesis of IONPs using plant extract is in the range of 25 to 100 °C (Patra et al., 2014). However, most researchers prefer the synthesis of IONPs at room temperature due to the volatility of some secondary metabolites of plants extract that are needed for bio-reduction of iron ions. Findings have shown that temperature of the reaction solution influences the morphological identity of NPs (Patra et al., 2014). Findings from the UV-visible analysis of IONPs synthesis from plant part at temperatures interval of 40 and 30 °C shown complete synthesis at 48 and 72 h, respectively. This indicated that rapid synthesis occurs at higher temperatures. This report also indicated that an increase in temperature beyond 40 °C led to poor synthesis of IONPs, which was attributed to the inactivation of biomolecules liable for the reduction of the iron precursor (Rajendran and Sen, 2016). However, a report has shown the successful synthesis of IONPs using *Punica granatum* seed extract at temperature of 70 °C (Bibi et al., 2019).

3.5 Time or reaction and incubation

The influence of incubation time on NPs synthesized using plant extract have been examined to influence the morphological properties and qualities of NPs (Harlekar et al., 2014). Other factors, such as storage conditions, device used for storage and exposure to light also affect the reaction time of IONPs. Long time incubation period has been documented to cause aggregation and shrinkage of particles (Saif et al., 2016).

3.6 Effect of type of plant extracts and concentrations of on IONPs synthesis

The synthesis of IONPs using plants extract is dependent on types of phytochemical found in the extract and the volume used (Devatha et al., 2018). The volume of plant extract used for the synthesis of NPs influence its duration of complete synthesis. When large volume of extract is being used, the rate of synthesis occurs rapidly because more chemical constituents are available in the solution which bind with the iron precursor to effect rapid bio-reduction and stabilization of IONPs while limited volume of extracts are being used the rate of IONPs formation decreases because there are insufficient biomolecules to bind with the metal precursor, which finally result into instability of NPs formed because the iron precursor would not be completely reduced to zerovalent form (Fazlzadeh et al., 2017). To attain an optimum condition for the green synthesis of IONPs, the ratio of the volume of plant extract must correspond to the concentration of iron precursor used because complete bio-reduction occur when there is equivalent amount of iron precursor and functional groups capable of causing reduction (Toledo et al., 2018). Also, the nature and kind of phytochemical available in plant extract influences the yield of IONPs produced (Gholami et al., 2018). The yield of IONPs depend largely on the volume of extract used for synthesis. High volume of extract has been reported induced to increased yield of synthesized IONPs when various volumes of plant extract were used, this was linked to the present of more functional groups, which react with the iron salt to produce improved absorption (Sumera et al., 2018). Findings have proved that volume and kind of extract used for NPs synthesis also affected their morphological properties and biological activities (Shen et al., 2017).

4. Characterization techniques

Several techniques have been used for the evaluation of the properties of synthesized IONPs. The confirmation of IONPs formation is examined with UV spectroscopy (Ramesh et al., 2018). Fourier transform infrared spectroscopy (FTIR) is used for the functional group identification (Devi et al., 2018). The morphological properties are determined by microscopy techniques such as transmission electron microscope (TEM), scanning electron microscopy (SEM), and atomic force microscopy (AFM) (Lassoued et al., 2017). The crystallinity of synthesized IONPs is determined with X-ray diffraction (Akintelu et al., 2020a) while the purity and composition of element are measured with EDX (Rufus et al., 2017) and total reflection X-ray fluorescence (TXRF) (Kulesh et al., 2016).

4.1 Nanoparticle formation analysis

Ultraviolet visible spectroscopy is a technique used for the confirmation of the formation of metal NPs and metal oxide NPs, such as IONPs (Madubuonu et al., 2020). This is carried out by the measurement of its surface plasmon resonance and estimation of the oscillations of conduction band electrons obtained in the electromagnetic radiation (Madubuonu et al., 2020). Ultraviolet analysis has been used to study the stability, size, aggregation and structure of the NPs (Aisida et al., 2020a). Each metal oxide and metal NPs have specific absorbance wavelength and this is obtained from the UV spectrum when incident rays of light encounter the conduction band electrons on the surface of the metal NPs (Akintelu et al., 2020b). The specific absorbance band for IONPs is in the range of 280 to 450 nm on the UV spectrum (Aisida et al., 2020b). Findings obtained from recent studies on the use of UV analysis for the confirmation of IONPs formation are summarized in Tab. 1.

4.2 Functional group identification

Fourier transform infrared spectroscopy is useful for the identification of the functional groups present in the plant extract and IONPs (Kumar et al., 2016). It is equally used in the determination of the functional groups that participated in the bio-reduction of the iron precursors (Mirza et al., 2018). Fourier transform infrared spectroscopy analysis can produce the absorption and infrared emission spectrum of solid, liquid and gas. The uniqueness in the combination of atoms of biomolecules enhance the identification of functional groups present in synthesized IONPs using the spectra obtained from FTIR analysis (Vasantharaj et al., 2019). The spectrum obtained from FTIR spectroscopic analysis presents fingerprint containing the absorption peaks that correspond to the wavelength of vibrations within the bounds of atoms of the NPs (Ibraheem et al., 2019; Sneha and Karthikeyan, 2019). Fourier transform infrared spectroscopy analysis have been used by numerous researchers to confirm the presence of some biomolecules, such as flavonoids, tannins, alkaloids, saponins in the extract of plants used for the bio-reduction of iron precursors during the formation of IONPs (Rahmani et al., 2019). The prominent functional groups that are responsible for the reduction process during the synthesis of IONPs obtained from previous studies are presented in Tab. 1.

4.3 Morphological assessment of IONPs

4.3.1 Transmission electron microscope (TEM)

Transmission electron microscope is one of the frequently used characterization tools for shape, size, and morphology determination of IONPs (Ebrahiminezhad et al., 2017a). Conversely, the IONPs preparatory procedure for TEM analysis is very complicated because the sample (IONPs) must be very thin for electron transmittance. The IONPs are enclosed in thin films prepared on copper grids coated with carbon by releasing small quantity of IONPs in solution onto the grid and extra solution on the grid are removed with blotting papers (Rizwan et al., 2018). To aid easy penetration of monochromatic beam of electrons through the sample which produce an image on the viewing screen, the prepared samples are dried under a mercury lamp (Liu et al., 2015). The used of TEM in the morphological assessment of IONPs synthesized from several plant materials have been reported by many researches and summary of their results are documented in Tab. 1.

4.3.2 Scanning electron microscopy (SEM)

Scanning electron microscopy is an electron microscopy-based technique that have been used for the morphological evaluation of numerous NPs via direct visualization (Akintelu et al., 2021). These techniques have some unique benefits for morphological and size analysis when compared with other available techniques. For the preparatory procedures of IONPs for SEM analysis. The IONPs

solution will be evaporated to dryness, the powder obtained are then mounted on a sample holder of the SEM machine and will be coated with a conductive metal using a sputter coater (Ebrahiminezhad et al., 2017b). Subsequently, a beam of high energy electrons will be focused to the IONPs to produce several signals on its surface (Ranmadugala et al., 2017). Then the signals on the IONPs surface are captured by electron beams and are recorded by the detector where information about the crystalline structure, external morphology, orientation and chemical composition of IONPs are determined (Sulaiman et al., 2018). The deficiency of SEM is in its inability to provide only accurate and sufficient information about the average size distribution of IONPs (Rajiv et al., 2017). Findings on the morphological determination of synthesized IONPs using several plant extracts via TEM analysis are summarized in Tab. 1.

4.3.3 Atomic force microscopy (AFM)

Several findings have shown the use of AFM in morphological evaluation of NPs (Adio et al., 2017). This technique is based on scanning of samples (IONPs) using a probe tip at the submicron level and with the aid of installed software-based image processing crucial information about morphology, surface texture, length, width, and height of NPs can be deduced (Jubb and Allen, 2010). For sample preparation for AFM analysis, a small amount of IONPs solution is placed on a glass slipcover attached to the AFM stub and dried over nitrogen gas at ambient temperature. Several images are recorded for better interpretation (Jagathesan and Rajiv, 2018). This instrument makes the use of the forces between the surface and the tip of the sample in generating topographical map which is scanned in contact mode (Bishnoi et al., 2018). The advantages of AFM in morphological evaluation of NPs does not require sample pretreatment before producing their images, it can be used to evaluate the morphological features of nonconducting samples and it also produce information about the volume and height of NPs (Katata-Seru et al., 2018).

4.3.4 Elemental composition

4.3.4.1 Energy dispersive X-ray spectra (EDX)

In order to evaluate the purity and elemental composition of NPs synthesized using plant extracts, some researchers have used EDX technique (Yadav and Fulekar, 2018). The elemental composition of IONPs is determined from the X-rays emission obtained from IONPs after they have been bombarded with an electron beam (Khalil et al., 2017). Also, the use of an attached EDS detector to SEM have been used to determine the composition of elements in IONPs by estimating the number of X-rays emitted to balance the difference in energy of the two electrons (Badni et al., 2016). This is attainable because the emitted X-ray energy is a characteristic identity of the element when quantitatively and qualitatively analyzed (Akintelu et al., 2020c).

4.3.4.2 Crystallinity evaluation

XRD have been reported as a good technique for the crystallinity assessment of synthesized NPs (Demirezen et al., 2018). The crystallinity assessment is accomplished by analyzing the lattice and structure parameters of the diffracted IONPs powder by measuring the diffraction angle when X-ray beam incident on them. With the aid of Scherrer formula represented with Eq. 2 the crystal size can be determined based on the X-ray peaks width (Truskewycz et al., 2016).

$$\text{Crystal size} = \frac{k\lambda}{\beta \cos\theta} \qquad (2)$$

where k = shape factor (0.94), λ = wavelength of incident X-ray, β = full width half maximum and θ = Bragg's angle.

5. Applications of IONPs synthesized from plant extract

5.1 Antimicrobial applications

Various investigations have been carried out to enhance the antimicrobial activities of available antibiotic drugs and also to develop novel antimicrobial agents to reduce/eliminate the microbial resistance towards readily available antibiotics and antiseptic (Ansari et al., 2017). Reports from the *in vitro* antimicrobial studies of metal and metal oxide NPs on numerous microbial species showed that metal oxide and metal NPs demonstrated remarkable inhibition against the growth of tested microbial species when compared with commercially available antibiotics and antiseptic (Rana et al., 2019). However, the antimicrobial activities of IONPs and other NPs depends upon majorly on particle size and material used for synthesis. Over the past decades, IONPs functionalized with therapeutic agents, such as

antimicrobials, have gained scientific and industrial attention because of their impressive results of antimicrobial and antibiofilm activities (Holban, 2015). When IONPs agglomerate, their surfaces are modified with important biological molecules and other polymer, IONPs have been coated with several antimicrobial agents to prevent IONPS agglomeration in attempt to extend the utility of engineered IONPs in biomedical applications (Seabra et al., 2017). The utilization of metal NPs have been recommended as the most promising approach for eradicating microbial drug resistance because of their multiple reaction mechanisms with microbial cells (Seabra et al., 2017). Some of the reaction mechanisms are generation of pits in the bacterial cell, which causes fragmentation of the cell wall, denaturation of the outermost membrane of microbes especially bacterial, and reaction with the disulfide groups of enzymes to obstruct metabolic processes, which causes cell death (Rai et al., 2013). Like other metal and metal oxide NPs such as silver, gold, zinc oxide and copper oxide. The IONPs also possess potential antimicrobial activities (Taghizadeh et al., 2019). Patra et al. (2017) reported that IONPs synthesized using corn plant extract exerted synergistic antibacterial activities against tested bacterial species. Previous study on the bactericidal action of IONPs synthesized using the fruit extract of *Couroupita guianensis* revealed that particles exhibited effective bactericidal potency on tested human pathogens (Gao et al., 2017). Findings have equally shown that the growth of *Proteus mirabilis* and *Escherichia coli* can be limited by IONPS obtained using leaf extract of *Argemone mexicana* L. (Arokiyaraj et al., 2013). The potential of IONPs in combating both gram positive and gram-negative bacteria have been reported effective and further strategies to develop synergistic IONPs platform which could function as carrier system for the treatment of microbial infection in future have been devised (Nehra et al., 2018). Some results obtained from recent studies on the antimicrobial potency of IONPs synthesized using plant extracts against the growth of some deadly human pathogens are shown in Tab. 2.

5.2 Anticancer applications

Lack of selective targets and multidrug resistance have made the effective treatment of tumor and cancer an abortive and worrisome issue (El-Boubbou, 2018). The advancement in nanotechnology and nanoscience over the years have shown some effective contribution of NPs in cancer treatment due to their exceptional features and mechanism of reaction with cancerous cells (Sathishkumar et al., 2018). Among the existing metal oxide NPs, IONPs have been recommended as good anticancer therapy due to their large surface area to graft targeting substrates and moieties, great resistance to *in vivo* degradation and potential synergistic activity in influencing the sensitivity of drugs towards the treatment of cancer (Bahrami et al., 2017). The cytotoxicity effect of biosynthesized IONPs against human HepG2 liver cell lines reveal that IONPs is capable of inhibiting the growth of cancer cell as the concentrations of IONPs increases (Rajendran et al., 2015). It was deduced from an investigation conducted to determine the cytotoxicity efficiency of lead oxide NPs and IONPs against HepG2 cells that IONPs exhibited higher cytotoxicity efficiency of 38.49% against HepG2 cells while the cytotoxicity efficiency of lead oxide NPs was 20.88%. The difference in the efficiency of the metal oxides in inhibiting the growth of HepG2 cells was linked with the smaller particle size of IONPs (Muhammad et al., 2019). The result obtained from the *in vitro* cytotoxicity evaluation of various concentrations of IONPs synthesized using flaxseed against MCF-7 cells revealed high toxicity efficacy at concentrations of 4.7 μg mL^{-1} and above (Rahmani et al., 2020). The high cytotoxicity efficiency of IONPs against the MCF-7 cell line was attributed to the ability of IONPs in causing breakdown of MCF-7 cells membrane by interacting with the phospholipid molecules in the cell layer (Berry et al., 2004). An outstanding cytotoxicity effect has been documented from the action of *Psoralea corylifolia* mediated IONPs against significant anticancer activity against renal tumor cells (Nagajyothi et al., 2017).

5.3 Environmental application

The wide use of anionic and cationic dyes in textiles, plastic, pharmaceuticals, leather, printing, and paper milling industries had led to their gigantic demand and supply across the globe (Fowsiya et al., 2016). Findings have shown that after manufacturing processes in the aforementioned industries over 20% of the total dyes used are wasted and are discharged into the environment where they resulted into various forms of environmental pollution (Ratna and Padhi, 2012). The discharge of dye and other toxic waste into the ecosystem have result to the death of many aquatic animals, water turbidity and several human health menace (Jin et al., 2018). However, the management and effective control of effluents containing dyes have been a daunting challenge. The implication of the environmental challenges associated with industrial effluents have led to the investigation of the catalytic

degradation and oxidation of dyes by metal and metal oxide NPs (Thandapani et al., 2018). Interestingly, metal oxides, such as zinc, copper, titanium and iron oxides, have showed good dye degradation efficiency (Gonawala and Mehta, 2014; Stan et al., 2015). The photodegradation of dyes by IONPs have been attributed to the easy adsorption of dyes linked with the high surface area to mass ratio and large number of surface reactive sites of metal oxide NPs (Dutta et al., 2014). Catalyst loading, pH, temperature, and time have reported as the major factors affecting the photocatalytic activities of IONPs (Ahmed et al., 2020). Several results obtained from the applications of IONPs on environmental control of toxic effluent containing dyes and inorganic substance are documented in Tab. 2.

6. Conclusion

This review discussed elaborately the various methods and techniques involved in the synthesis and characterization of IONPs. In general, the bioactive constituents of plant extract used for the synthesis of IONPs offer other benefits, such as improved biological activities and prevention of agglomeration aside been a reducing and stabilizing agent during the process of synthesis. The optimum conditions for the proper synthesis and improved yield of IONPs with desirable properties are well discussed. Review from the literature shows that plant-based synthesis is environmentally friendly, scalable to industrial production, nontoxic, very fast and consume less energy. Despite the numerous applications of biosynthesized IONPs in effluent treatment, catalysis and biomedicine, there is need for advance study to puffer solution to the challenges in comprehending the subsurface mechanistic pathways and transport of IONPs in the environments and their toxicological consequences.

Authors' contribution

Conceptualization: Akintelu, S. A.
Data curation: Oyebamiji, A. K.
Formal Analysis: Oyebamiji, A. K.; Folorunso, A. S.
Funding acquisition: Not applicable.
Investigation: Akintelu, S. A.; Folorunso, A. S.; Oyebamiji, A. K.
Methodology: Folorunso, A. S.
Project administration: Oyebamiji, A. K.
Resources: Not applicable.
Software: Not applicable.

Supervision: Oyebamiji, A. K.
Validation: Olugbeko, S. C.
Visualization: Akintelu, S. A.
Writing – original draft: Akintelu, S. A.
Writing – review & editing: Olugbeko, S. C.

Data availability statement

The data will be available upon request

References

Adio, S. O.; Omar, M. H.; Asif, M.; Saleh, T. A. Arsenic and selenium removal from water using biosynthesized nanoscale zero-valent iron: A factorial design analysis. *Process Saf. Environ. Prot.* **2017**, *107*, 518–527. https://doi.org/10.1016/j.psep.2017.03.004

Ahmad, W.; Khan, A. U.; Shams, S.; Qin, L.; Yuan, Q.; Ahmad, A.; Wei, Y.; Khan, Z. U. H.; Ullah, S.; Rahman, A. U. Eco-benign approach to synthesize spherical iron oxide nanoparticles: A new insight in photocatalytic and biomedical applications. *J. Photochem. Photobiol. B, Biol.* **2020**, *205*, 111821. https://doi.org/10.1016/j.jphotobiol.2020.111821

Ahmed, A.; Usman, M.; Yu, B.; Ding, X.; Peng, Q.; Shen, Y.; Cong, H. Efficient photocatalytic degradation of toxic Alizarin yellow R dye from industrial wastewater using biosynthesized Fe nanoparticle and study of factors affecting the degradation rate. *J. Photochem. Photobiol. B, Biol.* **2020**, *202*, 111682. https://doi.org/10.1016/j.jphotobiol.2019.111682

Aisida, S. O.; Madubuonu, N.; Alnasir, M. H.; Ahmad, I.; Botha, S.; Maaza, M.; Ezema, F. I. Biogenic synthesis of iron oxide nanorods using *Moringa oleifera* leaf extract for antibacterial applications. *Appl. Nanosci.* **2020a**, *10*, 305–315. https://doi.org/10.1007/s13204-019-01099-x

Aisida, S. O.; Ahmad, I.; Ezema, F. I. Effect of calcination on the microstructural and magnetic properties of PVA, PVP and PEG assisted zinc ferrite nanoparticles. *Phys. B:*

Condens. Matter **2020b**, *579*, 411907. https://doi.org/10.1016/j.physb.2019.411907

Aisida, S. O.; Ugwu, K.; Akpa P.; Nwanya, A. C.; Nwankwo, U.; Bashir, A. K. H.; Madiba, I.; Ahmed, I.; Ezema, F. Synthesis and characterization of iron oxide nanoparticles capped with *Moringa oleifera*: The mechanisms of formation effects on the optical, structural, magnetic and morphological properties. *Mater. Today: Proc.* **2021**, *36*, 214–218.

Akintelu, S. A.; Folorunso, A. S. Biosynthesis, Characterization and Antifungal Investigation of Ag-Cu Nanoparticles from Bark Extracts of G*arcina kola*. *Stem Cell* **2019a**, *10* (4), 30–37. https://doi.org/10.7537/marsscj100419.05

Akintelu, S. A.; Folorunso, A. S. Characterization and Antimicrobial Investigation of Synthesized Silver Nanoparticles from *Annona muricata* Leaf Extracts. *Journal of Nanotechnology Nanomedicine & Nanobiotechnology* **2019b**, *6*, 022. https://doi.org/10.24966/NTMB-2044/100022

Akintelu, S. A.; Folorunso, A. S.; Ademosun, O. T. Instrumental Characterization and Antibacterial Investigation of Silver Nanoparticles Synthesized from *Garcinia Kola* Leaf. Journal of Drug Delivery and Therapeutics **2019a**, *9* (6-S), 58–64. https://doi.org/10.22270/jddt.v9i6-s.3749

Akintelu, S. A.; Folorunso, A. S.; Oyebamiji, A. K.; Erazua, E. A. Antibacterial potency of silver nanoparticles synthesized using *Boerhaavia diffusa* leaf extract as reductive and stabilizing agent. *Int. J. Pharm. Sci. Res.* **2019b**, *10* (12), 374–380.

Akintelu, S. A.; Olugbeko, S. C.; Folorunso, A. S. A review on synthesis, optimization, characterization and antibacterial application of gold nanoparticles synthesized from plants. *Int. Nano Lett.* **2020a**, *10*, 237–248. https://doi.org/10.1007/s40089-020-00317-7

Akintelu, S. A.; Olugbeko, S. C.; Folorunso, F. A.; Oyebamiji, A. K.; Folorunso, A. S. Characterization and Pharmacological Efficacy of Silver Nanoparticles Biosynthesized Using the Bark Extract of *Garcinia Kola*. *J. Chem.* **2020b**, *2020*, 2876019. https://doi.org/10.1155/2020/2876019

Akintelu, S. A.; Bo, Y.; Folorunso, A. S. A Review on Synthesis, Optimization, Mechanism, Characterization, and Antibacterial Application of Silver Nanoparticles Synthesized from Plants. *J. Chem.* **2020c**, *2020*, 3189043. https://doi.org/10.1155/2020/3189043

Akintelu, S. A.; Yao, B.; Folorunso, A. S. Green Synthesis, Characterization, and Antibacterial Investigation of Synthesized Gold Nanoparticles (AuNPs) from *Garcinia*

kola Pulp Extract. *Plasmonics* **2021**, *16*, 157–165. https://doi.org/10.1007/s11468-020-01274-9

Alam, T.; Khan, R. A. A.; Ali, K.; Ali, A.; Sher, H.; Ullah, Z.; Ali, M. Biogenic synthesis of iron oxide nanoparticles via *Skimmia laureola* and their antibacterial efficacy against bacterial wilt pathogen *Ralstonia solanacearum*. *Mater. Sci. Eng. C* **2019**, *98*, 101–108. https://doi.org/10.1016/j.msec.2018.12.117

Alharbi, K. K.; Al-sheikh, Y. A. Role and implications of nanodiagnostics in the changing trends of clinical diagnosis. *Saudi J. Biol. Sci.* **2014**, *21* (2), 109–117. https://doi.org/10.1016/j.sjbs.2013.11.001

Ali, A.; Zafar, H.; Zia, M.; ul Haq, I.; Phull, A. R.; Ali, J. S.; Hussain, A. Synthesis, characterization, applications, and challenges of iron oxide nanoparticles. *Nanotechnol. Sci. Appl.* **2016**, *9*, 49–67. https://doi.org/10.2147/NSA.S99986

Ansari, S. A.; Oves, M.; Satar, R.; Khan, A.; Ahmad, S. I.; Jafri, M. A.; Zaidi, S. K.; Alqahtani, M. H. Antibacterial activity of iron oxide nanoparticles synthesized by co–precipitation technology against *Bacillus cereus* and *Klebsiella pneumoniae*. *Pol. J. Chem. Tech.* **2017**, *19* (4), 110–115. https://doi.org/10.1515/pjct-2017-0076

Arokiyaraj, S.; Saravanan, M.; Prakash, N. K. U.; Arasu, M. V.; Vijayakumar, B.; Vincent, S. Enhanced antibacterial activity of iron oxide magnetic nanoparticles treated with *Argemone Mexicana* L. leaf extract: An *in vitro* study. *Mater. Res. Bull.* **2013**, *48*, 3323–3327. https://doi.org/10.1016/j.materresbull.2013.05.059

Arsalani, S.; Guidelli, E. J.; Silveira, M. A.; Salmon, C. E. G.; Araujo, J. F. D. F.; Bruno, A. C.; Baffa, O. Magnetic Fe_3O_4 nanoparticles coated by natural rubber latex as MRI contrast agent. *J. Magn. Magn. Mater.* **2019**, *475*, 458–464. https://doi.org/10.1016/j.jmmm.2018.11.132

Arularasu, M. V.; Devakumar, J.; Rajendran, T. V. An innovative approach for green synthesis of iron oxide nanoparticles: Characterization and its photocatalytic activity. *Polyhedron* **2018**, *156*, 279–290. https://doi.org/10.1016/j.poly.2018.09.036

Asghar, M. A.; Zahir, E.; Shahid, S. M.; Khan, M. N.; Asghar, M. A.; Iqbal, J.; Walker, G. Iron, copper and silver nanoparticles: Green synthesis using green and black tea leaves extracts and evaluation of antibacterial, antifungal and aflatoxin B_1 adsorption activity. *LWT* **2018**, *90*, 98–107. https://doi.org/10.1016/j.lwt.2017.12.009

Assa, F.; Jafarizadeh-Malmiri, H.; Ajamein, H.; Anarjan, N.; Vaghari, H.; Sayyar, Z.; Berenjian, A. A biotechnological perspective on the application of iron oxide nanoparticles. Nano Research **2016**, *9*, 2203–2225. https://doi.org/10.1007/s12274-016-1131-9

Badni, N.; Benheraoua, F. Z.; Tadjer, B.; Boudjemaa, A.; El Hameur, H.; Bachari, K. Green synthesis of α-Fe₂O₃ nanoparticles using Roman nettle. *Proceedings of the Third International Conference on Energy, Materials, Applied Energetics and Pollution, ICEMAEP2016*, Constantina, Algeria, October 30–31, 2016; Kadja, M., Zaatri, A., Nemouchi, Z., Bessaih, R., Benissaad, S., Talbi, K., Eds.

Bahrami, B.; Hojjat-Farsangi, M.; Mohammadi, H.; Anvari, E.; Ghalamfarsa, G.; Yousefi, M.; Jadidi-Niaragh, F. Nanoparticles and targeted drug delivery in cancer therapy. *Immunol. Lett.* **2017**, *190*, 64–83. https://doi.org/10.1016/j.imlet.2017.07.015

Bashir, A. K. H.; Mayedwa, N.; Kaviyarasu, K.; Razanamahandry, L. C.; Matinise, N.; Bharuth-Ram, K.; Tchokonté, M. B. T.; Ezema, F. I.; Maaza, M. Investigation of electrochemical performance of the biosynthesized α-Fe₂O₃ nanorods. *Surf. Interfaces* **2019**, *17*, 100345. https://doi.org/10.1016/j.surfin.2019.100345

Berry, C. C.; Wells, S.; Charles, S.; Aitchison, G.; Curtis, A. S. G. Cell response to dextran-derivatised iron oxide nanoparticles post internalization. *Biomaterials* **2004**, *25* (23), 5405–5413. https://doi.org/10.1016/j.biomaterials.2003.12.046

Bibi, I.; Nazar, N.; Ata, S.; Sultan, M.; Ali, A.; Abbas, A.; Jilani, K.; Kamal, S.; Sarim, F. M.; Khan, M. I.; Jalal, F.; Iqbal, M. Green synthesis of iron oxide nanoparticles using pomegranate seeds extract and photocatalytic activity evaluation for the degradation of textile dye. *J. Mat. Res. Technol.* **2019**, *8* (6), 6115–6124. https://doi.org/10.1016/j.jmrt.2019.10.006

Bishnoi, S.; Kumar, A.; Selvaraj, R. Facile synthesis of magnetic iron oxide nanoparticles using inedible *Cynometra ramiflora* fruit extract waste and their photocatalytic degradation of methylene blue dye. *Mater. Res. Bull.* **2018**, *97*, 121–127. https://doi.org/10.1016/j.materresbull.2017.08.040

Bolade, O. P.; Akinsiku, A. A.; Adeyemi, A. O.; Williams, A. B.; Benson, N. U. Dataset on phytochemical screening, FTIR and GC–MS characterisation of *Azadirachta indica* and *Cymbopogon citratus* as reducing and stabilising agents for nanoparticles synthesis. *Data Brief* **2018**, *20*, 917–926. https://doi.org/10.1016/j.dib.2018.08.133

Bolade, O. P.; Williams, A. B.; Benson, N. U. Green synthesis of iron-based nanomaterials for environmental remediation: A revie. *Environ. Nanotechnol. Monit. Manag.* **2020**, *13*, 100279. https://doi.org/10.1016/j.enmm.2019.100279

Buiyan, S. H.; Muhammed, Y. M.; Paul, S. C.; Aka, T. D.; Saha, O.; Rahaman, M.; Sharif, J. I.; Habiba, O.; Ashaduzzaman. Green synthesis of iron oxide nanoparticle using *Carica papaya* leaf extract: application for

photocatalytic degradation of remazol yellow RR dye and antibacterial activity. *Heliyon* **2020**, *6* (8), e04603. https://doi.org/10.1016/j.heliyon.2020.e04603

Cabrera, L.; Gutierrez, S.; Menendez, N.; Morales, M. P.; Herrasti, P. Magnetite nanoparticles: Electrochemical synthesis and characterization. *Electrochim. Acta* **2008**, *53* (8), 3436–3441 https://doi.org/10.1016/j.electacta.2007.12.006

Chauhan, S.; Upadhyay, L. S. B. Biosynthesis of iron oxide nanoparticles using plant derivatives of *Lawsonia inermis* (Henna) and its surface modification for biomedical application. *Nanotechnol. Environ. Eng.* **2019**, *4*, 8. https://doi.org/10.1007/s41204-019-0055-5

Cheera, P.; Karlapudi, S.; Sellola, G.; Ponneri, V. A facile green synthesis of spherical Fe₃O₄ magnetic nanoparticles and their effect on degradation of methylene blue in aqueous solution. *J. Mol. Liq.* **2016**, *221*, 993–998. https://doi.org/10.1016/j.molliq.2016.06.006

Cho, J. S.; Lee, J.-C.; Rhee, S.-H. Effect of precursor concentration and spray pyrolysis temperature upon hydroxyapatite particle size and density. *J. Biomed. Mater. Res. Part B Appl. Biomater.* **2016**, *104* (2), 422–430. https://doi.org/10.1002/jbm.b.33406

Demirezen, D. A.; Yilmaz, S.; Yilmaz, D. Green synthesis and characterization of iron nanoparticles using *Aesculus hippocastanum* seed extract. *Int. J. Adv. Sci. Technol.* **2018**, *6* (2) (Suppl. 2), 25–29.

Desalegn, B.; Megharaj, M.; Chen, Z.; Naidu, R. Green synthesis of zero valent iron nanoparticle using mango peel extract and surface characterization using XPS and GC-MS. *Heliyon* **2019**, *5* (5), e01750. https://doi.org/10.1016/j.heliyon.2019.e01750

Devatha, C. P.; Jagadeesh, K.; Mallikarjun, P. Effect of Green synthesized iron nanoparticles by *Azardirachta Indica* in different proportions on antibacterial activity. *Environ. Nanotechnol. Monit. Manag.* **2018**, *9*, 85–94. https://doi.org/10.1016/j.enmm.2017.11.007

Devi, H. S., Boda, M. A., Shah, M. A., Parveen, S. Green synthesis of iron oxide nanoparticles using *Platanus orientalis* leaf extract for antifungal activity. *Green Process. Synth.* **2018**, *8* (1), 38–45. https://doi.org/10.1515/gps-2017-0145

Dutta, A. K.; Maji, S. K.; Adhikary, B. γ-Fe₂O₃ nanoparticles: An easily recoverable effective photo-catalyst for the degradation of rose bengal and methylene blue dyes in the waste-water treatment plant. *Mater. Res. Bull.* **2014**, *49*, 28–34. https://doi.org/10.1016/j.materresbull.2013.08.024

Ebrahiminezhad, A.; Zare-Hoseinabadi, A.; Berenjian, A.; Ghasemi, Y. Green synthesis and characterization of zero-valent iron nanoparticles using stinging nettle (*Urtica dioica*) leaf extract. *Green Process. Synth.* **2017a**, *6* (5).

Ebrahiminezhad, A.; Zare, M.; Kiyanpour, S.; Berenjian, A.; Niknezhad, S. V.; Ghasemi, Y. Biosynthesis of xanthangum-coated INPs by using *Xanthomonas campestris*. *IET Nanobiotechnol.* **2017b**, *12* (3), 254–258. https://doi.org/10.1049/iet-nbt.2017.0199

El Shafey, A. M. Green synthesis of metal and metal oxide nanoparticles from plant leaf extracts and their applications: A review. Gruyter Green Processing and Synthesis **2020**, *9* (1), 304–339. https://doi.org/10.1515/gps-2020-0031

El-Boubbou, K. Magnetic iron oxide nanoparticles as drug carriers: clinical relevance. *Nanomedicine (Lond)* **2018**, *13* (8), 953–971. https://doi.org/10.2217/nnm-2017-0336

Fatimah, I.; Pratiwi, E. Z.; Wicaksono, W. P. Synthesis of magnetic nanoparticles using *Parkia speciosa Hassk* pod extract and photocatalytic activity for Bromophenol blue degradation. *Egypt. J. Aquat. Res.* **2020**, *46* (1), 35–40. https://doi.org/10.1016/j.ejar.2020.01.001

Fazlzadeh, M.; Rahmani, K.; Zarei, A.; Abdoallahzadeh, H.; Nasiri, F.; Khosravi, R. A novel green synthesis of zero valent iron nanoparticles (NZVI) using three plant extracts and their efficient application for removal of Cr(VI) from aqueous solutions. *Adv. Powder Technol.* **2017**, *28* (1), 122–130. https://doi.org/10.1016/j.apt.2016.09.003

Folorunso, A.; Akintelu, S.; Oyebamiji, A. K.; Ajayi, S.; Abiola, B.; Abdusalam, I.; Morakinyo, A. Biosynthesis, characterization and antimicrobial activity of gold nanoparticles from leaf extracts of *Annona muricata*. *J. Nanostruct. Chem.* **2019**, *9*, 111–117. https://doi.org/10.1007/s40097-019-0301-1

Fowsiya, J.; Madhumitha, G.; Al-Dhabi, N. A.; Arasu, M. V. Photocatalytic degradation of Congo red using *Carissa edulis* extract capped zinc oxide nanoparticles. *J. Photochem. Photobiol. B, Biol.* **2016**, *162*, 395–401. https://doi.org/10.1016/j.jphotobiol.2016.07.011

Franzoso, F.; Nisticò, R.; Cesano, F.; Corazzari, I.; Turci, F.; Scarano, D.; Prevot, A. B.; Magnacca, G.; Carlos, L.; Mártire, D. O. Biowaste-derived substances as a tool for obtaining magnet-sensitive materials for environmental applications in wastewater treatments. Chemical Engineering Journal **2017**, *310* (Part 1), 307–316. https://doi.org/10.1016/j.cej.2016.10.120

Gan, L.; Lu, Z.; Cao, D.; Chen, Z. Effects of cetyltrimethylammonium bromide on the morphology of green synthesized Fe_3O_4 nanoparticles used to remove phosphate. *Mater. Sci. Eng. C* **2018**, *82*, 41–45. https://doi.org/10.1016/j.msec.2017.08.073

Gao, L.; Fan, K.; Yan, X. Iron oxide nanozyme: a multifunctional enzyme mimetic for biomedical applications. *Theranostics* **2017**, *7* (13), 3207–3227. https://doi.org/10.7150/thno.19738

Gebre, S. H.; Sendeku, M. G. New frontiers in the biosynthesis of metal oxide nanoparticles and their environmental applications: an overview. *SN Appl. Sci.* **2019**, *1*, 928. https://doi.org/10.1007/s42452-019-0931-4

Gholami, L.; Oskuee, R. K.; Tafaghodi, M.; Farkhani, A. R.; Darroudi, M. Green facile synthesis of low-toxic superparamagnetic iron oxide nanoparticles (SPIONs) and their cytotoxicity effects toward Neuro2A and HUVEC cell lines. *Ceram. Int.* **2018**, *44* (8), 9263–9268. https://doi.org/10.1016/j.ceramint.2018.02.137

Gonawala, K. H.; Mehta, M. J. Removal of color from different dye wastewater by using ferric oxide as an adsorbent. *Int. J. Eng. Res. Appl.* **2014**, *4* (5), 102–109.

Gunarani, G. I.; Raman, A. B.; Kumar, J. D.; Natarajan, S.; Jegadeesan, G. B. Biogenic synthesis of Fe and NiFe nanoparticles using *Terminalia bellirica* extracts for water treatment applications. *Mater. Lett.* **2019**, *247*, 90–94. https://doi.org/10.1016/j.matlet.2019.03.104

Harlekar, M.; Barve, S.; Kumar, R. Plant-Mediated Green Synthesis of Iron Nanoparticles. *J. Nanoparticles* **2014**, *2014*, 140614. https://doi.org/10.1155/2014/140614

Harshiny, M.; Iswarya, C. N.; Matheswaran, M. Biogenic synthesis of iron nanoparticles using *Amaranthus dubius* leaves extract as reducing agents. *Powder Technol.* **2015**, *286*, 744–749. https://doi.org/10.1016/j.powtec.2015.09.021

Harshiny, M.; Samsudeen, N.; Kameswara, R. J.; Matheswaran, M. Biosynthesized FeO nanoparticles coated carbon anode for improving the performance of microbial fuel cell. International Journal of Hydrogen Energy **2017**, *42* (42), 26488–26495. https://doi.org/10.1016/j.ijhydene.2017.07.084

Holban, A. M. Magnetite nanoshuttles for fighting *Staphylococcus aureus* infections: a recent review. *Curr. Top. Med. Chem.* **2015**, *15* (16), 1589-1595. https://doi.org/10.2174/1568026615666150414152431

Huang, L.; Luo, F.; Chen, Z.; Megharaj, M.; Naidu, R. Green synthesized conditions impacting on the reactivity of Fe NPs for the degradation of malachite green. *Spectrochim. Acta A Mol. Biomol. Spectrosc.* **2015**, *137*, 154–159. https://doi.org/10.1016/j.saa.2014.08.116

Ibraheem, F.; Aziz, M. H.; Fatima, M.; Shaheen, F.; Ali, S. M.; Huang, Q. *In vitro* Cytotoxicity, MMP and ROS activity of green synthesized nickel oxide nanoparticles using extract of *Terminalia chebula* against MCF-7 cells. *Mater. Lett.*

2019, *234*, 129–133. https://doi.org/10.1016/j.matlet.2018.09.075

Iqbal, J.; Abbassi, B. A.; Ahmad, R.; Shahbaz, A.; Zahra, S. A.; Kanwal, S.; Rabbani, A.; Mahmood, T. Biogenic synthesis of green and cost-effective iron nanoparticles and evaluation of their potential biomedical properties. *J. Mol. Struct.* **2020**, *1199*, 126979. https://doi.org/10.1016/j.molstruc.2019.126979

Jacob, P. J.; Masarudin, M. J.; Hussein, M. Z.; Rahim, R. A. Optimization of process parameters influencing the sustainable construction of iron oxide nanoparticles by a novel tropical wetlands *Streptomyces* spp. *J. Clean. Prod.* **2019**, *232*, 193–202. https://doi.org/10.1016/j.jclepro.2019.05.359

Jagadeesan, G.; Srimathi, K.; Srinivas, N. S.; Manishkanna, S.; Vignesh, D. Green synthesis of iron oxide nanoparticles using *Terminalia bellirica* and *Moringa oleifera* fruit and leaf extracts: Antioxidant, antibacterial and thermoacoustic properties. *Biocatal. Agric. Biotechnol.* **2019**, *21*, 101354. https://doi.org/10.1016/j.bcab.2019.101354

Jagathesan, G.; Rajiv, P. Biosynthesis and characterization of iron oxide nanoparticles using *Eichhornia crassipes* leaf extract and assessing their antibacterial activity. *Biocatal. Agric. Biotechnol.* **2018**, *13*, 90–94. https://doi.org/10.1016/j.bcab.2017.11.014

Jin, X.; Liu, Y.; Tan, J.; Owens, G.; Chen, Z. Removal of Cr(VI) from aqueous solutions via reduction and absorption by green synthesized iron nanoparticles. *J. Clean. Prod.* **2018**, *176*, 929–936. https://doi.org/10.1016/j.jclepro.2017.12.026

Jubb, A. M.; Allen, H. C. Vibrational spectroscopic characterization of hematite, maghemite, and magnetite thin films produced by vapor deposition. *ACS Appl. Mater. Interfaces* **2010**, *2* (10), 2804–2812. https://doi.org/10.1021/am1004943

Kamran, U.; Bhatti, H. N.; Iqbal, M.; Jamil, S.; Zahid, M. Biogenic synthesis, characterization and investigation of photocatalytic and antimicrobial activity of manganese nanoparticles synthesized from *Cinnamomum verum* bark extract. *J. Mol. Struct.* **2019**, *1179*, 532–539. https://doi.org/10.1016/j.molstruc.2018.11.006

Karpagavinayagam, P.; Vedhi, C. Green synthesis of iron oxide nanoparticles using *Avicennia marina* flower extract. *Vacuum* **2019**, *160*, 286–292. https://doi.org/10.1016/j.vacuum.2018.11.043

Katata-Seru, L.; Moremedi, T.; Aremu, O. S.; Bahadur, I. Green synthesis of iron nanoparticles using *Moringa oleifera* extracts and their applications: Removal of nitrate from water and antibacterial activity against *Escherichia coli*. *J.*

Mol. Liq. **2018**, *256*, 296–304. https://doi.org/10.1016/j.molliq.2017.11.093

Khalil, A. T.; Ovais, M.; Ullah, I.; Ali, M.; Shinwari, Z. K.; Maaza, M. Biosynthesis of iron oxide (Fe₂O₃) nanoparticles via aqueous extracts of *Sageretia thea* (Osbeck.) and their pharmacognostic properties. Green Chem. Lett. Rev. **2017**, *10* (4), 186–201. https://doi.org/10.1080/17518253.2017.1339831

Khatami, M.; Alijani, H. Q.; Fakheri, B.; Mobasseri, Heydarpour, M.; Farahani, Z. K.; Khan, A. U. Super-paramagnetic iron oxide nanoparticles (SPIONs): Greener synthesis using *Stevia* plant and evaluation of its antioxidant properties. *J. Clean. Prod.* **2019**, *208*, 1171–1177. https://doi.org/10.1016/j.jclepro.2018.10.182

Kheshtzar, R.; Berenjian, A., Ganji, N.; Taghizadeh, S.-M.; Maleki, M.; Taghizadeh, S.; Ghasemi, Y.; Ebrahiminezhadm A. Response surface methodology and reaction optimization to product zero-valent iron nanoparticles for organic pollutant remediation. Biocatalysis and Agricultural Biotechnology **2019**, *21*, 101329. https://doi.org/10.1016/j.bcab.2019.101329

Kulesh, N. A.; Novoselova, I. P.; Safronov, A. P.; Beketov, I. V.; Samatov, O. M.; Kurlyandskaya, G. V.; Morozova, M.; Denisova, T. P. Total reflection x-ray fluorescence spectroscopy as a tool for evaluation of iron concentration in ferrofluids and yeast samples. *J. Magn. Magn. Mater.* **2016**, *415*, 39–44. https://doi.org/10.1016/j.jmmm.2016.01.095

Kumar, B.; Smita, K.; Cumbal, L.; Debut, A.; Galeas, S.; Guerrero, V. H. Phytosynthesis and photocatalytic activity of magnetite (Fe₃O₄) nanoparticles using the *Andean blackberry* leaf. *Mater. Chem. Phys.* **2016**, *179*, 310–315. https://doi.org/10.1016/j.matchemphys.2016.05.045

Lassoued, A.; Dkhil, B.; Gadri, A.; Ammar, S. Control of the shape and size of iron oxide (α- Fe₂O₃) nanoparticles synthesized through the chemical precipitation method. *Results Phys.* **2017**, *7*, 3007–3015. https://doi.org/10.1016/j.rinp.2017.07.066

Lemine, O. M.; Omri, K.; Zhang, B.; El Mir, L.; Sajieddine, M.; Alyamani, A.; Bououdina, M. Sol–gel synthesis of 8 nm magnetite (Fe₃O₄) nanoparticles and their magnetic properties. *Superlattices Microstruct.* **2012**, *52*, 793–799. https://doi.org/10.1016/j.spmi.2012.07.009

Lenders, J. J. M.; Mirabello, G.; Sommerdijk, N. A. J. M. Bioinspired magnetite synthesis *via* solid precursor phases. *Chem. Sci.* **2016**, *7* (9), 5624–5634, https://doi.org/10.1039/C6SC00523C

Lin, J.; Weng, X.; Dharmarajan, R.; Chen, Z. Characterization and reactivity of iron-based nanoparticles synthesized by tea extracts under various atmospheres

Chemosphere **2017**, *169*, 413–417. https://doi.org/10.1016/j.chemosphere.2016.11.092

Liu, G.; Sun, W.-j.; Tang, S.-s.; Liang, S.-q.; Liu, J. Synthesis of α-Fe₂O₃@SnO₂ core-shell nanoparticles via low-temperature molten salt reaction route. *Trans. Nonferrous Met. Soc. China* **2015**, *25* (11), 3651–3656. https://doi.org/10.1016/S1003-6326(15)64076-6

Liu, Y.; Jin, X.; Chen, Z. The formation of iron nanoparticles by *Eucalyptus* leaf extract and used to remove Cr(VI). *Sci. Total Environ.* **2018**, *627*, 470–479. https://doi.org/10.1016/j.scitotenv.2018.01.241

Liu, H.; Sun, Y.; Yu, T.; Zhang, J.; Zhang, X.; Zhang, H.; Zhao, K.; Wei, J. Plant-mediated biosynthesis of iron nanoparticles-calcium alginate hydrogel membrane and its eminent performance in removal of Cr(VI). *Chem. Eng. J.* **2019**, *378*, 122120. https://doi.org/10.1016/j.cej.2019.122120

Madubuonu, N.; Aisida, S. O.; Ali, A.; Ahmad, I., Zhao, T.-K.; Bothag, S.; Maaza, M., Ezema, F. I. Biosynthesis of iron oxide nanoparticles via a composite of *Psidium guavaja-Moringa oleifera* and their antibacterial and photocatalytic study. *J. Photochem. Photobiol. B, Biol.* **2019**, *199*, 111601. https://doi.org/10.1016/j.jphotobiol.2019.111601

Madubuonu, N.; Aisida, S. O.; Ahmad, I.; Botha, S.; Zhao, T.-k.; Maaza, M.; Ezema, F. I. E. Bio-inspired iron oxide nanoparticles using *Psidium guajava* aqueous extract for antibacterial activity. *Appl. Phys. A* **2020**, *126*, 72. https://doi.org/10.1007/s00339-019-3249-6

Miri, A.; Khatami, M.; Sarani, M. Biosynthesis, Magnetic and Cytotoxic Studies of Hematite Nanoparticles. *J. Inorg. Organomet. Polym.* **2020**, *30*, 767–774. https://doi.org/10.1007/s10904-019-01245-6

Mirza, A. U.; Kareem, A.; Nami, S. A. A.; Khan, M. S.; Rehman, S.; Bhat, S. A.; Mohammad, A.; Nishat, N. Biogenic synthesis of iron oxide nanoparticles using *Agrewia optiva* and *Prunus persica* phyto species: Characterization, antibacterial and antioxidant activity. *J. Photochem. Photobiol. B, Biol.* **2018**, *185*, 262–274. https://doi.org/10.1016/j.jphotobiol.2018.06.009

Mohamed, F.; Rabia, M.; Shaban, M. Synthesis and characterization of biogenic iron oxides of different nanomorphologies from pomegranate peels for efficient solar hydrogen production. *J. Mater. Res. Technol.* **2020**, *9* (3), 4255–4271. https://doi.org/10.1016/j.jmrt.2020.02.052

Mohanraj, S.; Kodhaiyolii, S.; Rengasamy, M.; Pugalenthi, V. Green Synthesized Iron Oxide Nanoparticles Effect on Fermentative Hydrogen Production by *Clostridium acetobutylicum*. *Appl. Biochem. Biotechnol.* **2014**, *173*, 318–331. https://doi.org/10.1007/s12010-014-0843-0

Muhammad, W.; Khan, M. A.; Nazir, M.; Siddiquah, A.; Mushtaq, S.; Hashmi, S. S.; Abbasi, B. H. *Papaver somniferum* L. mediated novel bioinspired lead oxide (PbO) and iron oxide (Fe₂O₃) nanoparticles: In-vitro biological applications, biocompatibility and their potential towards HepG2 cell line. *Mater. Sci. Eng. C* **2019**, *103*, 109740. https://doi.org/10.1016/j.msec.2019.109740

Mukherjee, P. *Stenotrophomonas* and *Microbacterium*: Mediated Biogenesis of Copper, Silver and Iron Nanoparticles—Proteomic Insights and Antibacterial Properties Versus Biofilm Formation. *J. Clust. Sci.* **2017**, *28*, 331–358. https://doi.org/10.1007/s10876-016-1097-5

Muthukumar, H.; Matheswaran, M. *Amaranthus spinosus* leaf extract mediated FeO nanoparticles: Physicochemical traits, photocatalytic and antioxidant activity. *ACS Sustainable Chem. Eng.* **2015**, *3* (12), 3149–3156. https://doi.org/10.1021/acssuschemeng.5b00722

Nagajyothi, P. C.; Pandurangan, M.; Kim, D. H.; Sreekanth, T.; Shim, J. Green synthesis of iron oxide nanoparticles and their catalytic and *in vitro* anticancer activities. *J. Clust. Sci.* **2017**, *28*, 245–257. https://doi.org/10.1007/s10876-016-1082-z

Nehra, P.; Chauhan, R. P.; Garg, N.; Verma, K. Antibacterial and antifungal activity of chitosan coated iron oxide nanoparticles. *Br. J. Biomed. Sci.* **2018**, *75* (1), 13–18. https://doi.org/10.1080/09674845.2017.1347362

Nisticò, R. Magnetic materials and water treatments for a sustainable future. *Res. Chem. Intermed.* **2017**, *43*, 6911–6949. https://doi.org/10.1007/s11164-017-3029-x

Nisticò, R.; Tabasso, S.; Magnacca, G.; Jordan, T.; Shalom, M.; Fechler, N. Reactive hypersaline route: One-pot synthesis of porous photoreactive nanocomposites. *Langmuir* **2017a**, *33* (21), 5213–5222. https://doi.org/10.1021/acs.langmuir.7b00142

Nisticò, R.; Scalarone, D.; Magnacca, G. Sol–gel chemistry, templating and spin-coating deposition: A combined approach to control in a simple way the porosity of in organic thin films/coatings. *Microporous Mesoporous Mater.* **2017b**, *248*, 18–29. https://doi.org/10.1016/j.micromeso.2017.04.017

Nisticò, R. Block copolymers for designing nanostructured porous coatings. *Beilstein J. Nanotechnol.* **2018**, *9*, 2332–2344. https://doi.org/10.3762/bjnano.9.218

Nisticò, R. A synthetic guide toward the tailored production of magnetic iron oxide nanoparticles. *Bol. Soc. Esp. Cerám. Vidr.* **2021**, *60* (1), 29–40. https://doi.org/10.1016/j.bsecv.2020.01.011

Palma, D.; Prevot, A. B.; Brigante, M.; Fabbri, D.; Magnacca, G.; Richard, C.; Mailhot, G.; Nisticò, R. New

insights on the photodegradation of caffeine in the presence of bio-based substances-magnetic iron oxide hybrid nanomaterials. *Materials* **2018**, *11* (7), 1084. https://doi.org/10.3390/ma11071084

Pang, Y. L.; Lim, S.; Ong, H. C.; Chong, W. T. Research progress on iron oxide-based magnetic materials: Synthesis technique sand photocatalytic applications. *Ceram. Int.* **2016**, *42* (1) (Part A), 9–34. https://doi.org/10.1016/j.ceramint.2015.08.144

Park, T. J.; Lee, K. G.; Lee, S. Y. Advances in microbial biosynthesis of metal nanoparticles. *Appl. Microbiol. Biotechnol.* **2016**, *100*, 521–534. https://doi.org/10.1007/s00253-015-6904-7

Pascu, O.; Carenza, E.; Gich, M.; Estradé, S.; Peiró, F.; Herranz, G.; Roig, A. Surface reactivity of iron oxide nanoparticles by microwave-assisted synthesis; comparison with the thermal decomposition route. *J. Phys. Chem. C* **2012**, *116* (28), 15108–15116. https://doi.org/10.1021/jp303204d

Patra, J. K.; Baek, K.-H. Green Nanobiotechnology: Factors Affecting Synthesis and Characterization Techniques. *J. Nanomater.* **2014**, *2014*, 417305. https://doi.org/10.1155/2014/417305

Patra, J. K.; Ali, S.; Oh, I.-G.; Baek, K.-H. Proteasome inhibitory, antioxidant, and synergistic antibacterial and anticandidal activity of green biosynthesized magnetic Fe_3O_4 nanoparticles using the aqueous extract of corn (*Zea mays* L.) ear leaves. *Artif. Cells Nanomed. Biotechnol.* **2017**, *45* (2), 349–356. https://doi.org/10.3109/21691401.2016.1153484

Patra, J. K.; Baek, K.-H. Green biosynthesis of magnetic iron oxide (Fe_3O_4) nanoparticles using the aqueous extracts of food processing wastes under photo-catalyzed condition and investigation of their antimicrobial and antioxidant activity. *J. Photochem. Photobiol. B, Biol.* **2017**, *173*, 291–300. https://doi.org/10.1016/j.jphotobiol.2017.05.045

Pinkas, J.; Reichlova, V.; Zboril, R.; Moravec, Z., Bezdicka, P.; Matejkova, J. Sonochemical synthesis of amorphous nanoscopic iron(III) oxide from $Fe(acac)_3$. *Ultrason. Sonochem.* **2008**, *15* (3), 257–264. https://doi.org/10.1016/j.ultsonch.2007.03.009

Poka, L. P., Krishna, M. G., Venkateswara, K. R., Shanker, K. Biosynthesis, characterization and acute oral toxicity studies of synthesized iron oxide nanoparticles using ethanolic extract of *Centella asiatica* plant. *Mater. Lett.* **2019**, *236*, 256–259. https://doi.org/10.1016/j.matlet.2018.10.037

Prabhakar, R.; Samadder, S. R.; Jyotsana. Aquatic and terrestrial weed mediated synthesis of iron nanoparticles for possible application in wastewater remediation. *J. Clean. Prod.* **2017**, *168*, 1201–1210. https://doi.org/10.1016/j.jclepro.2017.09.063

Radini, I. A; Hansan, N.; Malik, M. A.; Khan, Z. Biosynthesis of iron nanoparticles using *Trigonella foenum-graecum* seed extract for photocatalytic methyl orange dye degradation and antibacterial applications. *J. Photochem. Photobiol. B, Biol.* **2018**, *183*, 154–163. https://doi.org/10.1016/j.jphotobiol.2018.04.014

Rahmani, R.; Gharanfoli, M.; Gholamin, M.; Darroudi, M.; Chamani, J.; Sadri, K. Green synthesis of ^{99m}Tc-labeled-Fe_3O_4 nanoparticles using Quince seeds extract and evaluation of their cytotoxicity and biodistribution in rats. *J. Mol. Struct.* **2019**, *1196*, 394–402. https://doi.org/10.1016/j.molstruc.2019.06.076

Rahmani, R.; Gharanfoli, M.; Gholamin, M.; Darroudi, M., Chamani, J.; Sadri, K.; Hashemzadeh, A. Plant-mediated synthesis of superparamagnetic iron oxide nanoparticles (SPIONs) using aloe vera and flaxseed extracts and evaluation of their cellular toxicities. *Ceram. Int.* **2020**, *46* (3), 3051–3058. https://doi.org/10.1016/j.ceramint.2019.10.005

Rai, M.; Ingle, A. P.; Gupta, I. R.; Birla, S. S., Yadav, A. P., Abd-Elsalam, K. A. Potential role of biological systems in formation of nanoparticles: mechanism of synthesis and biomedical applications. *Curr. Nanosci.* **2013**, *9* (5), 576–587. https://doi.org/10.2174/15734137113099990092

Rajendran, K.; Karunagaran, V.; Mahanty, B.; Sen, S. Biosynthesis of hematite nanoparticles and its cytotoxic effect on HepG2 cancer cells. *Int. J. Biol. Macromol.* **2015**, *74*, 376–381. https://doi.org/10.1016/j.ijbiomac.2014.12.028

Rajendran, K.; Sen, S. Optimization of process parameters for the rapid biosynthesis of hematite nanoparticles. *J. Photochem. Photobiol. B: Biol.* **2016**, *159*, 82–87. https://doi.org/10.1016/j.jphotobiol.2016.03.023

Rajiv, P.; Bavadharani, B.; Kumar, M. N.; Vanathi, P. Synthesis and characterization of biogenic iron oxide nanoparticles using green chemistry approach and evaluating their biological activities. *Biocatal. Agric. Biotechnol.* **2017**, *12*, 45–49. https://doi.org/10.1016/j.bcab.2017.08.015

Ramesh, A. V.; Devi, D. R.; Botsa, S. M.; Basavaiah, K. Facile green synthesis of Fe_3O_4 nanoparticles using aqueous leaf extract of *Zanthoxylum armatum* DC. for efficient adsorption of methylene blue. *J. Asian Ceram. Soc.* **2018**, *6* (2), 145–155. https://doi.org/10.1080/21870764.2018.1459335

Rana, P.; Sharma, S.; Sharma, R.; Banerjee, K. Apple pectin supported superparamagnetic (γ-Fe_2O_3) maghemite nanoparticles with antimicrobial potency. *Materials Science for Energy Technology* **2019**, *2* (1), 15–21. https://doi.org/10.1016/j.mset.2018.09.001

Ranmadugala, D.; Ebrahiminezhad, A.; Manley-Harris, M.; Ghasemi, Y.; Berenjian, A. Reduced biofilm formation in Menaquinone-7 production process by optimizing the composition of the cultivation medium. *Trends Pharmac. Sci.* **2017**, *3* (4), 245–254.

Ratna, D., Padhi, B. S. Pollution due to synthetic dyes toxicity and carcinogenicity studies and remediation. International Journal of Environmental Science **2012**, *3* (3), 940–955.

Rizwan, W., Farheen, K., Abdulaziz A., Al-Khedhairy, A. Hematite iron oxide nanoparticles: apoptosis of myoblast cancer cells and their arithmetical assessment. *RSC Adv.* **2018**, *8*, 24750–24759. https://doi.org/10.1039/C8RA02613K

Roca, A. G.; Gutiérrez, L.; Gavilán, H.; Fortes Brollo, M. E. F.; Veintemillas-Verdaguer, S.; Morales, M. P. Design strategies for shape-controlled magnetic iron oxide nanoparticles. *Adv. Drug Deliv. Rev.* **2019**, *138*, 68–104. https://doi.org/10.1016/j.addr.2018.12.008

Rufus, A.; Sreeju, N.; Vilas, V.; Philip, D. Biosynthesis of hematite (α-Fe$_2$O$_3$) nanostructures: Size effects on applications in thermal conductivity, catalysis, and antibacterial activity. *J. Mol. Liq.* **2017**, *242*, 537–549. https://doi.org/10.1016/j.molliq.2017.07.057

Rufus, A; Sreeju, N.; Philip, D. Size tunable biosynthesis and luminescence quenching of nanostructured hematite (α-Fe$_2$O$_3$) for catalytic degradation of organic pollutants. *J. Phys. Chem. Solids* **2019**, *124*, 221–234. https://doi.org/10.1016/j.jpcs.2018.09.026

Ruíz-Baltazar, Á. J.; Reyes-López, S. Y.; Mondragón-Sánchez, M. L.; Robles-Cortés, A. I.; Pérez, R. Eco-friendly synthesis of Fe$_3$O$_4$ nanoparticles: Evaluation of their catalytic activity in methylene blue degradation by kinetic adsorption models. *Results Phys.* **2019**, *12*, 989–995. https://doi.org/10.1016/j.rinp.2018.12.037

Saif, S.; Tahir, A.; Chen, Y. Green synthesis of iron nanoparticles and their environmental applications and implications. *Nanomaterials* **2016**, *6* (11), 209. https://doi.org/10.3390/nano6110209

Salem, D. M. S. A.; Ismail, M. M.; Aly-Eldeen, M. A. Biogenic synthesis and antimicrobial potency of iron oxide (Fe$_3$O$_4$) nanoparticles using algae harvested from the Mediterranean Sea, Egypt. *Egypt. J. Aquat. Res.* **2019**, *45* (3), 197–204. https://doi.org/10.1016/j.ejar.2019.07.002

Sathishkumar, G.; Logeshwaran, V.; Sarathbabu, S.; Jha, P. K.; Jeyaraj, M.; Rajkuberan, C.; Senthilkumar, N.; Sivaramakrishnan, S. Green synthesis of magnetic Fe$_3$O$_4$ nanoparticles using *Couroupita guianensis* Aubl. fruit extract for their antibacterial and cytotoxicity activities.

Artif. Cells Nanomed. Biotechnol. **2018**, *46* (3), 589–598. https://doi.org/10.1080/21691401.2017.1332635

Sayed, F. N.; Polshettiwar, V. Facile and Sustainable Synthesis of Shaped Iron Oxide Nanoparticles: Effect of Iron Precursor Salts on the Shapes of Iron Oxides. *Sci. Rep.* **2015**, *5*, 9733. https://doi.org/10.1038/srep09733

Seabra, A. B.; Pelegrino, M. T.; Haddad, P. S. Antimicrobial Applications of Superparamagnetic Iron Oxide Nanoparticles: Perspectives and Challenges. In *Nanostructures for Antimicrobial Therapy*; Ficai, A., Grumezescu, A. M., Eds.; Elsevier, 2017; pp 531-550. https://doi.org/10.1016/B978-0-323-46152-8.00024-X

Sharma, D.; Ledwani, L.; Mehrotra, T.; Kumar, N.; Pervaiz, N.; Kumar, R. Biosynthesis of hematite nanoparticles using *Rheum emodi* and their antimicrobial and anticancerous effects *in vitro*. *J. Photochem. Photobiol. B, Biol.* **2020**, *206*, 111841. https://doi.org/10.1016/j.jphotobiol.2020.111841

Shen, Z.; Wu, A.; Chen, X. Iron oxide nanoparticle-based contrast agents for magnetic resonance imaging. *Mol. Pharmaceutics* **2017**, *14* (5), 1352–1364. https://doi.org/10.1021/acs.molpharmaceut.6b00839

Singh, P.; Kim, Y.-J.; Zhang, D.; Yang, D.-C. Biological Synthesis of Nanoparticles from Plants and Microorganisms. *Trends Biotechnol.* **2016**, *34* (7), 588–599. https://doi.org/10.1016/j.tibtech.2016.02.006

Sirdeshpande, K. D.; Sridhar, A.; Cholkar, K. M.; Selvaraj, R. Structural characterization of mesoporous magnetite nanoparticles synthesized using the leaf extract of *Calliandra haematocephala* and their photocatalytic degradation of malachite green dye. *Appl. Nanosci.* **2018**, *8*, 675–683. https://doi.org/10.1007/s13204-018-0698-8

Sneha, U.; Karthikeyan, R. Bactericidal activity of ayurvedic formulation against cariogenic microorganisms. *Biocatal. Agric. Biotechnol.* **2019**, *18*, 101026. https://doi.org/10.1016/j.bcab.2019.101026

Sorbiun, M.; Mehr, E. S.; Ramazani, A.; Malekzadeh, A. M. Biosynthesis of metallic nanoparticles using plant extracts and evaluation of their antibacterial properties. *Nanochem. Res.* **2018**, *3* (1), 1–16.

Stan, M., Popa, A., Toloman, D.; Dehelean, A.; Lung, I.; Katona, G. Enhanced photocatalytic degradation properties of zinc oxide nanoparticles synthesized by using plant extracts. *Mater. Sci. Semicond. Process.* **2015**, *39*, 23–29. https://doi.org/10.1016/j.mssp.2015.04.038

Sulaiman, G. M.; Tawfeeq, A. T.; Naji, A. S. Biosynthesis, characterization of magnetic iron oxide nanoparticles and evaluations of the cytotoxicity and DNA damage of human breast carcinoma cell lines. *Artif. Cells Nanomed.*

Biotechnol. **2018**, *46* (6), 1215–1229. https://doi.org/10.1080/21691401.2017.1366335

Sumera, A.; Tahir, M. B.; Iqbal, T.; Liaqat, A.; Abrar, M. Green synthesis and characterization of novel iron particles by using different extracts. *J. Alloys Compd.* **2018**, *732*, 935–944. https://doi.org/10.1016/j.jallcom.2017.10.137

Taghizadeh, S.-M.; Berenjian, A., Taghizadeh, S.; Ghasemi, Y.; Taherpour, A.; Sarmah, A. K.; Ebrahiminezhad, A. One-put green synthesis of multifunctional silver iron core-shell nanostructure with antimicrobial and catalytic properties. *Ind. Crops Prod.* **2019**, *130* (2019) 230–236. https://doi.org/10.1016/j.indcrop.2018.12.085

Thandapani, K.; Kathiravan, M.; Namasivayam., E.; Padiksan, I. A.; Natesan, G., Tiwari, M., Giovanni, B., Perumal, V. Enhanced larvicidal, antibacterial, and photocatalytic efficacy of TiO₂ nanohybrids green synthesized using the aqueous leaf extract of *Parthenium hysterophorus*. *Environ. Sci. Pollut. Res.* **2018**, *25*, 10328-10339. https://doi.org/10.1007/s11356-017-9177-0

Thilagavathi, T.; Renuka, R.; Priya, R. S. Bio-synthesis of silver nanoparticles using *Punicagranatum* (Pomegranate) peel extract: a novel approach towards waste utilization. *Int. J. Adv. Sci. Eng.* **2016**, *3* (1), 234–236.

Toledo, L. A. S.; Rosseto, H. C.; Bruschi M. L. Iron oxide magnetic nanoparticles as antimicrobials for therapeutics. *Pharm. Dev. Technol.* **2018**, *23* (4), 316–323. https://doi.org/10.1080/10837450.2017.1337793

Truskewycz, A.; Shukla, R.; Ball, A. S. Iron nanoparticles synthesized using green tea extracts for the fenton-like degradation of concentrated dye mixtures at elevated temperatures. *J. Environ. Chem. Eng.* **2016**, *4* (4) (Part A), 4409–4417. https://doi.org/10.1016/j.jece.2016.10.008

Vallabani, N. V. S.; Singh, S. Recent advances and future prospects of iron oxide nanoparticles in biomedicine and diagnostics. *3 Biotech* **2018**, *8*, 279. https://doi.org/10.1007/s13205-018-1286-z

Vasantharaj, S.; Sathiyavimal, S.; Senthilkumar, P.; LewisOscar, F.; Pugazhendhi, A. Biosynthesis of iron oxide nanoparticles using leaf extract of *Ruellia tuberosa*: antimicrobial properties and their applications in photocatalytic degradation. *J. Photochem. Photobiol. B, Biol.* **2019**, *192*, 74–82. https://doi.org/10.1016/j.jphotobiol.2018.12.025

Verma, A.; Mehata, M. S. Controllable synthesis of silver nanoparticles using Neem leaves and their antimicrobial activity. *J. Radiat. Res. Appl. Sci.* **2016**, *9* (1), 109–115. https://doi.org/10.1016/j.jrras.2015.11.001

Vitta, Y.; Figueroa, M.; Calderon, M., Ciangherotti, C. Synthesis of iron nanoparticles from aqueous extract of *Eucalyptus robusta* Sm and evaluation of antioxidant and antimicrobial activity. *Materials Science for Energy Technologies* **2020**, *3*, 97–103. https://doi.org/10.1016/j.mset.2019.10.014

Wei, F.; Fang, Z.; Zheng, L.; Tan, L.; Tsang, E. P. Green synthesis of Fe nanoparticles using *Citrus maxima* peels aqueous extracts. *Mater. Lett.* **2016**, *185*, 384–386. https://doi.org/10.1016/j.matlet.2016.09.029

Woźnica, A.; Dzirba, J.; Mańka, D.; Łabuzek, S. Effects of electron transport inhibitors on iron reduction in *Aeromonas hydrophila* strain KB1. *Anaerobe* **2003**, *9* (3), 125–130. https://doi.org/10.1016/S1075-9964(03)00059-3

Wu, W.; Wu, Z.; Yu, T.; Jiang, C.; Kim, W.-S. Recent progress on magnetic iron oxide nanoparticles: synthesis, surface functional strategies and biomedical applications. *Sci. Technol. Adv. Mater.* **2015**, *16* (2), 023501. https://doi.org/10.1088/1468-6996/16/2/023501

Yadav, V. K.; Fulekar, M. H. Biogenic synthesis of maghemite nanoparticles (γ-Fe₂O₃) using *Tridax* leaf extract and its application for removal of fly ash heavy metals (Pb, Cd). *Mater. Today: Proc.* **2018**, *5* (9) (Part 3), 20704–20710. https://doi.org/10.1016/j.matpr.2018.06.454

Yazdani, F.; Seddigh, M. Magnetite nanoparticles synthesized by co-precipitation method: The effects of various iron anions on specifications. *Mater. Chem. Phys.* **2016**, *184*, 318–323. https://doi.org/10.1016/j.matchemphys.2016.09.058

Yew, Y. P.; Shameli, K.; Miyake, M.; Khairudin, N. B. B. A.; Mohamad, S. E. B.; Naiki, T.; Lee, K. X. Green biosynthesis of superparamagnetic magnetite Fe₃O₄ nanoparticles and biomedical applications in targeted anticancer drug delivery system: A review. *Arab. J. Chem.* **2020**, *13* (1), 2287–2308. https://doi.org/10.1016/j.arabjc.2018.04.013

Zhu, M.; Wang, Y.; Meng, D.; Qin, X.; Diao, G. Hydrothermal synthesis of hematite nanoparticles and their electrochemical properties. *J. Phys. Chem. C* **2012**, *116* (30), 16276–16285. https://doi.org/10.1021/jp304041m

Bioadsorption of lead(II) over the pulp of *Acrocomia aculeata*

Alexandra Novak[1+], Fátima Yubero[1], Diana Diez-Pérez-Núñez[1], Fernando Luis Fertonani[2], Brenda Gisselle Da Silva Britez[1], Yenny Gonzalez[1]

1. National University of Asunción, Faculty of Chemical Sciences, San Lorenzo, Paraguay.
2. São Paulo State University, Institute of Biosciences, Languages and Exact Sciences, São José do Rio Preto, Brazil.

+Corresponding author: Alexandra Novak, Phone: +1 585-281-0077, Email address: at.novak23@gmail.com

ABSTRACT: The adsorption of lead in aqueous solution onto *Acrocomia aculeata* pulp was examined. The pulp was characterized in the presence and absence of lead using Fourier transform infrared spectroscopy (FTIR), thermogravimetric analysis (TG-DTA), and scanning electron microscopy (SEM). Sulfur and oxygen bonds were responsible for adsorbing lead onto the pulp surface. The TG-DTA profile proved that adding sodium azide increases the pulp's thermal stability until 200 °C. Adsorption data in batch and column systems were analyzed to understand the pulp adsorption compared to other biomaterials. In the batch experiments, the removal efficiency reached a maximum of 91.9% when a solution of 50 ppm of lead was placed in contact with the pulp for 30 min and fit Freundlich isotherm behavior. In the column experiments, the theoretical maximum adsorption capacity was found to be 11.97 mg g^{-1}; more column data is needed to compare column results to other studies. Further studies to improve the pulp adsorption capacity are needed for it to be a competitive biomaterial for water treatment.
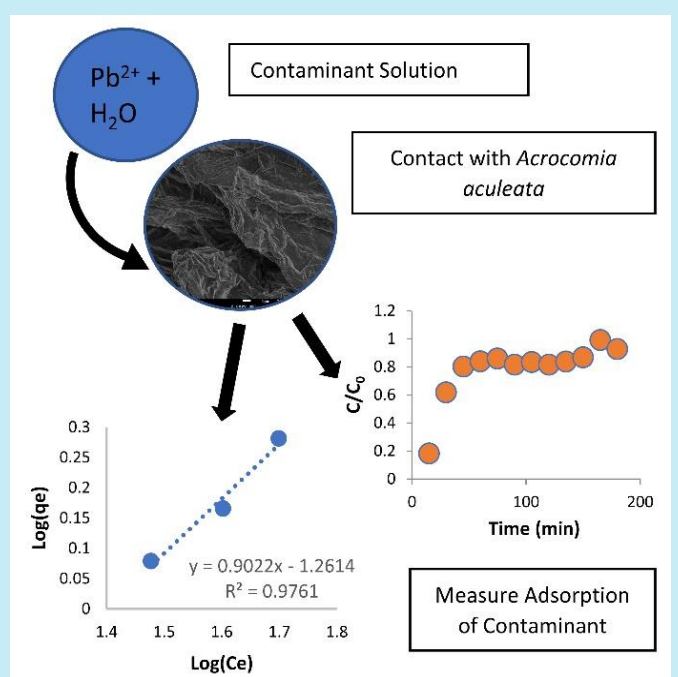
1. Introduction

Lead is one of the five most harmful elements to human health (Tchounwou *et al*., 2012). Due to its high bioavailability, lack of biological function, and persistence in the environment, it is extremely toxic to ecosystems and living organisms (Jaishankar *et al*., 2014; Tchounwou *et al*., 2012). Some toxic effects of lead include damage to the central and peripheral nervous system, birth defects, inhibition of plant growth, and ecosystem bioaccumulation (Cardwell *et al*., 2013; Flora *et al*., 2012; Goyer, 1993; Jaishankar *et al*., 2014).

Though lead is naturally occurring, the majority of lead contamination results from anthropogenic sources (Tchounwou *et al*., 2012). Industrial sources of lead include fossil fuels, production of metals, mining, soldering, battery production, and pipping. Domestic sources of lead include decorative paint, children's toys, and cosmetics (Flora *et al*., 2012; Jaishankar *et al*., 2014; Tchounwou *et al*., 2012). Humans are exposed to lead from these products via respiration of dust containing lead or the ingestion of contaminated water. Cases of lead contamination are found on every continent, excluding Antarctica, and 49% of children and 52% of adults in the world have blood levels of lead higher than 5 ug dL^{-1} (Kessler, 2014). Thus, it can be concluded that lead contamination is a global public health crisis (Tong *et al*., 2000).

The World Health Organization standard for lead in potable water is below 0.01 ppm, recommending that contaminated water be treated so that lead levels are below the standard (WHO, 2006). The most common methods of water treatment for lead are chemical precipitation and ionic exchange. Chemical precipitation uses hydroxides and sulfides to produce a solid precipitate containing lead. This process is fast and easy to control, however, the chemicals used and the disposal of toxic solids generate high operation costs. Ionic exchange uses a synthetic organic resin to attract soluble ions from a liquid phase to a solid phase. Although this method has low operation costs, it is very sensitive to pH changes and only works with low concentrations of lead (Gunatilake, 2015).

Bioadsorption is an alternative method for treating water contaminated with heavy metals such as lead. In this study, bioadsorption is defined as the mass transfer of a substance to the surface of a biomass-derived solid via physical and chemical interactions. Bioadsorption is efficient in purification and separation, low cost, and easy to control. Furthermore, it is a process that is environmentally friendly. Common materials for bioadsorption include agricultural wastes, biopolymers, and industrial byproducts (Gunatilake, 2015).

In Paraguay, a biomaterial of interest is the coconut palm *Acrocomia aculeata*, known by its common name as "mbokayá" (Yubero *et al*., 2015). *Acrocomia aculeata* is a species native to South America with a high cultivation potential in Paraguay, home to over 4,546,000 hectares of the species (Plath *et al*., 2016). Unlike the African palm and soy, *A. aculeata* can be grown in a mixed culture and in infertile, sandy soils (Poetsch *et al*., 2012; Roman, 1996). This means that its cultivation does not compete with the nutrient-rich rainforest soil nor causes the loss of biodiversity associated with land clearing for monocultures (Plath *et al*., 2016). As this palm survives in extremely low temperatures, fire, and drought, it is resistant to extreme weather events brought on by climate change (Poetsch *et al*., 2012). The kernel oil from the coconut is already used in a variety of local products and industries in Paraguay, such as food, biofuel, cosmetics, and medicinal soap, and thus is an important economic resource for the country (Poetsch *et al*., 2012; Roman, 1996).

In addition to the environmental, social, and economic benefits of *A. aculeata*, the pulp of the coconut, a byproduct of kernel oil extraction, has proven capabilities in the bioadsorption of heavy metals from water. According to Yubero et. al (2015), the pulp of *A. aculeata* can adsorb up to 66% of chromium (VI), another heavy metal toxic to human health. Thus, it is probable that this material could effectively remove other heavy metals such as lead. This study aims to explore *A. aculeata* as a sustainable material for lead bioadsorption through the characterization of the pulp composition and structure and the analysis of lead adsorption in both column and batch systems.

2. Experimental

2.1 Pulp preparation

The coconuts were collected in February of 2016, in semi-open field at the Jack Norment Camp in Caacupé, Paraguay. The pulp was processed by the Botany and Physical Chemistry Departments at Universidad Nacional de Asunción. First, the epicarp was removed and mesocarp cuts were made. The slightly insoluble fibers were then dried at 40 °C for two days (González *et al*., 2018; Yubero *et al*., 2016a; b). The size of the dry fiber was sieved for size selection, to be between 297 and 350 µm. To conserve the fiber, 0.5 g of

sodium azide was added and homogenized in about 4 g of the size-selected fiber.

2.2 Characterization methods

Fourier transform infrared spectroscopy (FTIR) analysis from 500–4000 cm^{-1} was conducted on the native pulp and the pulp in contact with a 25 ppm Pb(II) solution for 5 min, 30 min, and 5 h, using the Shimadzu Europa GmbH IR Prestige-21. Thermogravimetric analysis (TG-DTA) was carried out using TA Instruments ST 2960 Simultaneous DTA-DTG on a sample of m = 5.6 mg of native pulp/sodium azide mix. The sample was heated at β = 20 °C min^{-1} under air atmosphere (100 mL min^{-1}) in an open aluminum crucible (70 μL) during thermogravimetric analysis (TG-DAT analysis. Scanning electron microscopy (SEM) images of the pulp azide mix after contact with Pb(II) were taken using FEG-SEM JEOL Model 7500F.

2.3 Solution preparation

The distilled water was tested with a PHS-38W microprocessor from Bante Instruments. The pH was found to have a pH of 5.84 at 25.4 °C. As lead has a solubility between a pH of 2 to 7, distilled water was used in the following solutions (Wang *et al.*, 2017). Lead nitrate, Pb(NO$_3$)$_2$, were used in the preparation of all solutions.

A 1 L solution of 50 ppm Pb(NO$_3$)$_2$ was prepared using 50 mg of anhydrous Pb(NO$_3$)$_2$. Solutions of 30, 40, and 50 ppm Pb(NO$_3$)$_2$ were prepared by adding 30, 40, and 50 mL of the 50 ppm Pb(NO$_3$)$_2$ solution to 50 mL volumetric flasks and filling them with distilled water.

2.4 Batch study

To prepare the pulp for batch experiments, 200 mg samples of the pulp were washed three times with 25 mL of distilled water. The batch experiment was carried out by adding a sample of 200 mg of pulp to a 13 mL solution with an initial concentration of either 30, 40, or 50 ppm Pb(II) to conical centrifuge tubes. Each sample was rotated for a required time of either 5 min, 30 min, and 5 h at 8 rpm. Next, the pulp and solution were centrifuged for 5 min at 6000 rpm. The supernatant was extracted and the final concentration of Pb(II) was tested using AA-6300 Shimadzu atomic absorption spectrometer. It must be noted that this experiment was performed in duplicate (i.e. two

samples of pulp in contact with 30 ppm Pb(II) for 5 min, two samples in contact with 30 ppm Pb (II) for 30 min).

The Langmuir (Eq. 1) and Freundlich (Eq. 2) adsorption isotherms were applied to the batch data using the following equations.

$$\frac{1}{q_e} = \frac{1}{K_L q_m}\frac{1}{c_i} + \frac{1}{Q_m} \tag{1}$$

$$log q_e = log K_F + \frac{1}{n} log c_i \tag{2}$$

where K_L is the Langmuir constant (L mg^{-1}), q_m is the maximum adsorbed capacity (when the adsorbate monolayer has formed, mg g^{-1}), K_F is the Freundlich constant for adsorption capacity (L mg^{-1}), n is Freundlich constant for adsorption intensity, and c_i is the initial concentration adsorbate in solution (mg L^{-1}). q_e is the adsorption capacity at equilibrium (mg g^{-1}), solved for using Eq. 3.

$$q_e = \frac{c_i - c_f}{m} \times V \tag{3}$$

where c_f is the final solution (mg L^{-1}), m is the mass of adsorbent (g), and V is the volume of solution (L).

Removal efficiency (Eq. 4) was also calculated for batch data using the following equation.

$$Removal Efficiency = \frac{c_i - c_f}{c_i} x 100 \tag{4}$$

2.5 Column study

A 5 mL syringe with needle was used as the column. A sheet of packing plastic was placed at the bottom of the syringe and 200 mg of pulp were loaded into the column. The syringe needle was connected to a tube that fed through a peristaltic pump that regulated a flow rate of 4 mL min^{-1}, as seen in Fig. 1.

Twenty-five mL of distilled water were passed through the column to stabilize the column bed. After the pulp was stabilized, a 35 ppm Pb(II) solution was continuously passed through the column. Over a 3-time period, 15 mL samples of effluent solution were collected every 15 min in conical centrifuge tubes. In between sampling times, the effluent was collected in a waste beaker. The levels of Pb(II) in the conical centrifuge tube samples were tested using atomic absorption spectroscopy.
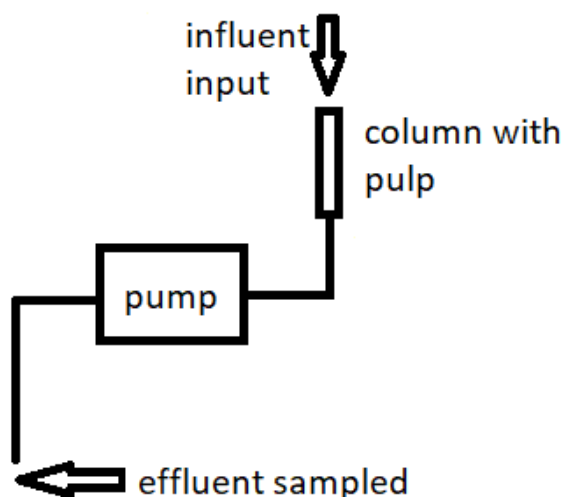
Figure 1. Column experiment configuration.

The Thomas (Eq. 5) and Yoon-Nelson (Eq. 6) models were applied to column data using the following equations.

$$ln\left[\left(\frac{C_o}{C_t}\right) - 1\right] = \frac{K_{TH}q_{TH}m}{Q} + K_{TH}C_o t \qquad (5)$$

where C_o is the original concentration of the solution (mg L^{-1}), C_t is the concentration of the effluent solution (mg L^{-1}), Q is the flow rate (mL min^{-1}), K_{TH} is the Thomas model constant (mL mg^{-1} min^{-1}), q_{TH} is the theoretical adsorption capacity, and t is the time (min).

$$ln\left(\frac{C_t}{C_o - C_t}\right) = tK_{YN} - \tau K_{YN} \qquad (6)$$

where C_o is the original concentration of the solution (mg L^{-1}), C_t is the concentration of the effluent solution (mg L^{-1}), flow rate of the influent solution (mL min^{-1}), t is the time (min), K_{YN} is the Yoon-Nelson constant (min^{-1}), and τ is the time to reach 50% saturation of the column.

3. Results and discussion

3.1 Materials characterization

The data for the infrared (IR) spectrum of the native pulp is found in Tab. 1. The native pulp had a characteristic fingerprint region, defined by bands 1–8 in Tab. 1, with representative bands at 1735, 1374, and 1064 cm^{-1} (Yubero *et al.*, 2015). These bands correspond with C=N/C=O, C-O-C, and C=S/S=O bonds (Chang, 1981).

Table 1. Fourier transform infrared (FTIR) spectrum bands of *A. aculeata* pulp.

	Band/cm^{-1}	Intensity	Area/a.u. cm^{-1}
1	996	1.260	27.17
2	1034	1.404	64.96
3	1068	1.426	4.12
4	1160	1.272	46.69
5	1249	1.331	72.19
6	1330	1.219	9.39
7	1378	1.291	12.37
8	1735	1.366	7.72
9	2348	1.209	10.41
10	2374	1.204	19.64
11	2866	1.281	8.64
12	2922	1.320	20.30
13	3005	1.271	8.58

When the pulp was in contact with a 25 ppm Pb(II) solution, the bands in the fingerprint region shrink in intensity as the contact time with the lead solution increased, as seen in Fig. 2. This change in intensity, an indicator of change in dipole movement, indicates that the oxygen and sulfur bonds are most likely involved in capturing the Pb(II). Additionally, a band appears at around 2300 cm^{-1} in the Pb(II) contact spectra, highlighted in Fig. 2, at a stronger intensity than in the raw pulp IR spectrum. This band could indicate the presence of Pb(II) nitrate.
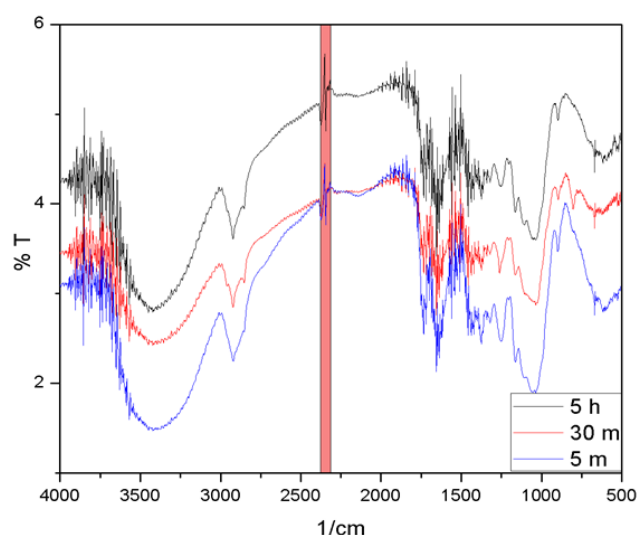

Figure 2. Fourier transform infrared spectrum (FTIR) of *A. aculeata* pulp in contact with 25 ppm Pb(II) solution for 5 min, 30 min, and 5 h; insert: expanded region of 2340–2380 cm^{-1}.

The results of the scanning electron microscopy (SEM) imaging are found in Fig. 3. These images reveal the pulp to have a rough, fibrous surface texture.

The thermogravimetric analysis (TGA) profile of the pulp azide mixture (Fig. 4) was compared to the TGA of *A. aculeata* pulp in absence of sodium azide, from Fig. 4. It must be noted that in Corrêa *et al*. (2019) the pulp was heated at 10 °C min⁻¹ under synthetic air while the conditions for this experiment was 20 °C min⁻¹. The raw pulp had four decomposition steps, while the thermogravimetric/derivative thermogravimetric (TG/DTG) curves of the pulp sodium azide mixture reveals that there are three distinct decomposition steps (Fig. 4). In the raw pulp TG/DTG curve, the first step occurred between room temperature and 160 °C and was endothermic due to the presence of water in the fibers (Corrêa *et al*., 2019). Similarly, the first step in the pulp azide mechanical mixture is endothermic between 25 and 100 °C and can be associated with water molecule evolution.

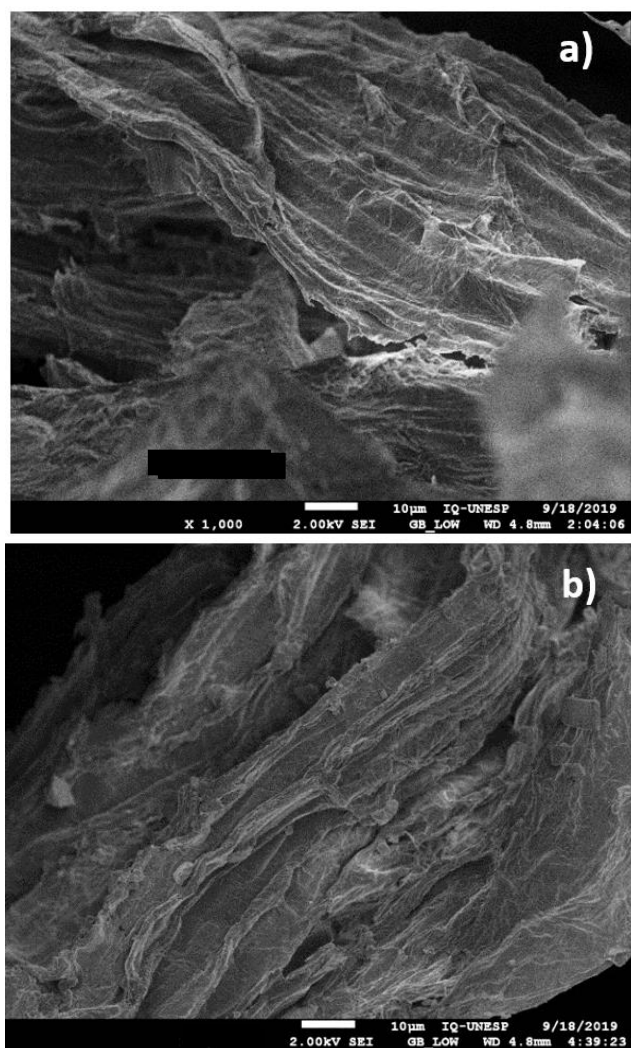and backscatter electron) image of *A. aculeata* pulp with Pb(II) in **(a)** batch and **(b)** column.
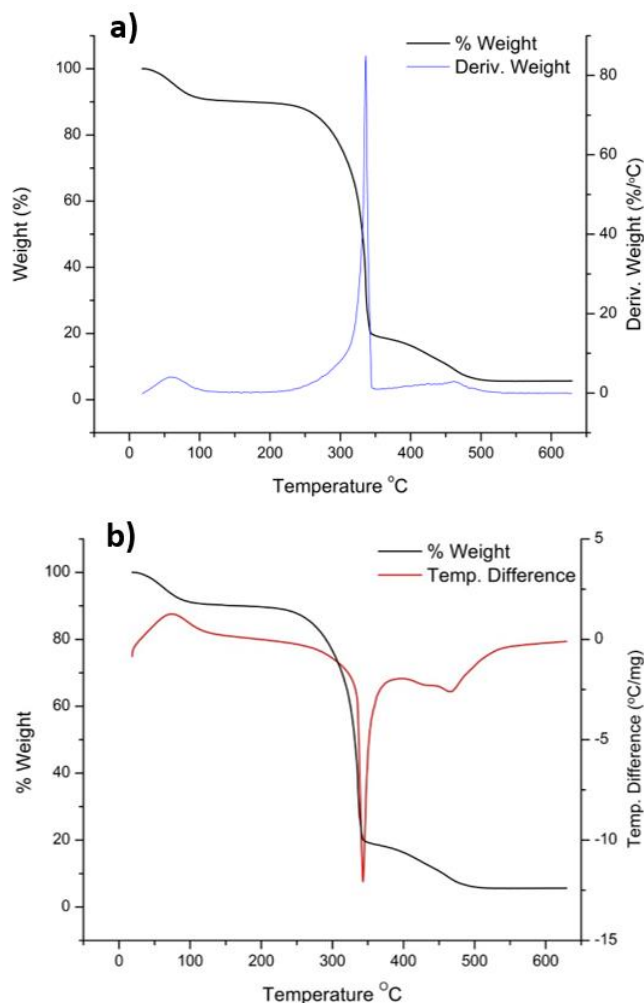

Figure 4. Thermogravemetric analysis (TGA) profile of *A. aculeata* pulp, % weight with **(a)** TG and DTG and **(b)** TG-DTA; mass sample of 5.6 mg; β = 20 °C min⁻¹; air (100 mL min⁻¹); open aluminum crucible (70 L).

Figure 3. Field emission gun scanning electron microscope (FEG-SEM) mixed (secondary electron

The next decomposition step in the raw pulp TGA was exothermic and the largest; it occurred between approximately 190 and 300 °C and can be attributed to the decomposition of hemicellulose and cellulose. This step was followed by two small exothermic mass losses between approximately 390 and 425 °C that can be attributed to the decomposition of lignin (Corrêa *et al*., 2019). On the other hand, the pulp azide mixture demonstrated thermal stability until about 200 °C, proving that the sodium azide causes a slight stabilization in the material. The following step for the sodium azide mixture is strongly exothermic and can be associated with the kinetically fast decomposition of

cellulose and the formation of the metallic Na species from sodium azide, which both simultaneously occur between 200 and 340 °C. The largest percentage weight loss occurs during this step at $T^{DTA}_{peak} = 336$ °C, which is right around the temperature that sodium azide decomposes according to literature. It can be concluded that the presence of sodium azide accelerates the decomposition of the material in this step. The residues from the decomposition reaction of cellulose and sodium azide to metallic Na then decomposes in the step between 350 and 510 °C. The DTG and DTA curves are in agreement with each other and the literature, revealing two small peaks that are associated with the slow kinetics steps of consecutive reactions (Fujimoto *et al.*, 1990). A total of 94.3% of the pulp sodium azide mixture decomposed.

3.2 Batch study

In the batch study, the removal efficiency (see Eq. 4), or performance in terms of amount of lead removed was found to reach a maximum of 91.9% when a 13 mL solution of 50 ppm of Pb(II) was placed in contact with 200 mg of pulp for 30 min. The Langmuir and Freundlich adsorption isotherms for 5 min of contact with the lead solution are found in Figs. 5 and 6, respectively. It is important to note that most results from the 5 h and 30 min contact time were found to be under the limit of quantification of the instrument (6.30 ppm Pb(II)), so these isotherms were not included in this paper (Silva, 2016). The results from the application of the Langmuir and Freundlich isotherm models applied to the batch results are summarized in Tab. 2.
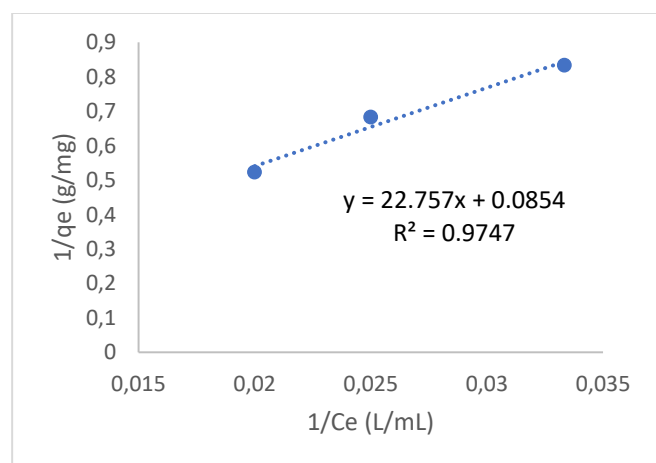

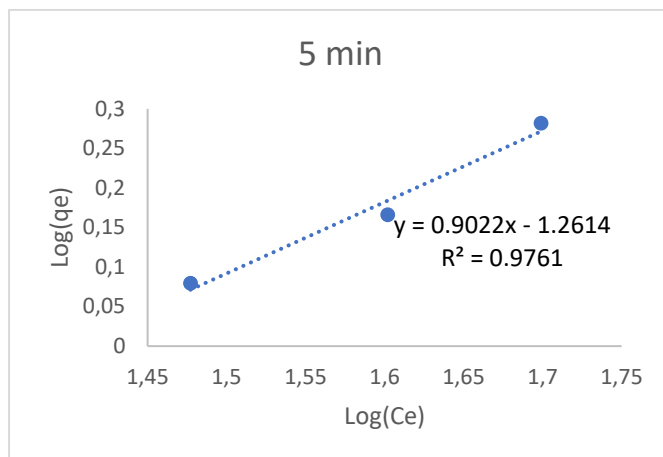**Figure 5.** Langmuir isotherm of Pb(II) adsorption for 5 min contact time with *A. aculeata*.

Figure 6. Freundlich isotherm of Pb(II) adsorption for 5 min contact time with *A. aculeata*.

Table 2. Langmuir and Freundlich isotherms of Pb(II) adsorption in batch for 5 min contact time.

| Langmuir isotherm			Freundlich isotherm		
q_m	K_L	R^2	K_L	n	R^2
11.71	0.0037	0.9747	0.0548	1.108	0.9761

The R^2 value suggest that the Freundlich model fits the adsorption behavior slightly more than the Langmuir model. This indicates that the distribution of surface energy is heterogenous. The Freundlich model also is in accordance with the SEM images, as Freundlich adsorption commonly occurs on rough surfaces (Fig. 3) (Chang, 1981). The *n* value, the Freundlich constant for adsorption intensity is greater than 1, which indicates that the adsorption reaction is kinetically favorable. The Freundlich constant for adsorption capacity, K_F, however, is low compared to other biomaterials in batch, as seen in Tab. 3. The pulp was found to have a low adsorption capacity, q_e (Eq. 3), of 2.3 mg g^{-1} in comparison to other biomaterials (Tab. 3). Since the adsorption capacity defines the amount of adsorbate taken up by the adsorbent, the low value indicates that it is not a promising biomaterial for filtration (Tab. 3). Future optimization studies regarding ideal conditions for adsorption or chemical treatment of the material are needed to improve the adsorption capacity.

Table 3. Comparison of Freundlich adsorption parameters for various biomaterials.

Material	Source	KF	n	R^2	qe (mg g^{-1})
Corn cobs	Stefan *et al.*, 2010	0.40	1.5	0.8794	N/A
Hazelnut shell	Pehlivan *et al.*, 2009	4.28	1.6	0.9360	28.18
Almond shell	Pehlivan *et al.*, 2009	0.18	1.9	0.9260	8.08
Activated carbon	Singanan, 2011	1.25	3.5	0.9626	N/A
Rice husk	Zulkali *et al.*, 2006	0.81	1.9	0.9851	5.69
Modified peanut husk	Li *et al.*, 2007	0.34	0.5	0.9773	4.66
A. Aculeata pulp	This study	0.05	1.1	0.9761	2.30

3.3 Column study

The experimental breakthrough curve from the column experiment is found in Fig. 7 and the breakthrough parameters, along with the Thomas and Yoon-Nelson results, are summarized in Tab. 4. The breakthrough curve resembles the typical shape for column adsorption. The breakthrough time, which is defined as the time at which the concentration of the effluent solution is equal to 5% of the influent concentration, occurs in the first 15 min. This signifies an efficient mass transfer rate. The exhaustion time, the time at which the concentration of the effluent solution reaches 95% of the influent concentration, was found to occur between 2.50 and 2.75 h. The long exhaustion time indicates that the pulp-column system would have a long operating life.
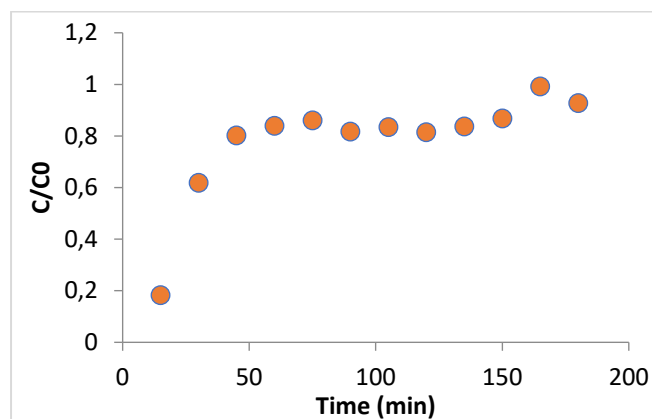
Figure 7. Experimental breakthrough curve for Pb(II) adsorbed on *A. aculeata* pulp.

Table 4. The parameters in fixed-bed experiments for adsorption of Pb(II) on *A. aculeata*.

Thomas model			Yoon-Nelson model			Breakthrough parameters		
K_{TH} (mL mg^{-1} min^{-1})	q_{TH} (mg g^{-1})	R^2	K_{YN} (1/min)	T (min)	R^2	t$_b$ (min)	t$_e$ (min)	R$_q$
0.5714	11.97	0.5782	0.020	17.15	0.5782	0–15	150–165	1.022

The Thomas (Eq. 5) and Yoon-Nelson (Eq. 6) are mathematical models for Langmuir adsorption used to describe the performance of the column. The Thomas model is typically used to calculate q_{th}, the theoretical adsorption capacity of the pulp, which describes the maximum solid phase concentration of Pb(II) on the pulp. This was found to be 11.97 mg g^{-1}. The Yoon-Nelson model is a model for fixed bed, single component adsorption that assumes the decrease in probability of adsorption for each Pb(II) molecule is proportionate to the probability of breakthrough on the pulp by the Pb(II). When applied to the data from the column study, the Thomas and Yoon-Nelson models had low R^2 and, therefore, did not fit the adsorption behavior of Pb(II) (Tab. 2). The R_q, which is the ratio of the theoretical adsorption maximum in column compared to batch, was calculated using the results from the Thomas model in column and Langmuir model. The ratio of 1.022 shows that the column and

batch systems have almost equal efficiency in adsorption of Pb(II), however, as the adsorption does not follow Langmuir behavior and the Thomas and Yoon-Nelson models have poor R^2 coefficients, the column results cannot truly compare the efficacies of both systems. It is necessary that more column data be collected so that an accurate performance assessment can be made.

4. Conclusions

The IR characterization revealed that bonds containing oxygen and sulfur were involved in the adsorption of Pb(II) ions from water. The TGA analysis demonstrated that sodium azide increases the pulp stability. In accordance with the rough surface revealed from the SEM images, the pulp adsorption of Pb(II) specie follows the Freundlich model preferentially, indicating that the binding sites have a

heterogenous distribution of energy and do not form a single layer. The adsorption parameters in batch, however, indicate lower performance when compared to other biomaterials. While the breakthrough curve from the column experiments demonstrated efficiency and operation durability, more column experiments need to be conducted in order to determine which model best describes the adsorption behavior and performance. Future studies on improving the adsorption capacity of *A. aculeata* are needed to understand this biomaterial full capabilities as a sustainable water treatment for Pb(II).

Authors' contribution

Conceptualization: Novak, A.; Yubero, F.
Data curation: Novak, A.
Formal Analysis: Novak, A.
Funding acquisition: Novak, A.
Investigation: Novak, A.; Yubero, F.; Diez-Pérez-Núñez, D.; Fertonani, F. L.; Da Silva Britez, B. G.; González, Y.
Methodology: Novak, A.; Yubero, F.; Diez-Pérez-Núñez, D.; Fertonani, F. L.
Project Administration: Novak, A.; Yubero, F.
Resources: Yubero, F.; Diez-Pérez-Núñez, D.; Fertonani, F. L.; González, Y.
Software: Not applicable
Supervision: Yubero, F.; Fertonani, F. L.
Validation: Yubero, F.; Diez-Pérez-Núñez, D.; Fertonani, F. L.; González, Y.
Visualization: Novak, A.
Writing – original draft: Novak, A.
Writing – review & editing: Novak, A.; Yubero, F.; Fertonani, F. L.

Data availability statement

All data in this report is licensed under creative commons.

References

Cardwell, R. D.; DeForest, D. K.; Brix, K. V.; Adams, W. J. Do Cd, Cu, Ni, Pb, and Zn biomagnify in aquatic ecosystems. In *Reviews of Environmental Contamination and Toxicology*; Springer, 2013; pp 101–122. https://doi.org/10.1007/978-1-4614-6898-1_4

Chang, R. *Physical chemistry with applications to biological systems*; Collier Macmillan, 1981.

Corrêa, A. C.; Carmona, V. B.; Simão, J. A.; Galvani, F.; Marconcini, J. M.; Mattoso, L. H. C. Cellulose Nanocrystals from Fibers of Macauba (*Acrocomia Aculeata*) and Gravata (*Bromelia Balansae*) from Brazilian Pantanal. *Polymers* **2019**, *11* (11), 1785. https://doi.org/10.3390/polym11111785

Flora, G.; Gupta, D.; Tiwari, A. Toxicity of lead: a review with recent updates. *Interdiscip. Toxicol.* **2012**, *5* (2), 47–58. https://doi.org/10.2478/v10102-012-0009-2

Fujimoto, Y.; Ando, T.; Morisaki, S. Thermal stability of sodium azide. Azi ka natorium no netsu anteisei. *Kogyo Kayaku* **1990**, *51* (3), 148–156.

González, Y.; García, M. G.; Arrúa, R. D.; López, M.; Bernal, C.; Ayala, J.; Yubero, F. Morfología, anatomía estructural y actividad lipasa de la pulpa de "coco", *Acrocomia aculeata* (Jacq) Lodd. ex Mart. (Arecaceae) en función al tiempo de colecta. *Rojasiana* **2018**, *17* (1), 73–80.

Goyer, R. A. Lead toxicity: current concerns. *Environ. Health Perspect.* **1993**, *100*, 177–187. https://doi.org/10.1289/ehp.93100177

Gunatilake, S. K. Methods of removing heavy metals from industrial wastewater. *J. Multidiscip. Eng. Sci. Stud.* **2015**, *1* (1), 12–18.

Jaishankar, M.; Tseten, T.; Anbalagan, N.; Mathew, B. B.; Beeregowda, K. N. Toxicity, mechanism and health effects of some heavy metals. *Interdiscip. Toxicol.* **2014**, *7* (2), 60–72. https://doi.org/10.2478/intox-2014-0009

Kessler, R. Lead-based decorative paints: where are they still sold—and why? *Environ. Health Perspect.* **2014**, *122* (4), A97–A103. https://doi.org/10.1289/ehp.122-A96

Li, Q.; Zhai, J.; Zhang, W.; Wang, M.; Zhou, J. Kinetic studies of adsorption of Pb (II), Cr (III) and Cu (II) from aqueous solution by sawdust and modified peanut husk. *J. Hazard. Mater.* **2007**, *141* (1), 163–167. https://doi.org/10.1016/j.jhazmat.2006.06.109

World Health Organization. *Guías para la calidad del agua potable*; WHO, 2006. https://www.who.int/water_sanitation_health/dwq/gdwq3_es_fulll_lowsres.pdf (accessed 2021-31-08).

Pehlivan, E.; Altun, T.; Cetin, S.; Bhanger, M. I. Lead sorption by waste biomass of hazelnut and almond shell. *J. Hazard. Mater*. **2009**, *167* (1–3), 1203–1208. https://doi.org/10.1016/j.jhazmat.2009.01.126

Plath, M.; Moser, C.; Bailis, R.; Brandt, P.; Hirsch, H.; Klein, A.-M.; Walmsley, D.; von Wehrden, H. A novel bioenergy feedstock in Latin America? Cultivation potential of *Acrocomia aculeata* under current and future climate conditions. *Biomass Bioenergy* **2016**, *91*, 186–195. https://doi.org/10.1016/j.biombioe.2016.04.009

Poetsch, J.; Haupenthal, D.; Lewandowski, I.; Oberländer, D., Hilger, T. *Acrocomia aculeata* – a sustainable oil crop. *Rural* **2012**, *21* (3), 41–44.

Roman, C. J. C. Análisis de um sub-sector de la industria de Productos no Maderables del Bosque (PNMB) del Paraguay. *Kaàguy Revista Forestal del Paraguay* **1996**, *12* (1), 41–47.

Silva, R. J. N. B. Spreadsheet for designing valid least-squares calibrations: A tutorial. *Talanta*. **2016**, *148*, 177–190. https://doi.org/10.1016/j.talanta.2015.10.072

Singanan, M. Removal of lead (II) and cadmium (II) ions from wastewater using activated biocarbon. *Science Asia* **2011**, *37*, 115–119. https://doi.org/10.2306/scienceasia1513-1874.2011.37.115

Stefan, D. S.; Belcu, M.; Stefan, M.; Marinescu, I. A. Sorption of Hg^{2+} and Pb^{2+} ions from aqueous solutions on corn cobs biomaterials. *Rev. Chim.* **2010**, *61* (1), 31–35.

Tchounwou, P. B.; Yedjou, C. G.; Patlolla, A. K.; Sutton, D. J. Heavy metal toxicity and the environment. In *Molecular, Clinical and Environmental Toxicology*; Luch, A., Ed.; Springer, 2012; pp 133–164. https://doi.org/10.1007/978-3-7643-8340-4_6

Tong, S.; von Schirnding, Y. E.; Prapamontol, T. Environmental lead exposure: a public health problem of global dimensions. *Bull. World Health Organ.* **2000**, *78* (9), 1068–1077.

Wang, X.; Wang, L.; Wang, Y.; Tan, R.; Ke, X.; Zhou, X.; Geng, J.; Hou, H.; Zhou, M. Calcium sulfate hemihydrate whiskers obtained from flue gas desulfurization gypsum and used for the adsorption removal of lead. *Crystals* **2017**, *7* (9), 270. https://doi.org/10.3390/cryst7090270

Yubero, F.; Ayala, J.; López, M.; Valdovinos, V.; Bernal, C.; González, Y. Polvo insoluble de pulpa de coco (*Acrocomia aculeata*) como biocatalizador. In *XXV Congreso Iberoamericano de Catálisis (CICat 2016)*, Montevideo, Uruguay, September 18–23, 2016a.

Yubero, F.; Ayala, J.; Lopez, M., Valdovinos, V.; Monteiro, M.; Gonzalez, Y.; Thompson, W.; Arguello, J. Physicochemical characteristics of the coconut pulp (*Acrocomia aculeata*) for use as support of proteins and metal material. In *22 Congreso Brasilero de Ingenieria y Ciencia de los Materiales (CBCIMAT 2016)*, Natal, Brazil, November 6–10, 2016b.

Yubero, F.; Oviedo, C.; Arango, M. Biomateriales de fuentes naturales para la retención de Cromo (VI). *Rev. Soc. Cient. Parag.* **2015**, *20* (2), 135–143.

Zulkali, M. M. D.; Ahmad, A. L.; Norulakmal, N. H.; Sharifah, N. S. Comparative studies of *Oryza sativa* L. husk and chitosan as lead adsorbent. *J. Chem. Technol. Biotechnol.* **2006**, *81* (7), 1324–1327. https://doi.org/10.1002/jctb.1429

Variability levels of selected amino acids among mandarins produced in Uruguay

Sofía Rezende[1,2], Sabrina Banchero[2], Ignacio Migues[3], María Veronica Cesio[3], Carlos Fernando Rivas[4], Horacio Heinzen[3], María Natalia Besil[1+]

1. University of the Republic of Uruguay, Chemistry Department of Litoral, Paysandú, Uruguay.
2. Technological University, Southwest Regional Technological Institute, Paysandú, Uruguay.
3. University of the Republic of Uruguay, Faculty of Chemistry, Montevideo, Uruguay.
4. National Institute for Agricultural Research, Salto, Uruguay.

+**Corresponding author:** María Natalia Besil, **Phone:** +598-4722-7950, **Email address:** nbesil@fq.edu.uy

ABSTRACT: Nutraceutical properties of mandarins are of great interest to promote their consumption. The occurrence of free amino acids in foods is relevant to assess the nutritional value of it. To learn more about the amino acids' occurrence and variability between species, a targeted metabolomics study in 'Ellendale', 'Willowleaf' and 'Page' varieties was performed through ion exchange liquid chromatography coupled to tandem mass spectrometry. The studied amino acids were asparagine, glutamic acid, glutamine, histidine, methionine, phenylalanine, proline, threonine and tyrosine. The difference between two consecutive seasons was evaluated, as well as the influence of fruit maturity of 'Page' collected in two periods of 2015. The analytical methodology was validated. The concentration of the compounds through principal component analysis, separated well apart the three cultivars in both harvests, showing a particular profile for each of them. When comparing mature and immature cultivar 'Page', the amino acids with higher levels in mature samples were histidine, asparagine, glutamine and glutamic acid. The profiles were different due to genetic diversity, and the climatic conditions. These results add value to citric production.
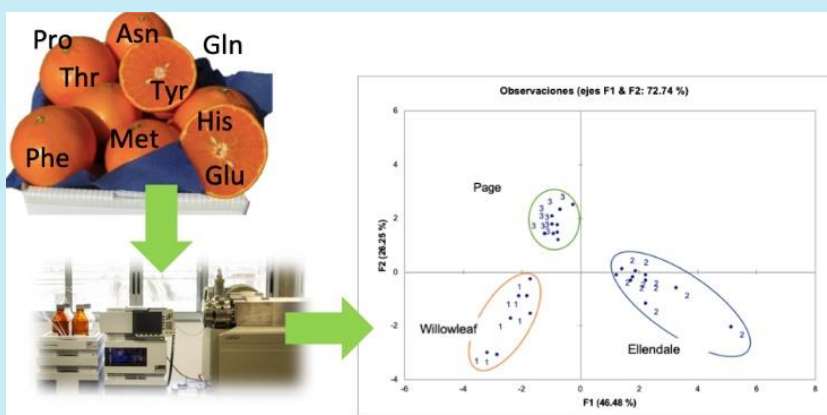
1. Introduction

In recent years, the consumption of healthy foods by the world population has been increasing. The knowledge on food composition seeking a healthier life boosts consumer demand for foods with low amounts of additives, fewer colorants, nontransgenic, with beneficial health properties beyond their own nutritional capacity (Fernández, 2007).

Particularly, citrus fruits contain nutritious ingredients and their consumption is associated with a reduction in the risk of cardiovascular diseases, diabetes and cancer, linked to the presence of flavonoids among other compounds with antioxidant and anti-inflammatory activity (Khan *et al*., 2014; Xi *et al*., 2014). Nevertheless, the presence and contribution of amino acids to the healthy properties of citrus fruits has not been acknowledged in recent reviews (Lado *et al*., 2018). It is reported that the amino acids present in different foods are used as nutraceuticals for the treatment and prevention of diseases (Sharma *et al*., 2016). It is also known that amino acids are essential nutrients in the diet and supplements containing them can be beneficial in strict vegetarian people. Recent studies suggest that a supplementation of tryptophan could improve the therapeutic treatment of patients with anorexia nervosa (Haleem, 2017). Besides, the supplements containing essential amino acids together with keto acids is beneficial to ensure an adequate supply of essential amino acids in patients with chronic kidney disease (Cupisti and Bolasco, 2017).

Particularly, mandarins have eight of the nine essential amino acids (histidine, isoleucine, leucine, lysine, methionine, phenylalanine, threonine, tryptophan and valine), which makes their consumption beneficial to human health, but the content of free amino acids is different depending on the variety. The total content of amino acids in Satsuma mandarin has been reported as 15 µmol g^{-1}, being the most abundant ones asparagine (3.5 µmol g^{-1}), arginine (2.4 µmol g^{-1}), aspartic acid (2.0 µmol g^{-1}), proline (1.5 µmol g^{-1}) and glutamine (1.0 µmol g^{-1}). Meanwhile, the remaining amino acids are in concentrations lower than 1 µmol g^{-1}. Besides, in mandarin juices the most abundant amino acids are proline (1 mg mL^{-1}), arginine (0.85 mg mL^{-1}), asparagine (0.18–0.86 mg mL^{-1}), aspartic acid (0.24–0.50 mg mL^{-1}), glutamic acid (0.17–0.34 mg mL^{-1}), serine (0.12–0.26 mg mL^{-1}), alanine and phenylalanine (0.60–0.15 mg mL^{-1}). The total content of free amino acids changes during the maturity of the fruit, being proline and arginine those that showed the most substantial changes (Ladanyia, 2008). In citrus fruits,

free amino acids play an important role as osmoprotectants, but also their connection to disease resistance had been highlighted (Killiny and Hijaz, 2016; Sadka *et al*., 2019). Although amino acids are compounds which belong to the primary metabolism, their contribution to specific adaptive properties to stress places them as contributors to the role of secondary metabolism. Secondary metabolites are normally at concentration levels of one or two orders of magnitude lower than primary metabolites. Given the reported amounts of amino acids in citrus fruits, it could be of interest to study the changes they go through between two different cropping years, with distinct water availability during fruit development. To study these changes, coupling analytical determinations with statistical analyses is the most appropriate strategy (Dewick, 2009). Within this frame, the study of changes in the amino acids profile, using the concepts of targeted metabolomics was faced using liquid chromatography-tandem mass spectrometry. Up to date, there have not been studies using a targeted determination by ion exchange liquid chromatography-mass spectrometry (LC-(ESI)-MS/MS) of the occurrence of amino acids in mandarins produced in the region. These data allow the regional and national industries to characterize and differentiate their production from a nutraceutical point of view. With this idea in mind, the inter-cultivar composition variability of nine amino acids in cultivars Willowleaf, Page and Ellendale, as well as the variations between two consecutive harvests, is presented in this work.

2. Materials and methods

2.1 Samples

Mandarin samples were bred at Instituto Nacional de Investigación Agropecuaria (INIA) — Salto Grande (31°16'18" S 57°53'26" W) in two consecutive harvesting seasons during 2015 and 2016. Fruits were harvested at their optimal fruit ripening and stored at –20 °C until processed.

A total of 59 samples of mandarins of three different genetically stable cultivars: Willowleaf (*Citrus reticulata*), Page (*Tangelo minneola × Clementina*), Ellendale (*Citrus sinensis × Citrus reticulata*) were selected for this study. In the sampling process, 10 mandarins were taken from each tree randomly. At the time of harvest, the quality parameters of the fruit (titratable acidity, soluble solids, texture, internal and external color) were evaluated to ensure that the maturity between the varieties was the

same. In the case of 'Page' (2015), the samplings were carried out in May and July in order to evaluate the amino acids profile for the same variety at different maturity stages.

2.2 Reagents and materials

High purity amino acid standards were provided by Sigma-Aldrich. Individual standard solutions were prepared at a concentration of 1000 mg L^{-1}, using a mixture of 50:50 $CH_3OH:H_2O$ 0.1% formic acid (HCOOH) as solvents. Subsequently, a mix of 10 mg L^{-1} was prepared, containing all the purchased amino acids, making the corresponding dilutions from the different standard solutions. Ultra-pure water was used as solvent for the mobile phase and acidified water with 1 mmol L^{-1} citric acid (Analar-BDH Chemical Ltd Poole England) and finally adjusted to pH 11 with dimethylamine (DMA). Methanol (PHARMCO-AAPER) quality UV-HPLC and chloroform (J.T. Baker) quality HPLC were used as extraction solvents.

For the extraction procedure, 50 mL conical polypropylene tubes, 5 mL syringes and 0.45 μm hydrophobic PTFE filters were used. Vials of 12 and 4 mL to store the samples, and vials for automatic sampling of 2 mL with screw cap and septum for injection in the chromatographic equipment were used.

2.3 Apparatus and experimental conditions

The LC-(ESI)–MS/MS analysis was performed with an Agilent 1200 LC system (Agilent Technologies, Palo alto, CA, USA) coupled to a 4000 QTRAP LC-MS/MS system from AB SCIEX™ (Framingham, Massachusetts, USA) run in the Scheduled MS/MS-mode. The LC-Separation was performed on a Dionex AS11 (250 × 2 mm, 4 μm) ion exchange column. The column temperature was 40 ºC and it was reconstituted after de analysis with a solution of NaOH 30 mmol L^{-1}. The operation of the LC gradient involved the elution program described in Fig. 1, A: water; B: water 1 mmol L^{-1} citric acid and adjusted to pH 11. It was run at 300 μL min^{-1}. The injection volume was 5 μL. The MS/MS detection was performed with a QqQ analyzer in the multiple reaction monitoring (MRM) mode using an Electrospray Ionization (ESI) interface in the negative ion mode (Bringans et al., 2011). The ionization voltage was 5000 V, the nebulizer and the curtain gases were nitrogen at 50 psi each. The solvent evaporation in the source was assisted by a drying gas (heated nitrogen at 500 °C per 50 psi). The optimal

MRM transitions, collision energies (CE), cell exit potential (CXP) and declustering potentials (DP) for each investigated compound were determined infusing with a syringe directly the amino acids individual standard solutions to the instrument at a constant flow of 10 μL min^{-1}.
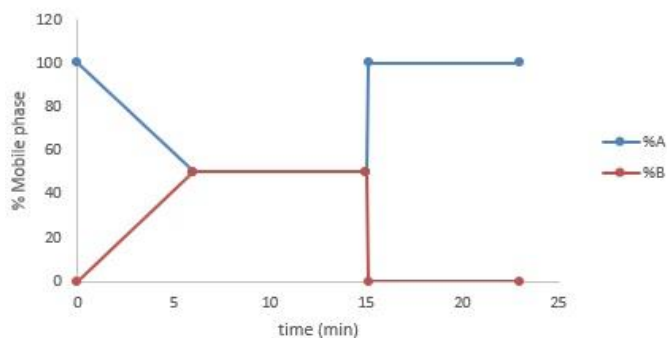

Figure 1. LC-MS/MS elution program.

2.4 Instrumental identification

The criteria used for identification of the targeted analytes using MRM acquisition mode, based in mass spectrometry pesticide residue analysis guidelines, were retention time of the analyte corresponding to that of the calibration standard (0.1 min of tolerance) and the precursor ion that yields product ions of specific m/z., called transitions. Additional confirmation was achieved evaluating the reference ion ratio. The reference ion ratio (m/z ratio) is the average obtained in solvent of standards measured in the same sequence and under the same conditions as the samples [Intensity(m/z)$_{transition}$/(intensity(m/z)$_{parent}$)]. The MRM transitions ratio from sample extracts should be within ± 30% (relative) of average of calibration standards tolerance deviation (EURL, 2017).

2.5 Amino acids extraction

The amino acids were extracted from mandarins pulp with a methodology adapted from Verpoorte et al. (2007). For the extraction of the amino acids, 2.0 ± 0.1 g of frozen crushed pulp were placed in a 50 mL polypropylene centrifuge tube together with 8 mL of $CHCl_3$ (LiChrosolv, Merck, Germany), 4 mL of MeOH (LiChrosolv, Merck, Germany), and 4 mL of ultrapure water (Millipore Milli-Q Ultrapure Water Solutions Type 1). The resulting suspension was vortexed for 30 s and sonicated for 60 s. It was then centrifuged for 5 min at 1400 xg, the phases were separated, and 8 mL of $CHCl_3$ were added to the aqueous phase. The whole

process was repeated, and the organic phases were combined and stored for future analysis. The aqueous extract was filtered, distilled under reduced pressure to remove MeOH, and then lyophilized to remove water (Migues *et al.*, 2021). Finally, the freeze-dried extract was dissolved in water and citric acid adjusted to pH 11 with DMA, filtered and placed in a 2 mL injection vial.

2.6 Study of linearity and limit of quantification (LOQ)

The LOQ and linearity were determined from the calibration curves performed in solvent for each analyte. To establish the linear range, curves that have a correlation coefficient greater than 0.99 and a good visual adjustment were considered acceptable. The LOQ was determined by the lowest level of concentration studied in which a signal-to-noise ratio greater than 10 was obtained and an adequate peak shape with correct superposition between transitions was observed.

2.7 Statistical analysis

For data treatment, the XLSTAT version 2015 software was used, as well as the principal component analysis (PCA) and Levene's test for homogeneity of variances.

A student's t test was applied to the results obtained for two samples, assuming equal variances with 95% confidence. This test assumes normal distribution and homogeneity of variances between the samples. For the samples that did not present homogeneous variances, a student's test was performed for two samples with unequal variances.

For the classification of mandarin varieties, to evaluate their diversity, and to identify outliers within each class, PCA was employed. For the identification of the most relevant amino acids between harvests, a discriminant analysis of partial least squares (PLS-DA) was performed using MetaboAnalyst software (version 4.0) (Chong *et al.*, 2018; Chong and Xia, 2018). Pareto scaling was applied to minimize the weight of large values while maintaining data structure partially intact (van den Berg *et al.*, 2006). The models derived from PLS-DA were validated using permutation tests of 100 iterations where the classes were randomly reassigned, two thirds of the data were used as training data to build a classifier, and the remaining third of the data was used to test it. The VIP scores study based on loadings from the PLS analysis show the amino acid that contribute to the separation and differentiation of the two harvests.

3. Results and discussion

The production of mandarins in Uruguay has a broad harvest calendar that covers from the end of February (mid-summer) to the end of October (mid-spring) according to the different varieties that are cultivated. These numerous varieties have been originated by spontaneous mutations of mandarins or by crossing with other citrus fruits, such as orange or grapefruit (Otero *et al.*, 2020). Differences in their amino acids profiles are expected due to their wide genetic variety and harvesting times during the year (Kefford and Chandler, 1970; Underwood and Rockland, 1953). The amino acids selected for the study, listed in Tab. 1, represent a combination of essential amino acids and those with relevant osmoprotective properties.

Table 1. Mass of the ions generated operating in ESI negative mode. Amino acid, precursor ion and product (m Z^{-1}), fragmentation potential (DP), collision energy (CE), input potential (EP), cell output potential (CXP) is from the mass analyzer operating in ESI mode negative.

Amino acid	Precursor ion (m Z^{-1})	Product ion (m Z^{-1})	DP (V)	EP (V)	CE (V)	CXP (V)
Asparagine	132.0	88.0	−10	−10	−16	−8
	132.0	115.0	−10	−10	−16	−10
	132.0	71.0	−10	−10	−18	−6
Glutamine	145.0	128.0	−10	−10	−12	−6
Methionine	148.0	47.0	−10	−10	−22	−6
Phenylalanine	164.0	147.0	−70	−10	−18	−25
	164.0	103.0	−70	−10	−24	−15
	164.0	72.0	−70	−10	−20	−11
						Continue…

Tyrosine	180.0	163.0	−80	−10	−20	−27
	180.0	119.0	−80	−10	−26	−19
Threonine	118.0	74.0	−55	−10	−16	−11
	118.0	72.0	−55	−10	−14	−11
Proline	114.0	68.0	−75	−10	−18	−9
	114.0	66.0	−75	−10	−20	−11
Histidine	154.0	109.0	−40	−10	−12	−17
	154.0	93.0	−40	−10	−26	−13
	154.0	137.0	−40	−10	−20	−21
Glutamic acid	146.0	102.9	−50	−10	−18	−15
	146.0	128.0	−50	−10	−18	−9

3.1 Targeted analysis

Taking into account that the level of the concentrations of free amino acids reported in mandarins are in the order of µg/kg, as well as the polarity of the moieties, the most suitable analytical approach for their analysis is liquid chromatography coupled to mass spectrometry. Due to the ionic behavior of these compounds, the use of the reverse phase in liquid chromatography (LC) is not the best selection for the analysis. The reported methods show that it is possible to analyze them directly, using an ion exchange column (Piraud *et al.*, 2003), polar columns (Yao *et al.*, 2013), or indirectly, using derivatization (Alterman and Hunziker, 2012). Particularly, in this work the analysis was performed using an ion exchange column, as it is described in section 2.3, to avoid the standardization of the derivative reaction and make the analysis simpler.

For the analysis it was necessary to optimize the chromatographic separation with an ion exchange column (Fig. 2), as well as the tandem mass detector conditions described above (Tab. 1).
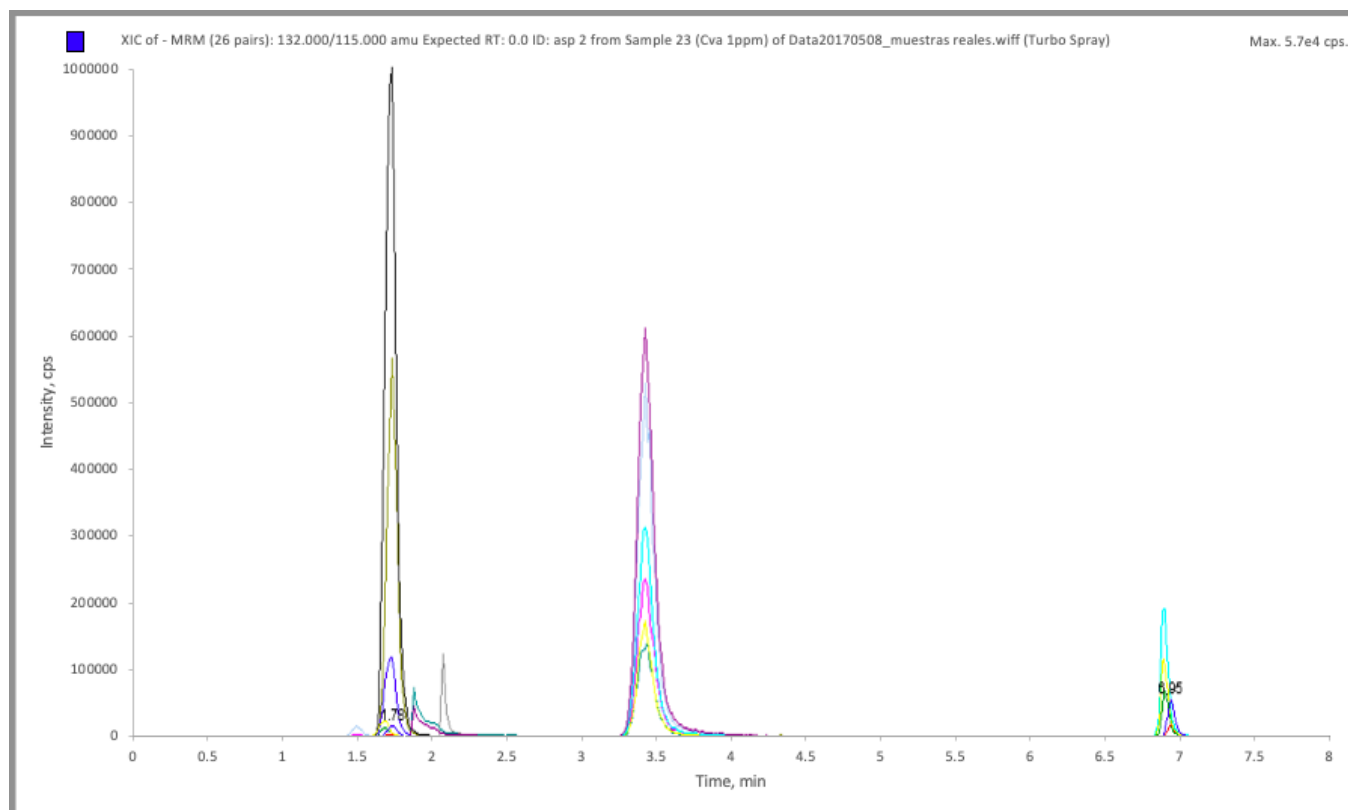

Figure 2. Multi reaction monitoring (MRM) chromatogram of the nine studied amino acids at a 1 mg L^{-1} level.

The final instrumental method was based on the MRM operation mode, which is a highly specific and sensitive mass spectrometry operation mode that can selectively quantify compounds in a complex matrix

(Bringans *et al.*, 2011; Wright *et al.*, 2015). Multiple reaction monitoring provides high selectivity to the determination, enhancing the signal to noise (S/N) ratio of the peaks, improving the overall sensitivity.

In summary, the triple quadrupole configuration allows to work in tandem mass spectrometry configuration. The first quadrupole acts as a filter for the [M-H]$^-$ ions generated in the ESI source, they are then guided to a second quadrupole which is a collision chamber. The [M-H]$^-$ ions (precursor ion) degrade to fragmented ions (product ions). The third quadrupole filters the product ions, eliminating the back noise that spoils the S/N relationship. The transitions from the precursor ion to the product ion are highly specific and are the basis for the high selectivity and sensibility of the MRM acquisition mode. In this work, precursor ions, declustering potential, product ions, cell exit potential and collision energies were determined by direct infusion of each analyte. It is important to notice that, for each precursor ion, different collision energies and cell exit potential are settled in order to enhance the production of each product ion and, as a consequence, a better S/N ratio will be obtained.

For MRM compounds optimization and MRM quantitative analysis, amino acids standards are necessary. Focused on the instrumental confirmation of the analytes, two transitions were monitored, and a time-scheduled acquisition method was developed. However, this criterion has not been accomplished for glutamine and methionine, it was only possible to optimize just one transition for each of these compounds.

3.2 Linearity and LOQ

The linearity was evaluated with calibration curves in solvent in a range between 5–1000 µg L^{-1}. For all the amino acids in study a linear adjustment was obtained with a correlation coefficient higher than 0.99 in a range that varies with the analyzed compound. The linear ranges for each compound were set from the LOQ value to 1000 µg L^{-1}.

The LOQs obtained were 10 µg L^{-1} for asparagine, methionine and threonine, 20 µg L^{-1} for phenylalanine and glutamic acid, 50 µg L^{-1} for histidine, 100 µg L^{-1} for glutamine, 250 µg L^{-1} for tyrosine and 500 µg L^{-1} for proline, respectively.

3.3 Sample analysis

A total of 59 mandarin samples were analyzed (33 belonging to the 2015 harvest and 26 to the 2016 harvest). The samples from 2015 were: 10 cultivar Ellendale, 13 cultivar Page and 10 cultivar Willowleaf. While the ones from 2016 were: 10 cultivar Ellendale, 9 cultivar Page and 7 cultivar Willowleaf.

To study the variability of the amino acids content during maturation of cultivar Page, a total of 23 samples collected in May and July of 2015 were tested.

The content of each amino acid (expressed as µg g^{-1} of dried extract) present in the different varieties in two years of production are presented in Tabs. 2 and 3. The amino acids were distributed in a wide range of concentration as it was reported by Ladanyia (2008). The amino acid with higher concentration was a different one in the three studied varieties. Ellendale presented proline, as the amino acid with higher concentration in both years of production studied, while 'Willowleaf' was characterized by the presence of asparagine and for cultivar Page the prevalent ones were proline and asparagine in both harvests, being the concentration level of glutamic acid remarkably close to the levels of the other two.

Table 2. Average, maximum and minimum concentrations of the nine amino acids for the three varieties year 2015.

Harvest 2015	'Willowleaf'			'Ellendale'			'Page'		
Concentration (µg g^{-1})	Average	Minimum	Maximum	Average	Minimum	Maximum	Average	Minimum	Maximum
Glutamic acid	266.0	240.0	500.0	163.0	89.0	305.0	577.1	358.9	1360.6
Asparagine	1215.7	40.0	4560.0	2021.4	811.0	3556.0	806.4	66.0	1369.0
Phenylalanine	26.2	16.0	35.0	196.1	89.0	254.0	46.0	12,0	92.0
Glutamine	665.8	18.0	2593.0	200.6	101.0	362.0	55.9	10.0	86.0
Histidine	< LOQ	< LOQ	< LOQ	33.8	26.0	61.0	< LOQ	< LOQ	< LOQ
Methionine	< LOQ	< LOQ	< LOQ	< LOQ	< LOQ	< LOQ	< LOQ	< LOQ	< LOQ
Proline	6.7	1.0	11.0	7431.0	330.6	11615.5	996.9	641.2	1440.2
Tyrosine	< LOQ	< LOQ	< LOQ	77.9	37.0	111.0	11.3	6.0	20.0
Threonine	15.8	7.0	35.0	84.8	45.0	114.0	16.2	9.0	38.0

Table 3. Average, maximum and minimum concentrations of the nine amino acids for the three varieties year 2016.

Harvest 2016	'Willowleaf'			'Ellendale'			'Page'		
Concentration (µg g⁻¹)	Average	Minimum	Maximum	Average	Minimum	Maximum	Average	Minimum	Maximum
Glutamic acid	348.1	51.0	963.0	280.0	195.0	346.0	1457.4	865.0	1969.3
Asparagine	5629.2	3148.0	8044.0	1377.1	517.0	2769.0	2255.5	1128.3	2985.2
Phenylalanine	60.1	39.0	76.0	130.0	81.0	264.0	83.6	69.4	99.4
Glutamine	340.9	114.0	570.0	231.7	66.0	689.0	148.5	103.0	231.0
Histidine	< LOQ	< LOQ	< LOQ	68.2	40.0	127.0	19.8	10.0	33.0
Methionine	2.0	1.0	3.0	< LOQ	< LOQ	< LOQ	< LOQ	< LOQ	< LOQ
Proline	18.6	13.0	24.0	4293.6	3055.0	5627.0	1601.1	634.0	3429.0
Tyrosine	< LOQ	< LOQ	< LOQ	< LOQ	< LOQ	< LOQ	43.0	24.0	96.0
Threonine	3.1	2.0	5.0	97.4	67.0	146.0	26.3	19.0	45.0

In general, asparagine showed a wide range of concentrations among all the varieties. Low concentration levels of threonine, methionine and tyrosine were observed in the three varieties. Moreover, low concentrations ranges were observed for these amino acids in both evaluated years.

For 'Willowleaf' it was only possible to identify but not to quantify histidine and tyrosine because they concentration levels were below the LOQs. Same scenario was seen for asparagine, glutamine, threonine and methionine in 'Ellendale'; and for 'Page', methionine was not detected in neither of the studied years of production.

These results are in line with previous literature reports which assigned the variability in the mandarins amino acids composition to their wide genetic variety and their harvest time during the year (Otero *et al.*, 2020; Underwood and Rockland, 1953).

3.4 Statistical analysis

A student's t-test was carried out to study if the amino acid profiles were the same in each variety in the harvest of 2015 and 2016. The results for 'Willowleaf' variety showed that the concentrations of the amino acids asparagine, phenylalanine and proline have significant differences, while glutamine, methionine and glutamic acid have no significant differences.

Cultivar Ellendale showed that glutamic acid, phenylalanine, histidine, tyrosine and proline presented significant differences between their concentrations.

For cultivar Page, it was observed that glutamic acid, asparagine, phenylalanine, glutamine, proline, tyrosine and threonine present significant differences, while histidine did not present significant differences.

The student's t-test was also carried out for 'Page' harvested in May and July 2015 to study the differences in the amino acid profiles due to ripening. The results show that there are no significant differences between the concentration levels of the amino acids: glutamic acid, asparagine, phenylalanine, tyrosine and threonine. However, significant differences were observed for glutamine, histidine and proline. The difference between the amino acids profiles can be explained by the influence of several factors, such as genetic, maturity, the position of the fruit in the tree, management of the plant, climatic conditions and field factors (Otero *et al.*, 2020; Underwood and Rockland, 1953). The differences in appearance and taste that distinguish the different types and varieties of citrus are fundamentally differences in chemical composition because of genetic factors (Underwood and Rockland, 1953).

After the evaluation of the amino acid profiles in each mandarin variety, a PCA was carried out to study the differentiation of these varieties due to their amino acids composition. The PCA was implemented separately for the 2015 and 2016 samples.

3.4.1 Principal component analysis (PCA) of 2015 samples

In the PCA carried out for the varieties harvested in 2015, a slight separation between samples was achieved. According to the concentration levels, cultivar Ellendale is characterized by the presence of threonine, histidine, proline, phenylalanine and tyrosine; the cultivar Page is distinguished by containing a high concentration of glutamic acid; while 'Willowleaf' mandarin is differentiated by its content of methionine and glutamine (Fig. 3).
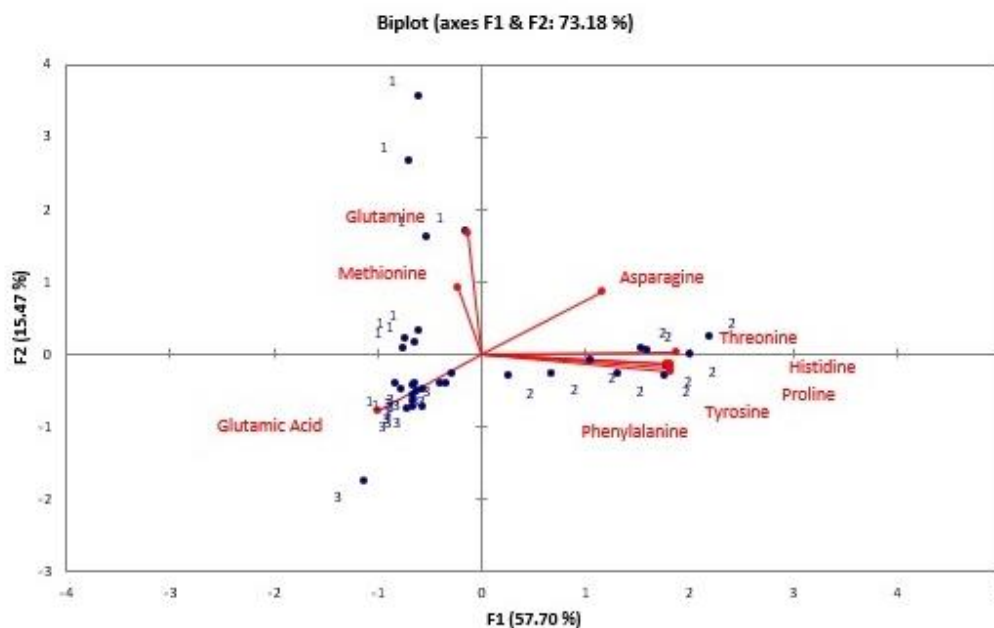
Figure 3. Principal component analysis of the three varieties of mandarin harvested in 2015 (1: 'Willowleaf'; 2: 'Ellendale'; 3: 'Page').

3.4.2 Principal component analysis of 'Page' May-July 2015 samples

Page variety harvests were carried out in two periods of the same year, in May and July 2015, being able in this way to compare the amino acid profiles of the fruit depending on the ripening grade (Tab. 4). Lin et al., (2015) reported that the concentration of free amino acids may increase or decrease depending on the maturity of the fruit. In this study, it was observed that some amino acids content increased (glutamic acid, asparagine and phenylalanine) upon maturity. The level of proline slightly decreased and a possible explanation for this result is the well-known increment in sugars concentration upon maturation, which will also increase the osmotic pressure within the juice sacs and, therefore, the contribution of proline as osmoprotectant is no longer needed (Torres et al., 2007). The results of the PCA (Fig. 4) showed a differentiation between mandarins at different harvest times, being those of July better represented by the amino acids histidine, asparagine, glutamine and glutamic acid.

Table 4. Average, maximum and minimum concentrations of the nine amino acids for the variety 'Page' May-July 2015.

| Harvest 2015	'Page' May			'Page' July		
Concentration (μg g^{-1})	Average	Minimum	Maximum	Average	Minimum	Maximum
Glutamic acid	589.7	178.0	976.5	1457.4	865.0	1969.3
Asparagine	2378.8	43.7	8378.3	2255.5	1128.3	2985.2
Phenylalanine	45.8	30.6	74.0	83.6	69.4	99.4
Glutamine	345.2	24.8	943.2	148.5	103.0	231.0
Histidine	126.6	5.8	260.4	19.8	10.0	33.0
Methionine	< LOQ	< LOQ	< LOQ	< LOQ	< LOQ	< LOQ
Proline	1803.6	947.8	2947.9	1601.1	634.0	3429.0
Tyrosine	14.7	3.7	20.3	43.0	24.0	96.0
Threonine	19.5	1.7	24.6	26.3	19.0	45.0
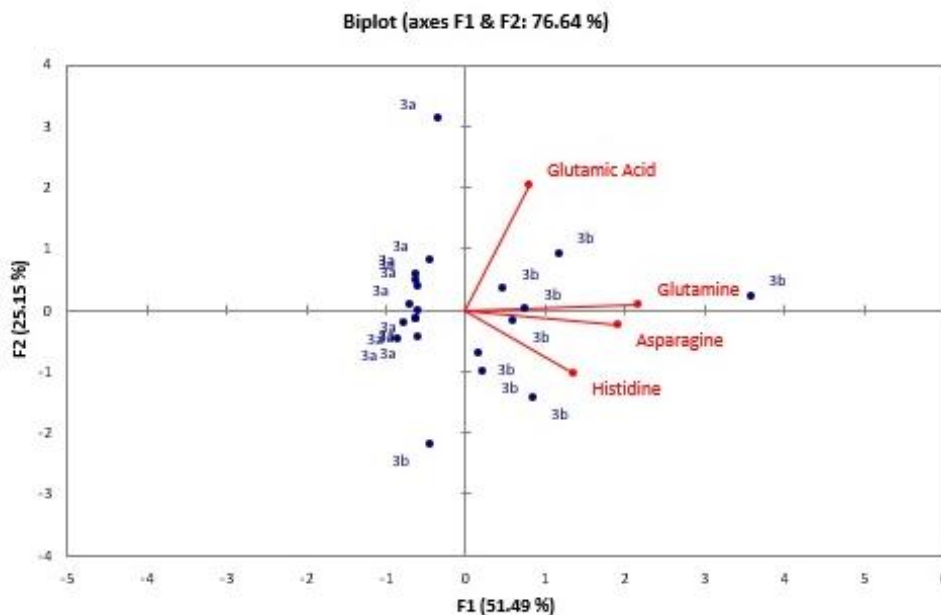
Figure 4. Principal component analysis of 'Page' variety with different degree of maturity (3a: May harvest; 3b: July harvest).

3.4.3 Principal component analysis of 2016 samples

For the varieties harvested in 2016, there is a clear differentiation between the samples of the three cultivars Ellendale, Page and Willowleaf. 'Ellendale' was characterized for its high concentration levels of glutamine, phenylalanine, histidine and threonine; whereas cultivar Page is represented by its high content of glutamic acid and tyrosine; and asparagine and methionine were the major amino acids for cultivar Willowleaf samples (Fig. 5).
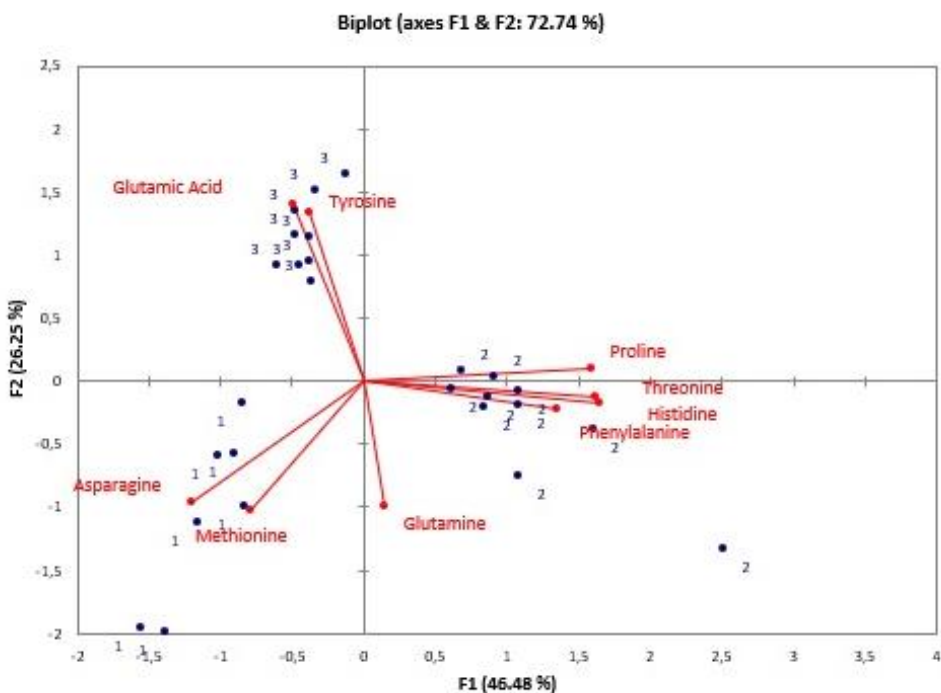
Figure 5. Principal component analysis of the three varieties of mandarin harvested in 2016 (1: 'Willowleaf'; 2: 'Ellendale'; 3: 'Page').

3.4.4 Discriminant analysis of partial least squares of the varieties harvested in 2015 and 2016

The comparison between Ellendale variety harvested in 2015 and 2016 indicate that the amino acid that weighted the most in the differentiation between both years is proline followed by asparagine (Fig. 6a). In Page variety, the most important amino acid for this classification was asparagine followed by glutamic acid and proline (Fig. 6b).
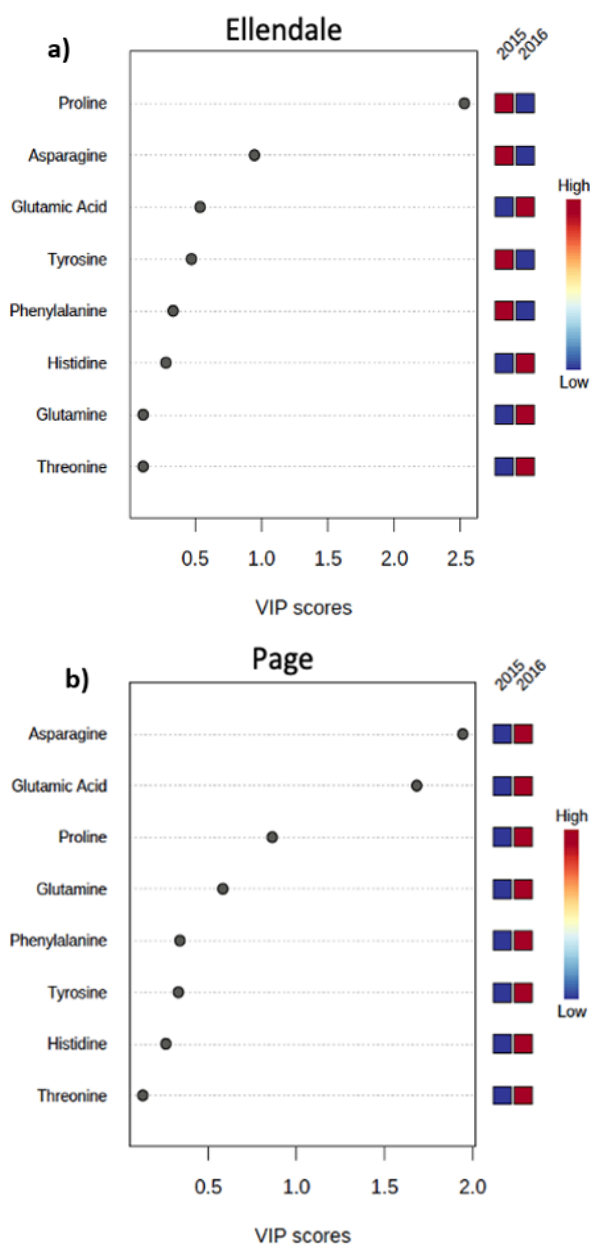
In the case of 'Willowleaf' (Fig. 7a), asparagine was the amino acid that showed greater changes between harvests followed by glutamic acid and proline, the same was as in cultivar Page. When this analysis was performed with all the three samples together (Fig. 7b), the results also indicate asparagine, glutamic acid and proline as the amino acids that suffered the most drastic change between one harvest and the other.
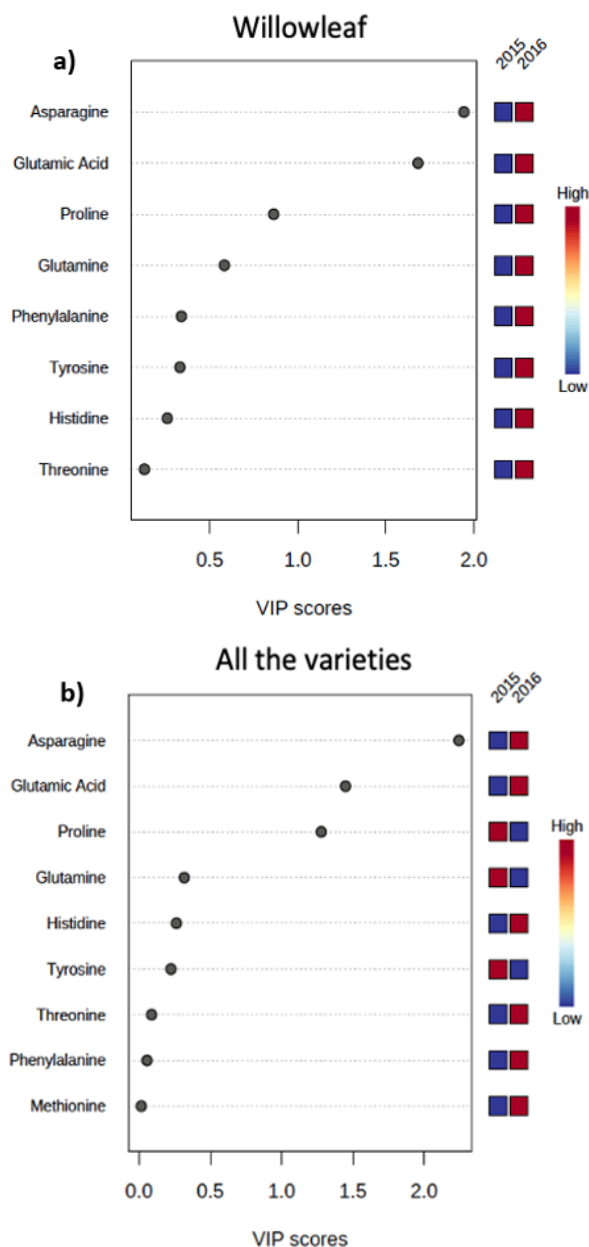

Figure 6. The VIP score plots of the PLS analysis performed on 'Ellendale' **(a)** and 'Page' **(b)** cultivated in 2015 and 2016.

Figure 7. The VIP score plots of the PLS analysis performed on 'Willowleaf' **(a)** and the three varieties together **(b)** cultivated in 2015 and 2016.

Even though the most abundant amino acid for each variety was the same between harvests (see section 3.2), this type of analysis allows to identify the most important concentration changes between one harvest and the other. These changes could also be attributed to environmental conditions during maturation process as 2016 was characterized by a larger precipitation range than 2015 specially during the first months of each year (INIA, 2017).

4. Conclusions

A sensitive methodology for the underivatized analysis of amino acids in mandarins was developed and applied to the extraction and determination of nine amino acids: asparagine, glutamic acid, glutamine, histidine, methionine, phenylalanine, proline, threonine and tyrosine.

Fifty-nine mandarin samples were analyzed, and the results showed the differences between the amino acid profiles which allow to differentiate the varieties. The most abundant amino acid of each variety was the same in both harvests, however, it was observed that there were significant differences in the concentrations of amino acids between the two years. These differences were also observed when comparing the evolution of the amino acid profiles of cultivar Page upon maturation. The increase in sugar concentration dropped down the proline levels. The results could be explained by the genetic differences between the varieties, as well as due to the environmental conditions. Osmoprotectants as proline showed lower levels in the rainy year 2016 (Zulfiqar *et al*., 2020).

The analysis of the main amino acids profile in different mandarin varieties using targeted MRM determination by LC-MS/MS proved to be a straightforward methodology to broaden marketing opportunities for the citrus industry, giving emphasis to the health-promoting effects of mandarins consumption due to their amino acids composition.

Authors' contribution

Data availability statement

The data will be available upon request.

Funding

Acknowledgments

References

Alterman, M. A.; Hunziker, P. *Amino Acid Analysis: Methods and Protocols*; Springer, 2012. https://doi.org/10.1007/978-1-61779-445-2

Bringans, S.; Stoll, T.; Winfield, K.; Casey, T.; Davis, T.; Albanese, J.; Lipscombe, R. Protein Biomarker Research Pipeline for Developing Protein Biomarkers for Diabetic Kidney Disease. *AB Sciex*, **2011**, 1–5. http://www.proteomics.com.au/wp-content/uploads/Biomarker-Pipeline-Diabetes-4250211-01.pdf (accessed 2020-06-10).

Cupisti, A.; Bolasco, P. Keto-analogues and essential aminoacids and other supplements in the conservative management of chronic kidney disease. *Panminerva Med.* **2017**, *59* (2), 149–156. https://doi.org/10.23736/S0031-0808.16.03288-2

Chong, J.; Soufan, O.; Li, C.; Caraus, I.; Li, S.; Bourque, G.; Wishart, D. S.; Xia, J. MetaboAnalyst 4.0: Towards more transparent and integrative metabolomics analysis. *Nucleic Acids Res.* **2018**, *46* (W1), W486–W494. https://doi.org/10.1093/nar/gky310

Chong, J.; Xia, J. MetaboAnalystR: An R package for flexible and reproducible analysis of metabolomics data. *Bioinformatics* **2018**, *34* (24), 4313–4314. https://doi.org/10.1093/bioinformatics/bty528

Dewick, P. M. *Medicinal Natural Products: A Biosynthetic Approach*; Wiley & Sons, 2009. https://doi.org/10.1002/9780470742761

EU Reference Laboratories for Residues of Pesticides (EURL). *Analytical quality control and method validation procedures for pesticide residues analysis in food and feed*; SANTE/2017/11813; European Commission: Brussels, 2017. https://www.eurl-pesticides.eu/userfiles/file/EurlALL/SANTE_11813_2017-fin.pdf (accessed 2020-06-11).

Fernández, E. L. *Alimentos funcionales y nutracéuticos*; Sociedad Española de Cardiología, 2007.

Haleem, D. J. Improving Therapeutics in Anorexia Nervosa with Tryptophan. *Life Sci.* **2017**, *178*, 87–93. https://doi.org/10.1016/j.lfs.2017.04.015

Instituto Nacional de Investigación Agropecuaria (INIA). Estación meteorológica. 2017. http://www.inia.uy/gras/Clima/Precipitación-nacional/Estación-meteorológica (accessed April 2017).

Kefford, J. F.; Chandler, B. V. *The Chemical Constituents of Citrus Fruits*; Academic Press, 1970.

Khan, M. K.; Zill-E-Huma; Dangles, O. A Comprehensive review on flavanones, the major citrus polyphenols. *J. Food Compost. Anal.* **2014**, *33* (1), 85–104. https://doi.org/10.1016/j.jfca.2013.11.004

Killiny, N.; Hijaz, F. Amino acids implicated in plant defense are higher in *Candidatus* liberibacter asiaticus-tolerant citrus varieties. *Plant Signal. Behav.* **2016**, *11* (4), e1171449. https://doi.org/10.1080/15592324.2016.1171449

Ladanyia, M. *Citrus Fruit: Biology, Technology and Evaluation*; Academic Press, 2008.

Lado, J.; Gambetta, G.; Zacarias, L. Key Determinants of Citrus Fruit Quality: Metabolites and Main Changes during Maturation. *Sci. Hortic.* **2018**, *233*, 238–248. https://doi.org/10.1016/j.scienta.2018.01.055

Lin, Q.; Wang, C.; Dong, W.; Jiang, Q.; Wang, D.; Li, S.; Chen, M.; Liu, C.; Sun, C.; Chen, K. Transcriptome and metabolome analyses of sugar and organic acid metabolism in Ponkan (*Citrus reticulata*) fruit during fruit maturation. *Gene* **2015**, *554* (1), 64–74. https://doi.org/10.1016/j.gene.2014.10.025

Migues, I.; Hodos, N.; Moltini, A. I.; Gámbaro, A.; Rivas, F.; Moyna, G.; Heinzen, H. ^{1}H NMR metabolic profiles as

selection tools of new mandarin cultivars based on fruit acceptability. *Sci. Hortic*. **2021**, 287, 110262. https://doi.org/10.1016/j.scienta.2021.110262

Otero, A.; Grasso, R.; Goñi, C.; Pérez, E.; Rubio, L.; Maeso, D.; Bertalmío, A.; Buenahora, J.; Giambiasi, M.; Arruabarrena, A.; Lado, J.; Moltini, A. I.; Fasiolo, C.; Espino, M.; Rivas, F. Desafíos de la citricultura en el uruguay y el aporte de inia a su competitividad. *Revista INIA* **2020**, *61*, 55–68.

Piraud, M.; Vianey-Saban, C.; Petritis, K.; Elfakir, C.; Steghens, J.-P.; Morla, A.; Bouchu, D. ESI-MS/MS analysis of underivatised amino acids: a new tool for the diagnosis of inherited disorders of amino acid metabolism. Fragmentation study of 79 molecules of biological interest in positive and negative ionisation mode. *Rapid Commun. Mass Spectrom.* **2003**, *17* (12), 1297–1311. https://doi.org/10.1002/rcm.1054

Sadka, A.; Shlizerman, L.; Kamara, I.; Blumwald, E. Primary Metabolism in Citrus Fruit as Affected by Its Unique Structure. *Front. Plant Sci.* **2019**, *10*, 1167. https://doi.org/10.3389/fpls.2019.01167

Sharma, V.; Singh, L.; Verma, N.; Kalra, G. The Nutraceutical Amino Acids: Nature's Fortification for Robust Health. *Br. J. Pharm. Res.* **2016**, *11* (3), 1–20. https://doi.org/10.9734/BJPR/2016/24415

Torres, G. A. M.; Gimenes, M. A.; Rosa Junior, V. E., Quecini, V. Identifying water stress-response mechanisms in citrus by in silico transcriptome analysis. *Genet. Mol. Biol.* **2007**, *30* (3 Suppl.), 888–905. https://doi.org/10.1590/S1415-47572007000500018

Underwood, J. C.; Rockland, L. B. Nitrogenous constituents in citrus fruits. *J. Food Sci.* **1953**, *18* (1–6), 17–29. https://doi.org/10.1111/j.1365-2621.1953.tb17681.x

van den Berg, R. A.; Hoefsloot, H. C. J.; Westerhuis, J. A.; Smilde, A. K.; van der Werf, M. J. Centering, scaling, and transformations: improving the biological information content of metabolomics data. *BMC Genomics* **2006**, *7*, 142. https://doi.org/10.1186/1471-2164-7-142

Verpoorte, R.; Choi, Y. H.; Kim, H. K. NMR-based metabolomics at work in phytochemistry. *Phytochem. Rev*. **2007**, *6*, 3–14. https://doi.org/10.1007/s11101-006-9031-3

Wright, M. J.; Thomas, R. L.; Stanford, P. E.; Horvath, A. R. Multiple Reaction Monitoring with Multistage Fragmentation (MRM3) Detection Enhances Selectivity for LC-MS/MS Analysis of Plasma Free Metanephrines. Clin. Chem. 2015, 61 (3), 505–513. https://doi.org/10.1373/clinchem.2014.233551

Xi, W.; Fang, B.; Zhao, Q.; Jiao, B.; Zhou, Z. Flavonoid composition and antioxidant activities of Chinese local pummelo (*Citrus Grandis* Osbeck.) varieties. *Food Chem.*

2014, *161*, 230–238. https://doi.org/10.1016/j.foodchem.2014.04.001

Yao, X.; Zhou, G.; Tang, Y.; Pang, H.; Qian, Y.; Guo, S.; Mo, X.; Zhu, S.; Su, S.; Qian, D.; Jin, C.; Qin, Y.; Duan, J.-a. Direct determination of underivatized amino acids from *Ginkgo biloba* leaves by using hydrophilic interaction ultra-high performance liquid chromatography coupled with triple quadrupole mass spectrometry. *J. Sep. Sci.* **2013**, *36* (17), 2878–2887. https://doi.org/10.1002/jssc.201201045

Zulfiqar, F.; Akram, N. A.; Ashra, M. Osmoprotection in plants under abiotic stresses: new insights into a classical phenomenon. *Planta* **2020**, *251*, 3. https://doi.org/10.1007/s00425-019-03293-1

Effect of the deformation parameter on the nonrelativistic energy spectra of the *q*-deformed Hulthen-quadratic exponential-type potential

Ushie Patrick Obogo[1] , Ofem Egbe Ubi[1] , Collins Okon Edet[2+] , Akpan Ndem Ikot[2]

1. Cross River University of Technology, Department of Physics, Faculty of Physical Sciences, Calabar, Nigeria.
2. University of Port Harcourt, Department of Physics, Rivers State, Nigeria.

+Corresponding author: Collins Okon Edet, **Phone:** +2349016715883, **Email address:** collinsokonedet@gmail.com

ABSTRACT: In this study, an approximate solution of the Schrödinger equation for the *q*-deformed Hulthen-quadratic exponential-type potential model within the framework of the Nikiforov–Uvarov method was obtained. The bound state energy equation and the corresponding eigenfunction was obtained. The energy spectrum is applied to study H_2, HCl, CO and LiH diatomic molecules. The effect of the deformation parameters and other potential parameters on the energy spectra of the system were graphically and numerically analyzed in detail. Special cases were considered when the

potential parameters were altered, resulting in deformed Hulthen potential, Hulthen potential, deformed quadratic exponential-type potential and quadratic exponential-type potential. The energy eigenvalues expressions agreed with what obtained in literature. Finally, the results can find many applications in quantum chemistry, atomic and molecular physics.
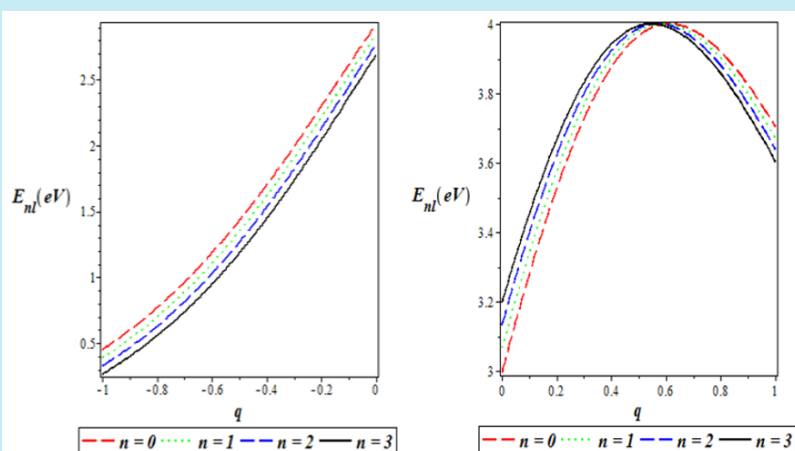
1. Introduction

Since the early days of quantum mechanics (QM), the study of a particle confined by a potential field has been of utmost importance (Edet and Okoi, 2019; Edet et al., 2020a; b; Landau, 1977; Schiff, 1995). Studies of this nature are carried out by solving the Schrödinger equation with different interaction potentials of interest. The solutions of the Schrödinger equation with different potential models of interest have been employed by many researchers to give insights, explanations, and predictions into the behavior of diatomic molecules, quarks, etc (Edet et al., 2020c; 2021a; Greiner, 2000; Okoi et al., 2020; Okorie et al., 2019).

Recently, numerous researchers have proffered solutions to the Schrödinger equation for some potential of interest. The analytical solution of the Schrödinger equation with $\ell = 0$ and $\ell \neq 0$ for some potentials has been addressed by many researchers in non-relativistic and relativistic quantum mechanics for bound states (Durmus and Yasuk, 2007; Edet et al., 2020d; 2021b; Louis et al., 2018a; 2018b). Some of these potentials include Deng-Fan potential (Falaye et al., 2015), Hyperbolic potential (Onate et al., 2018b), Eckart potential (Onate et al., 2017), generalized trigonometric Pöschl–Teller potential (Edet et al., 2020e), and screened Kratzer Potential (Ikot et al., 2020a).

Also, several methods have been employed to obtain the solutions of the nonrelativistic wave equations with some potential models of interest, some of these methods include: the factorization method (Dong, 2007), formula method (Falaye et al., 2015), supersymmetry quantum mechanics (SUSYQM) (Falaye et al., 2014), Nikiforov-Uvarov method (NU) (Nikiforov and Uvarov, 1988) asymptotic iteration method (AIM) (Ciftci et al., 2003; 2005; Falaye, 2012), exact quantization Rule (Gu and Dong, 2011; Ma and Xu, 2005), proper quantization rule (Qiang and Dong, 2007), WKBJ (Ita et al., 2018), etc.

Moreover, it is the goal in the present consideration to propose a potential of the form:

$$V_q(r) = \frac{V_0 e^{-\alpha r}}{1 - q e^{-\alpha r}} + \frac{V_1(a + b e^{-\alpha r} + c e^{-2\alpha r})}{(1 - q e^{-\alpha r})^2} \tag{1}$$

Where V_0 and V_1 are the potential strengths, α is the screening parameter, a, b and c are the adjusted parameter and q is deformation parameter. We call the potential q-deformed Hulthen-quadratic exponential-type potential (q-HQEP). With respect to what was obtained in previous studies of the molecular potential, the potential to allow for more physical application and a comparative analysis to existing studies of the molecular potential was modified. In addition, in molecular physics, it has also been established that potential energy functions with more parameters tend to fit experimental data than those with fewer parameters and researchers have recently paid great attention to obtaining modified version of potential functions by employing dissociation energy, and equilibrium bond length for molecular systems as explicit parameters. This model will be an important tool for spectroscopists to represent experimental data, verify measurements, and make predictions.

The potential is a superposition of the Hulthen (Ikhdair, 2009; Ikhdair and Sever, 2007; Onate et al., 2018a) and Quadratic exponential-type potentials (Okorie et al., 2018). These potentials have been individually applied to carry out studies extensively by several researchers (Ikot et al., 2014). Hence, the motivation to combine them.

In this research article, the goal is in two-fold. First, the Schrödinger wave equation (SWE) is solved with the q-HQEP via parametric Nikiforov–Uvarov method. The effect of the deformation parameter on the energy spectra of some diatomic molecules is analyzed with the aid of some graphical representation and numerical analysis.

The outline of the paper is as follows: section 2 provides brief a description of the parametric Nikiforov–Uvarov method. In section 3, the solutions of the three-dimensional (3D) Schrödinger equation (SE) with the q-HQEP via parametric NU. In Section 4, special cases of the potential understudy were discussed. In section 5, the results of this study are presented and discussed. Finally, in section 6, the concluding remarks are given.

2. The parametric NU method

The parametric form of the NU method takes the form (Tezcan and Sever, 2009):

$$\frac{d^2\psi}{ds^2} + \frac{\alpha_1 - \alpha_2 s}{s(1 - \alpha_3 s)} \frac{d\psi}{ds} + \frac{1}{s^2(1 - \alpha_3 s)^2}\{-\xi_1 s^2 + \xi_2 s - \xi_3\}\psi(s) = 0 \tag{2}$$

The energy eigenvalues equation and eigenfunctions satisfy the following sets of equations, respectively:

$$\alpha_2 n - (2n+1)\alpha_5 + (2n+1)(\sqrt{\alpha_9} + \alpha_3\sqrt{\alpha_8}) + n(n-1)\alpha_3 + \alpha_7 + 2\alpha_3\alpha_8 + 2\sqrt{\alpha_8\alpha_9} = 0 \tag{3}$$

$$\psi(s) = s^{\alpha_{12}}(1-\alpha_3 s)^{-\alpha_{12}-\frac{\alpha_{13}}{\alpha_3}} P_n^{(\alpha_{10}-1,\frac{\alpha_{11}}{\alpha_3}-\alpha_{10}-1)}(1-2\alpha_3 s) \tag{4}$$

where

$$\begin{aligned}
&\alpha_4 = \tfrac{1}{2}(1-\alpha_1), \alpha_5 = \tfrac{1}{2}(\alpha_2 - 2\alpha_3), \alpha_6 = \alpha_5^2 + \xi_1 \\
&\alpha_7 = 2\alpha_4\alpha_5 - \xi_2, \alpha_8 = \alpha_4^2 + \xi_3, \alpha_9 = \alpha_3\alpha_7 + \alpha_3^2\alpha_8 + \alpha_6 \\
&\alpha_{10} = \alpha_1 + 2\alpha_4 + 2\sqrt{\alpha_8}, \alpha_{11} = \alpha_2 - 2\alpha_5 + 2(\sqrt{\alpha_9} + \alpha_3\sqrt{\alpha_8}) \\
&\alpha_{12} = \alpha_4 + \sqrt{\alpha_8}, \alpha_{13} = \alpha_5 - (\sqrt{\alpha_9} + \alpha_3\sqrt{\alpha_8})
\end{aligned} \tag{5}$$

and P_n is the orthogonal Jacobi polynomial, which is defined as

$$P_n^{(\alpha,\beta)}(x) = \frac{\Gamma(\alpha+n+1)}{n!\Gamma(\alpha+\beta+n+1)}\sum_{m=0}^{n}\binom{n}{m}\frac{\Gamma(\alpha+\beta+n+m+1)}{\Gamma(\alpha+m+1)}\left(\frac{x-1}{2}\right)^m \tag{6}$$

3. Bound-state solutions of *q*-deformed Hulthen plus quadratic exponential-type potential

The radial Schrödinger equation in arbitrary dimensions (Rampho *et al*., 2021; Ebomwonyi *et al*., 2017) can be given as:

$$\frac{d^2R_{n\ell}(r)}{dr^2} + \frac{2\mu}{\hbar^2}\left[E_{n\ell} - V(r) - \frac{\ell(\ell+1)\hbar^2}{2\mu r^2}\right]R_{n\ell}(r) = 0 \tag{7}$$

where μ is the reduced mass, $E_{n\ell}$ is the energy spectrum, $\hbar$ is the reduced Planck's constant and n and ℓ are the principal and orbital angular momentum quantum numbers, respectively (or vibration-rotation quantum numbers in quantum chemistry) (Onate *et al*., 2018c). Substituting Eq. 1 into Eq. 7 gives:

$$\frac{d^2R_{n\ell}(r)}{dr^2} + \left[\frac{2\mu E_{n\ell}}{\hbar^2} - \frac{2\mu}{\hbar^2}\left(-\frac{V_0 e^{-\alpha r}}{1-qe^{-\alpha r}} + \frac{V_1(a+be^{-\alpha r}+ce^{-2\alpha r})}{(1-qe^{-\alpha r})^2}\right) - \frac{\ell(\ell+1)}{r^2}\right]R_{n\ell}(r) = 0 \tag{8}$$

The radial Schrödinger equation with this potential can be solved exactly for $\ell = 0$ (s-wave) but cannot be solved with this potential for $\ell \neq 0$. To obtain the solution for $\ell \neq 0$, the approximation scheme proposed by Greene and Aldrich (1976) is employed to deal with the centrifugal term, which is given as:

$$\frac{1}{r^2} \approx \frac{\alpha^2 e^{-\alpha r}}{(1-qe^{-\alpha r})^2} \tag{9}$$

It is noted that for a short-range potential, the relation in Eq. 9 is a good approximation to $\frac{1}{r^2}$, as proposed by Greene and Aldrich (1976), Ikot *et al*. (2020b) and Okorie *et al*. (2020). This implies that Eq. 9 is not a good approximation to the centrifugal barrier when the screening parameter α becomes large. Thus, the approximation is valid when $\alpha \ll 1$. Substituting the approximation Eq. 8 into Eq. 9, an equation of the form is obtained:

$$\frac{d^2R_{n\ell}(r)}{dr^2} + \left[\frac{2\mu E_{n\ell}}{\hbar^2} - \frac{2\mu}{\hbar^2}\left(\frac{V_0 e^{-\alpha r}}{1-qe^{-\alpha r}} + \frac{V_1(a+be^{-\alpha r}+ce^{-2\alpha r})}{(1-qe^{-\alpha r})^2}\right) - \frac{\ell(\ell+1)\alpha^2 e^{-2\alpha r}}{(1-qe^{-\alpha r})^2}\right]R_{n\ell}(r) = 0 \tag{10}$$

To solve the differential equation above, the transformation $s = e^{-\alpha r}$ is used so as to enable to apply the NU method as a solution technique to the hypergeometric-type differential equation. Hence, this transforms $\frac{d^2R_{n\ell}(r)}{dr^2}$ into the form:

$$\frac{d^2R_{n\ell}(r)}{dr^2} = \alpha^2 s^2 \frac{d^2R_{n\ell}(s)}{ds^2} + \alpha^2 s \frac{dR_{n\ell}(s)}{ds} \tag{11}$$

$$\alpha^2 s^2 \frac{d^2R_{n\ell}(s)}{ds^2} + \alpha^2 s \frac{dR_{n\ell}(s)}{ds} + \left[\begin{array}{c} \frac{2\mu E_{n\ell}}{\hbar^2} - \frac{2\mu}{\hbar^2} \left(\frac{V_0 s}{1-qs} + \frac{V_1(a+bs+cs^2)}{(1-qs)^2} \right) \\ - \frac{\ell(\ell+1)\alpha^2 s}{(1-qs)^2} \end{array} \right] R_{n\ell}(s) = 0 \tag{12}$$

In view of the above, the differential equation of the form is obtained:

$$\frac{d^2R_{n\ell}(s)}{ds^2} + \frac{1-qs}{s(1-qs)} \frac{dR_{n\ell}(s)}{ds} + \frac{1}{s^2(1-qs)^2} \left[\begin{array}{c} -(\varepsilon_{n\ell}q^2 + \beta q - \delta_3)s^2 + \\ (2\varepsilon_{n\ell}q + \beta - \delta_3 - \gamma)s - (\varepsilon_{n\ell} - \delta_3) \end{array} \right] R_{n\ell}(s) = 0 \tag{13}$$

where the following dimensionless abbreviations have been introduced for mathematical convenience:

$$-\varepsilon_{n\ell} = \frac{2\mu E_{n\ell}}{\hbar^2\alpha^2}, \beta = \frac{2\mu V_0}{\hbar^2\alpha^2}, \delta_1 = \frac{2\mu V_1 a}{\hbar^2\alpha^2}, \delta_2 = \frac{2\mu V_1 b}{\hbar^2\alpha^2}, \delta_3 = \frac{2\mu V_1 c}{\hbar^2\alpha^2} \gamma = \ell(\ell+1) \tag{14}$$

Equation 13 is of the form that is solvable by the NU method. Therefore, on comparison to Eqs. 2 and 13, the following parameters are obtained:

$$\begin{array}{l} \xi_1 = \varepsilon_{n\ell}q^2 + \beta q - \delta_3 \\ \xi_2 = 2\varepsilon_{n\ell}q + \beta - \delta_3 - \gamma \\ \xi_3 = \varepsilon_{n\ell} - \delta_3 \end{array} \tag{15a}$$

and

$$\begin{array}{l} \alpha_1 = 1, \alpha_2 = q, \alpha_3 = q \\ \xi_1 = \varepsilon_{n\ell}q^2 + \beta q - \delta_3, \xi_2 = 2\varepsilon_{n\ell}q + \beta - \delta_3 - \gamma, \xi_3 = \varepsilon_{n\ell} - \delta_3 \\ \alpha_4 = 0, \alpha_5 = -\frac{q}{2}, \alpha_6 = \frac{q^2}{4} + \varepsilon_{n\ell}q^2 + \beta q - \delta_3, \alpha_7 = -2\varepsilon_{n\ell}q - \beta + \delta_3 + \gamma \\ \alpha_8 = \varepsilon_{n\ell} + \delta_1, \alpha_9 = \frac{q^2}{4} - \delta_2 q + \gamma q + \delta_1 q^2 - \delta_3 \\ \alpha_{10} = 1 + 2\sqrt{\varepsilon_{n\ell} - \delta_1}, \alpha_{11} = 2q + 2\left(\sqrt{\frac{q^2}{4} - \delta_2 q + \gamma q + \delta_1 q^2 - \delta_3} + q\sqrt{\varepsilon_{n\ell} + \delta_1} \right) \\ \alpha_{12} = \sqrt{\varepsilon_{n\ell} + \delta_1}, \alpha_{13} = -\frac{q}{2} - \left(\sqrt{\frac{q^2}{4} - \delta_2 q + \gamma q + \delta_1 q^2 - \delta_3} + q\sqrt{\varepsilon_{n\ell} + \delta_1} \right) \end{array} \tag{15b}$$

Substituting these polynomials into Eq. 3, it is possible to obtain

$$q\left(n+\frac{1}{2}\right)^2 + 2\left(n+\frac{1}{2}\right)\left(\sqrt{\frac{q^2}{4} - \delta_2 q + \gamma q + \delta_1 q^2 - \delta_3} + q\sqrt{\varepsilon_{n\ell} + \delta_1} \right) - \beta + \delta_2 + \gamma + 2\delta_1 q + \frac{q}{4} + $$
$$2\sqrt{(\varepsilon_{n\ell} + \delta_1)\left(\frac{q^2}{4} - \delta_2 q + \gamma q + \delta_1 q^2 - \delta_3 \right)} = 0 \tag{16}$$

By carrying out some algebraic manipulation, the following equation is obtained:

$$\varepsilon_{n\ell} = -\delta_1 + \frac{1}{4}\left[\frac{\left(n+\frac{1}{2}+\sqrt{\frac{1}{4}-\frac{\delta_2}{q}+\frac{\gamma}{q}+\delta_1-\frac{\delta_3}{q^2}}\right)^2 + \frac{\delta_3}{q^2}+\delta_1-\frac{\beta}{q}}{\left(n+\frac{1}{2}+\sqrt{\frac{1}{4}-\frac{\delta_2}{q}+\frac{\gamma}{q}+\delta_1-\frac{\delta_3}{q^2}}\right)} \right]^2 \tag{17}$$

Substituting Eq. 14 into Eq. 17 and carrying some simple manipulative algebra, it is possible to arrive at the energy eigenvalue equation of the q-deformed Hulthen plus quadratic exponential-type potential in the form:

$$E_{n\ell} = V_1 a - \frac{\hbar^2 \alpha^2}{8\mu} \left[\frac{\left(n+\frac{1}{2}+\sqrt{\frac{1}{4}-\frac{2\mu V_1 b}{\hbar^2 \alpha^2 q}+\frac{\ell(\ell+1)}{q}+\frac{2\mu V_1 a}{\hbar^2 \alpha^2}-\frac{2\mu V_1 c}{\hbar^2 \alpha^2 q^2}}\right)^2 + }{\frac{2\mu V_1 c}{\hbar^2 \alpha^2 q^2}+\frac{2\mu V_1 a}{\hbar^2 \alpha^2}-\frac{2\mu V_0}{\hbar^2 \alpha^2 q}} \right]^2 \tag{18}$$

$$\frac{\frac{2\mu V_1 c}{\hbar^2 \alpha^2 q^2}+\frac{2\mu V_1 a}{\hbar^2 \alpha^2}-\frac{2\mu V_0}{\hbar^2 \alpha^2 q}}{\left(n+\frac{1}{2}+\sqrt{\frac{1}{4}-\frac{2\mu V_1 b}{\hbar^2 \alpha^2 q}+\frac{\ell(\ell+1)}{q}+\frac{2\mu V_1 a}{\hbar^2 \alpha^2}-\frac{2\mu V_1 c}{\hbar^2 \alpha^2 q^2}}\right)}$$

The corresponding wave functions can be evaluated from Eq. 4 as follows:

$$R_{n\ell}(s) = N_{n\ell} s^{\sqrt{\varepsilon_{n\ell}+\delta_1}}(1-s)^{\frac{1}{2}+\sqrt{\frac{1}{4}-\frac{\delta_2}{q}+\frac{\gamma}{q}+\delta_1-\frac{\delta_3}{q^2}}} P_n^{\left(2\sqrt{\varepsilon_{n\ell}+\delta_1},2\sqrt{\frac{1}{4}-\frac{\delta_2}{q}+\frac{\gamma}{q}+\delta_1-\frac{\delta_3}{q^2}}\right)}(1-2s) \tag{19}$$

From the definition of the Jacobi polynomials (Edet *et al*., 2020a; b).

$$P_n^{(2\varpi,2\chi)}(1-2s) = \frac{\Gamma(n+2\varpi+1)}{n!\Gamma(2\varpi+1)} \,_2F_1(-n,2\varpi+2\chi+n+1,2\varpi+1;s) \tag{20}$$

$$\varpi = \sqrt{\varepsilon_{n\ell}+\delta_1}$$

$$\chi = \sqrt{\frac{1}{4}-\frac{\delta_2}{q}+\frac{\gamma}{q}+\delta_1-\frac{\delta_3}{q^2}} \tag{21}$$

In terms of hypergeometric polynomials, Eq. 21 can be written as

$$R_{n\ell}(s) = N_{n\ell} s^{\varpi}(1-s)^{\frac{1}{2}+\chi} \frac{\Gamma(n+2\varpi+1)}{n!\Gamma(2\varpi+1)} \,_2F_1(-n,2\varpi+2\chi+n+1,2\varpi+1;s) \tag{22}$$

4. Special cases

4.1 Deformed Hulthen potential

If V_1 is set as $V_1 = a = b = c = 0$, the potential model (1) reduces to deformed Hulthen potential (Hall *et al*., 2018):

$$V_q(r) = \frac{V_0 e^{-\alpha r}}{1-qe^{-\alpha r}} \tag{23}$$

and the energy equation as follows:

$$E_{n\ell} = -\frac{\hbar^2 \alpha^2}{8\mu} \left[\frac{\left(n+\frac{1}{2}+\sqrt{\frac{1}{4}+\frac{\ell(\ell+1)}{q}}\right)^2 - \frac{2\mu V_0}{\hbar^2 \alpha^2 q}}{\left(n+\frac{1}{2}+\sqrt{\frac{1}{4}+\frac{\ell(\ell+1)}{q}}\right)} \right]^2 \tag{24}$$

This is in agreement with Eq. 44 (Edet and Okoi, 2019).

4.2 Hulthen potential

If V_1 is set as $V_1 = a = b = c = 0$ and $q \to 1$, the potential model (1) reduces to the Hulthen potential:

$$V(r) = \frac{V_0 e^{-\alpha r}}{1-e^{-\alpha r}},\qquad(25)$$

and the energy equation as follows:

$$E_{n\ell} = -\frac{\hbar^2 \alpha^2}{8\mu}\left[\frac{\left(n+\frac{1}{2}+\sqrt{\frac{1}{4}+\ell(\ell+1)}\right)^2 - \frac{2\mu V_0}{\hbar^2 \alpha^2}}{\left(n+\frac{1}{2}+\sqrt{\frac{1}{4}+\ell(\ell+1)}\right)}\right]^2 \qquad(26)$$

Equation 26 is in agreement with the energy equation given in Eq. 39 (Ikhdair, 2009), Eq. 31 (Ikhdair and Sever, 2007), Eq. 34 (Agboola, 2009), Eq. 35 (Bayrak *et al*., 2006) and Eq. 27 (Jia *et al*., 2008).

4.3 Deformed quadratic exponential-type potential

If V_0 is set as $V_0 = 0$, the potential model (1) reduces to deformed quadratic exponential-type potential:

$$V_q(r) = \frac{V_1(a+be^{-\alpha r}+ce^{-2\alpha r})}{(1-qe^{-\alpha r})^2}\qquad(27)$$

and the energy equation as follows:

$$E_{n\ell} = V_1 a - \frac{\hbar^2 \alpha^2}{8\mu}\left[\frac{\left(n+\frac{1}{2}+\sqrt{\frac{1}{4}-\frac{2\mu V_1 b}{\hbar^2 \alpha^2 q}+\frac{\ell(\ell+1)}{q}+\frac{2\mu V_1 a}{\hbar^2 \alpha^2}-\frac{2\mu V_1 c}{\hbar^2 \alpha^2 q^2}}\right)^2 + \frac{2\mu V_1 c}{\hbar^2 \alpha^2 q^2}+\frac{2\mu V_1 a}{\hbar^2 \alpha^2}}{\left(n+\frac{1}{2}+\sqrt{\frac{1}{4}-\frac{2\mu V_1 b}{\hbar^2 \alpha^2 q}+\frac{\ell(\ell+1)}{q}+\frac{2\mu V_1 a}{\hbar^2 \alpha^2}-\frac{2\mu V_1 c}{\hbar^2 \alpha^2 q^2}}\right)}\right]^2 \qquad(28)$$

4.4 Quadratic exponential-type potential

If V_0 is set as $V_0 = 0$ and $q \to 1$ the potential model (1) reduces to quadratic exponential-type potential (Okorie *et al*., 2018):

$$V(r) = \frac{V_1(a+be^{-\alpha r}+ce^{-2\alpha r})}{(1-e^{-\alpha r})^2}\qquad(29)$$

and the energy equation as follows:

$$E_{n\ell} = V_1 a - \frac{\hbar^2 \alpha^2}{8\mu}\left[\frac{\left(n+\frac{1}{2}+\sqrt{\frac{1}{4}-\frac{2\mu V_1 b}{\hbar^2 \alpha^2}+\ell(\ell+1)+\frac{2\mu V_1 a}{\hbar^2 \alpha^2}-\frac{2\mu V_1 c}{\hbar^2 \alpha^2}}\right)^2 + \frac{2\mu V_1 c}{\hbar^2 \alpha^2}+\frac{2\mu V_1 a}{\hbar^2 \alpha^2}}{\left(n+\frac{1}{2}+\sqrt{\frac{1}{4}-\frac{2\mu V_1 b}{\hbar^2 \alpha^2}+\ell(\ell+1)+\frac{2\mu V_1 a}{\hbar^2 \alpha^2}-\frac{2\mu V_1 c}{\hbar^2 \alpha^2}}\right)}\right]^2 \qquad(30)$$

Equation 30 is in agreement with the energy equation given in Eq. 31 (Okorie *et al*., 2018).

5. Results and discussions

In our study, the energy (Eq. 18) and wave function (Eq. 22) of the deformed Hulthen potential plus the quadratic exponential-type potential obtained using the parametric NU. For validity purposes, were also obtained the energy eigenvalues and wave function of the deformed Hulthen potential, Hulthen potential, deformed quadratic exponential-type potential and quadratic exponential-type potential, shown in Eqs. 23–30 as special cases.

In the present study, the energy spectrum was used to study the four selected diatomic molecules, H$_2$, HCl, CO and LiH. The spectroscopic parameters of these molecules are given in Tab. 1 and taken from (Edet *et al.*, 2020e; Rampho *et al.*, 2021). The following conversions were used; $\hbar c = 1973.269 \text{ eV\AA}$ and $1 amu = 931.5 \times 10^6 eV(\text{\AA})^{-1}$ for all computations (Edet *et al.*, 2020e; Rampho *et al.*, 2021). All non-spectroscopic parameters are kept in natural units.

Table 1. Spectroscopic parameters of the molecules used in this work (Edet *et al.*, 2020e; Rampho *et al.*, 2021).

Parameters	H$_2$ (Edet *et al.*, 2020e)	HCl (Rampho *et al.*, 2021)	CO (Edet *et al.*, 2020e)	LiH (Rampho *et al.*, 2021)
α (Å^{-1})	1.9426	1.8677	2.294	1.128
μ (a.m.u)	0.50391	0.980105	6.860672	0.880122

In Tab. 2, the energy values for the *q*-deformed Hulthen-quadratic exponential-type potential was shown for H$_2$, HCl, CO and LiH diatomic molecules for various values of the deformation parameter and of quantum states. It is seen clearly that when the deformation parameter is q = −0.5, the energy is low

and for instance in LiH molecule it becomes more bounded. But for q = 0.5, the energy is raised significantly although drops slightly and remains positive when q = 1 (i.e., absence of deformation).

Table 2. Energy values for the *q*-deformed Hulthen-quadratic exponential-type potential for H$_2$, HCl, CO and LiH diatomic molecule for various values of the deformation parameter and of quantum states.

State	q	H$_2$	HCl	CO	LiH
1s	−0.5	1.208540	1.104410	2.021420	−0.338560
	0.5	3.865880	3.710050	4.565230	2.225200
	1.0	3.547310	3.415690	4.299980	1.950540
2s	−0.5	0.910264	0.901356	1.928360	−0.466642
	0.5	3.885060	3.730360	4.578700	2.241860
	1.0	3.423210	3.333520	4.263660	1.899950
2p	−0.5	1.221470	1.110510	2.022730	−0.336094
	0.5	3.867670	3.711040	4.565480	2.225650
	1.0	3.542160	3.413300	4.299470	1.949580
3s	−0.5	0.600211	0.692631	1.834060	−0.597053
	0.5	3.872680	3.735150	4.588670	2.252040
	1.0	3.284190	3.243990	4.225680	1.846270
3p	−0.5	0.923715	0.907634	1.929690	−0.464130
	0.5	3.885170	3.730790	4.578890	2.242160
	1.0	3.417380	3.330900	4.263140	1.898930
3d	−0.5	1.247280	1.122710	2.025350	−0.331163
	0.5	3.870960	3.712950	4.565970	2.226530
	1.0	3.531790	3.408500	4.298470	1.947680
4s	−0.5	0.278707	0.478346	1.738530	−0.729764
	0.5	3.830940	3.725190	4.595210	2.255940
	1.0	3.131300	3.147490	4.186070	1.789610
4p	−0.5	0.614176	0.699079	1.835410	−0.594496
	0.5	3.871240	3.735050	4.588800	2.252200
	1.0	3.277720	3.241150	4.225130	1.845200
					Continue…

	−0.5	0.950587	0.920182	1.932350	−0.459108
4d	0.5	3.885150	3.731590	4.579270	2.242750
	1.0	3.405660	3.325650	4.262080	1.896900
	−0.5	1.285910	1.140990	2.029280	−0.323769
4f	0.5	3.875230	3.715670	4.566710	2.227830
	1.0	3.516090	3.401270	4.296950	1.944810

The variation of the energy eigenvalues with different parameters of the combined potential, such as V_0, V_1, a, b, c and q, is shown in Figs. 1–7, respectively, for H$_2$, HCl, CO and LiH diatomic molecule in the ground state. In Fig. 1a and b, the variation of the energy spectrum was plotted for various values of n as a function of the parameter ℓ for q = 1 and q = −1, respectively. Figure 1a shows that the energy decreases as the angular momentum increases. In Fig. 1b, it is possible to observe that the energy increases as the ℓ increases up to a maximum and then drops again sporadically. Figure 2a and b shows the variation of the energy spectrum for various values of n as a function of the parameter V_0 for q = 1 and q = 1, respectively, in the region $0 < V_0 < 3$. In Fig. 2a, the energy of the system increases as the parameter V_0 increases. In Fig. 2b, the energy linearly decreases as V_0 increases. Figure 3a and b shows the variation of the energy spectrum for various values of n as a function of the parameter V_1 for q = 1 and q = −1, respectively, in the region $0 < V_1 < 0.16$. In both figures, the energy increases monotonically as the parameter V_1 increases as well. Figure 4a and b shows the variation of the energy spectrum for various values of diatomic molecules as a function of the parameter a, respectively, in the interval $0 < a < 0.25$. In both cases considered, the energy increases linearly with increasing a, but in the case q = −1 (Fig. 4b), there is a wider spacing between the energy levels. Figure 5a and b shows the variation of the energy spectrum for various values of n as a function of the parameter b for q = 1 and q = −1, respectively, in the region $0 < b < 1$. In Fig. 5a, the energy increases linearly as the parameter b increases. In Fig. 5b, the energy decreases linearly as the parameter b increases. Figure 6a and b shows the variation of the energy spectrum for various values of n as a function of the parameter c for q = 1 and q = -1, respectively, in the region $0 < c < 0.20$. In Fig. 6a, the energy decreases linearly as the parameter c increases. In Fig. 6b, the energy decreases linearly as the parameter c increases. Figure 7a and b shows the variation of the energy spectrum for various values of n as a function of the parameter $−q$ and $+q$ in the intervals $−1 < q < 0$ and $0 < q < 1$, respectively. In Fig. 7a, the energy increases up to a maximum as q increases and then declines again. In Fig. 7b, the energy increases linearly as q upsurges.
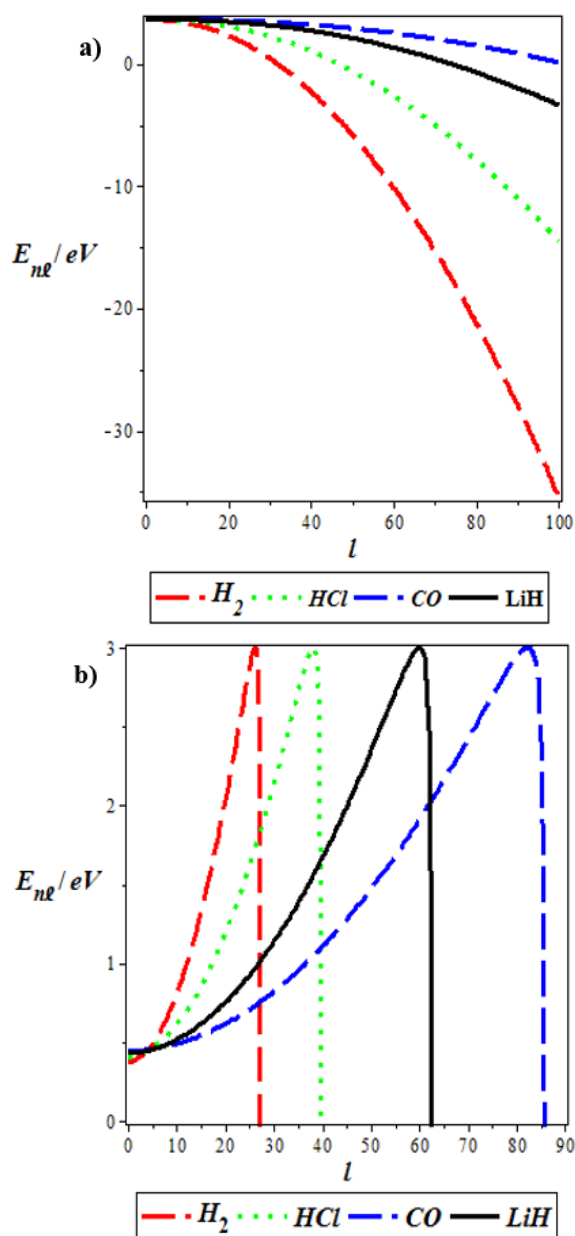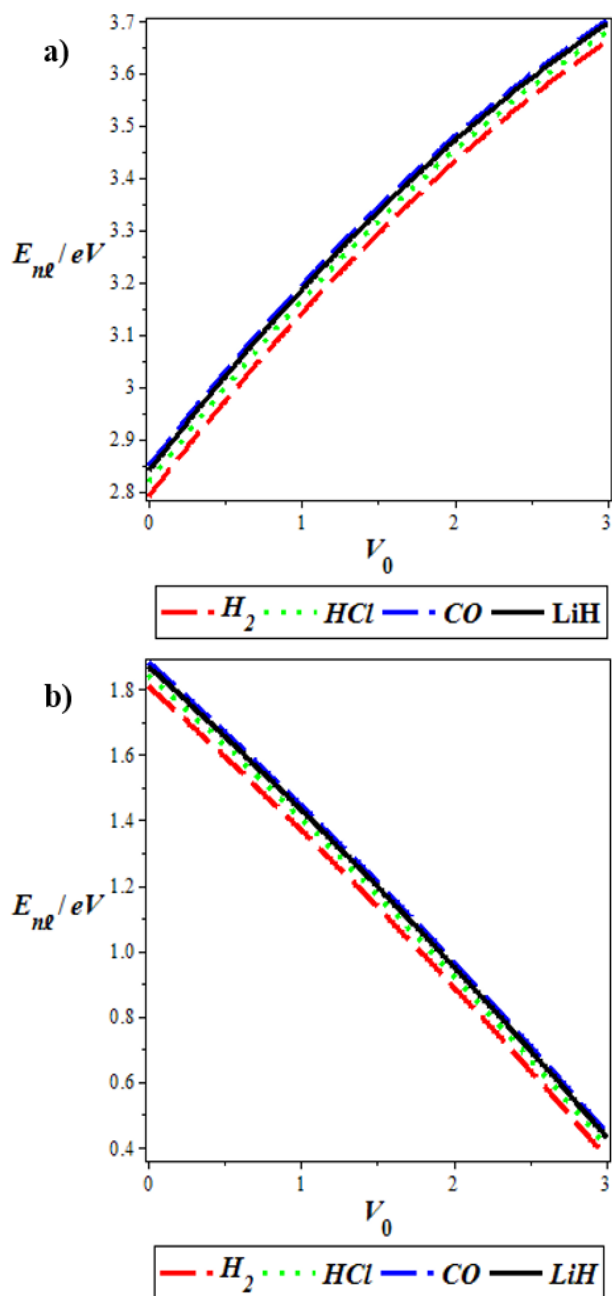

Figure 1. (a) The variation of the energy spectrum for various values of n as a function of the parameter ℓ for q = 1. (b) The variation of the energy spectrum for various values of n as a function of the parameter ℓ for q = −1. $a = 2\,fm^{-1}$, $b = 1\,fm^{-1}$, $c = −3\,fm^{-1}$, $V_1 = 2\,fm^{-1}$ and $V_0 = 3\,fm^{-1}$.
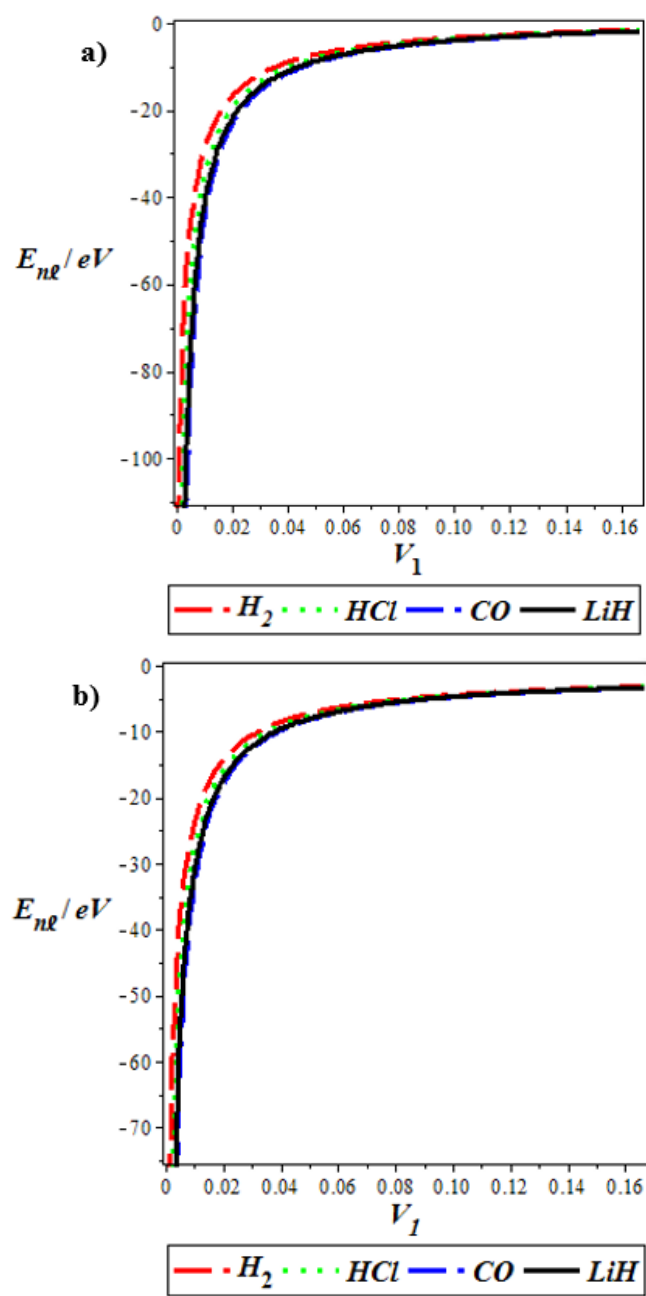
67

Figure 2. (a) The variation of the energy spectrum for various values of n as a function of the parameter V_0 for q = 1. **(b)** The variation of the energy spectrum for various values of n as a function of the parameter V_0 for q = −1. h = 1, μ = 1, a = 2, b = 1, c = −3, V_1 = 2 and α = 0.05.

Figure 3. (a) The variation of the energy spectrum for various values of n as a function of the parameter V_1 for q = 1. **(b)** The variation of the energy spectrum for various values of n as a function of the parameter V_1 for q = −1. a = 2, b = 1, c = −3 and V_0 = 3.
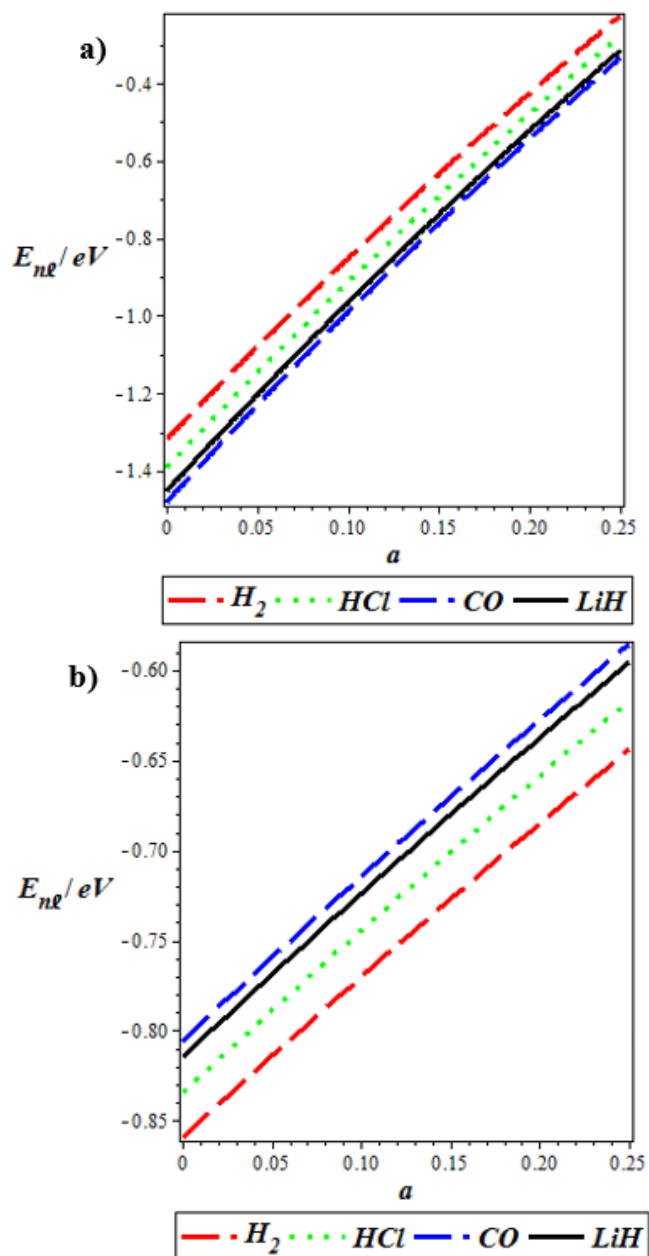
Figure 4. (a) The variation of the energy spectrum for various values of *n* as a function of the parameter *a* for q = 1. **(b)** The variation of the energy spectrum for various values of *n* as a function of the parameter *a* for q = −1. b = 1, c = −3, V_0 = 3 and V_1 = 2.
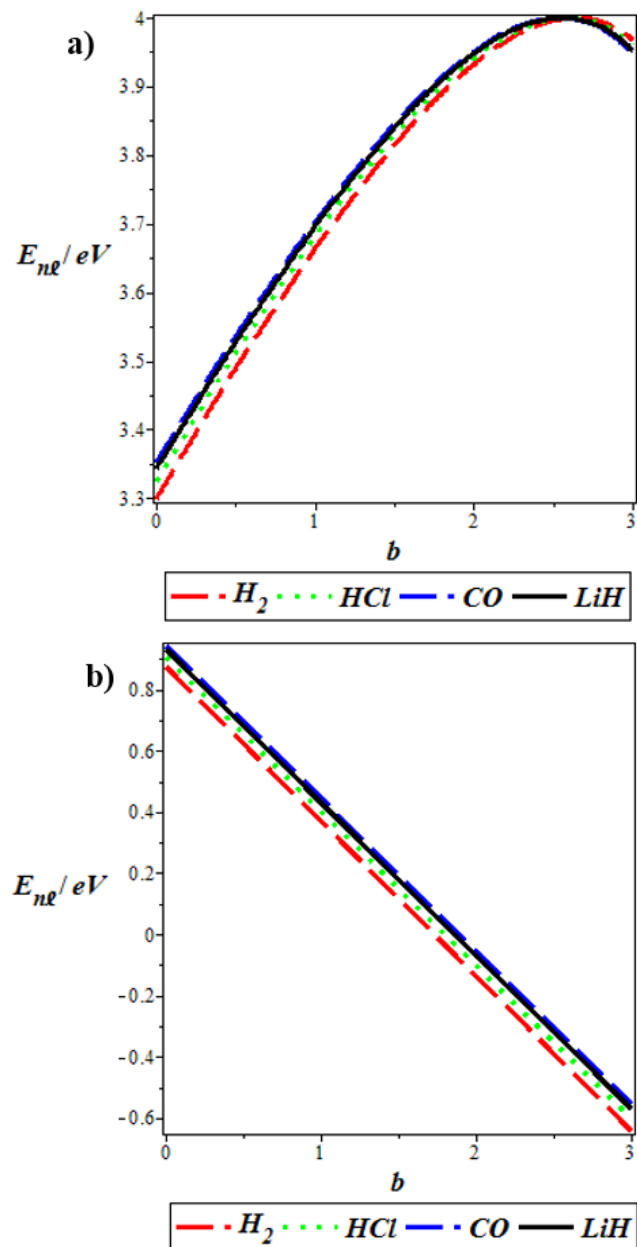
Figure 5. (a) The variation of the energy spectrum for various values of *n* as a function of the parameter *b* for q = 1. **(b)** The variation of the energy spectrum for various values of *n* as a function of the parameter *b* for q = −1. a = 2, c = −3, V_0 = 3 and V_1 = 2.

Figure 6. (a) The variation of the energy spectrum for various values of n as a function of the parameter c for $q = 1$. **(b)** The variation of the energy spectrum for various values of n as a function of the parameter c for $q = -1$. $a = 2$, $b = 1$, $V_0 = 3$ and $V_1 = 2$.
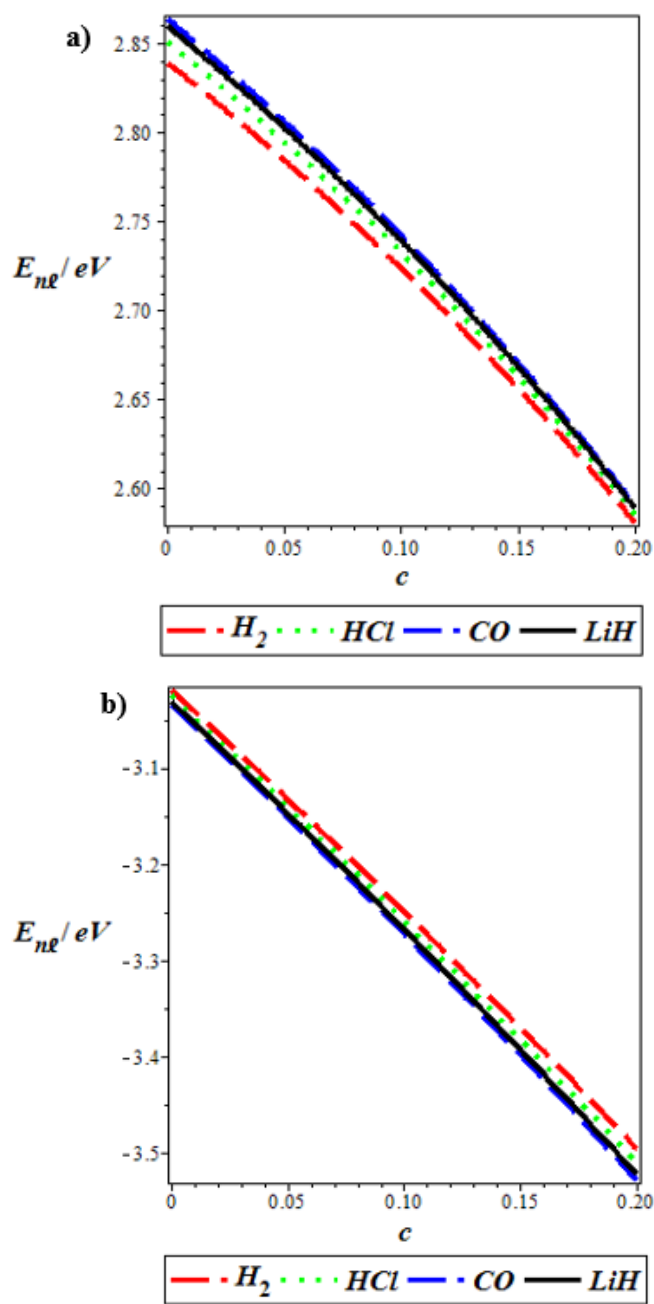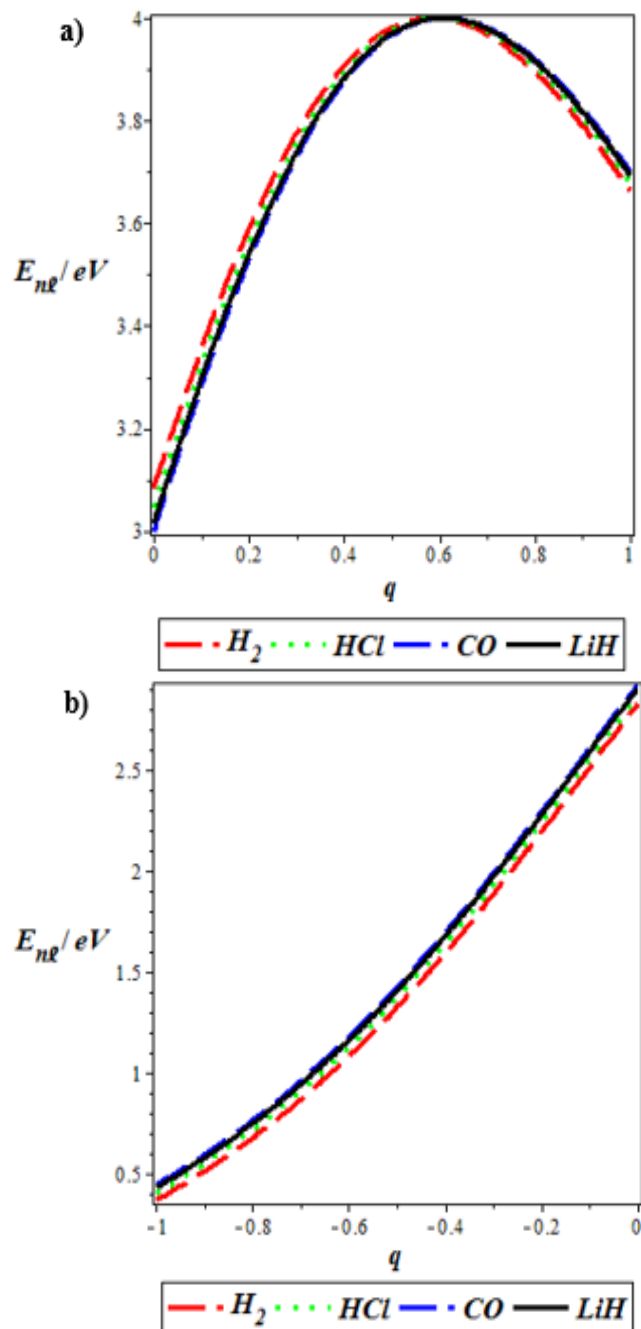
Figure 7. (a) The variation of the energy spectrum for various values of n as a function of the parameter $-q$. **(b)** The variation of the energy spectrum for various values of n as a function of the parameter $+q$. $a = 2$, $b = 1$, $c = -3$, $V_1 = 2$ and $V_0 = 3$.

6. Conclusion

In this work, the bound state solutions of the Schrödinger equation were studied with the *q*-deformed Hulthen-quadratic exponential-type potential using parametric NU method. The Greene and Aldrich approximation scheme was used to deal with the centrifugal term; the energy eigenvalues and the corresponding eigenfunctions were obtained and some special cases of the potential were also discussed. The energy spectrum is applied to study four selected diatomic molecules, H_2, HCl, CO and LiH. The effect of the deformation parameters and other potential parameters on the energy of the system were graphically and numerically analyzed. The results are in excellent agreement with literature. Finally, the results can find many applications in quantum mechanical systems, atomic and molecular physics.

Authors' contribution

Conceptualization: Obogo, U. P.; Ubi, O. E.
Data curation: Ikot, A. N.; Edet, C. O.
Formal Analysis: Edet, C. O.
Funding acquisition: Not applicable.
Investigation: Obogo, U. P.; Ubi, O. E.; Edet, C. O.; Ikot, A. N.
Methodology: Edet, C. O.
Project administration: Obogo, U. P.; Ubi, O. E.; Edet, C. O.; Ikot, A. N.
Resources: Edet, C. O.; Ikot, A. N.
Software: Edet, C. O.
Supervision: Obogo, U. P.; Edet, C. O.; Ikot, A. N.
Validation: Edet, C. O.; Ikot, A. N.
Visualization: Edet, C. O.; Ikot, A. N.
Writing – original draft: Obogo, U. P.; Ubi, O. E.
Writing – review & editing: Edet, C. O.; Ikot, A. N.

Data availability statement

All data sets were generated or analyzed in the current study.

Funding

Acknowledgments

References

Agboola, D. The Hulthén potential in *D*-dimensions. *Phys. Scr.* **2009**, *80* (6), 065304. https://doi.org/10.1088/0031-8949/80/06/065304

Bayrak, O.; Kocak, G.; Boztosun, I. Any *l*-state solutions of the Hulthén potential by the asymptotic iteration method. *J. Phys. A: Math. Gen.* **2006**, *39* (37), 11521. https://doi.org/10.1088/0305-4470/39/37/012

Ciftci, H.; Hall, R. L.; Saad, N. Asymptotic iteration method for eigenvalue problems. *J. Phys. A: Math. Gen.* **2003**, *36* (47), 11807. https://doi.org/10.1088/0305-4470/36/47/008

Ciftci, H.; Hall, R. L.; Saad, N. Perturbation theory in a framework of iteration methods. *Phys. Lett. A* **2005**, *340* (5–6), 388–396. https://doi.org/10.1016/j.physleta.2005.04.030

Dong, S.-H. *Factorization method in quantum mechanics*; Springer, 2007.

Durmus, A.; Yasuk, F. Relativistic and nonrelativistic solutions for diatomic molecules in the presence of double ring-shaped Kratzer potential. *J. Chem. Phys* **2007**, *126*, 074108. https://doi.org/10.1063/1.2566432

Ebomwonyi, O.; Onate, C. A.; Onyeaju, M. C.; Ikot, A. N. Any ℓ−states solutions of the Schrödinger equation interacting with Hellmann-generalized Morse potential model. *Karbala Intl. J. Mod. Sci.* **2017**, *3* (1), 59–68. https://doi.org/10.1016/j.kijoms.2017.03.001

Edet, C. O.; Okoi, P. O. Any *l*-state solutions of the Schrödinger equation for *q*-deformed Hulthen plus generalized inverse quadratic Yukawa potential in arbitrary dimensions. *Rev. Mex. Fis.* **2019**, *65* (4), 333–344. https://doi.org/10.31349/RevMexFis.65.333

Edet, C. O.; Okoi, P. O.; Chima S. O. Analytic solutions of the Schrödinger equation with non-central generalized inverse quadratic Yukawa potential. *Rev. Bras. Ensino Fís.* **2020a**, *42*, e20190083. https://doi.org/10.1590/1806-9126-rbef-2019-0083

Edet, C. O., Okorie, U. S., Ngiangia, A. T., Ikot, A. N. Bound state solutions of the Schrodinger equation for the modified Kratzer potential plus screened Coulomb potential. *Indian J. Phys.* **2020b**, *94*, 425–433. https://doi.org/10.1007/s12648-019-01477-9

Edet, C. O.; Amadi, P. O.; Okorie, U. S.; Tas, A.; Ikot, A. N.; Rampho, G. Solutions of Schrodinger equation and thermal properties of generalized trigonometric Poschl-Teller potential. *Rev. Mex. Fis.* **2020c**, *66* (6). https://doi.org/10.31349/RevMexFis.66.824

Edet, C. O.; Okorie, K. O.; Louis, H.; Nzeata-Ibe, N. A. Any *l*-state solutions of the Schrodinger equation interacting with Hellmann–Kratzer potential model. *Indian J. Phys.* **2020d**, *94*, 243–251. https://doi.org/10.1007/s12648-019-01467-x

Edet, C. O.; Okorie, U. S.; Osobonye, G.; Ikot, A. N.; Rampho, G. J.; Sever, R. Thermal properties of Deng–Fan–Eckart potential model using Poisson summation approach. *J. Math. Chem.* **2020e**, *58*, 989–1013. https://doi.org/10.1007/s10910-020-01107-4

Edet C. O.; Amadi, P. O.; Onyeaju, M. C.; Okorie, U. S.; Sever, R.; Rampho, G. J.; Abdullah, H. Y.; Salih, I. H.; Ikot, A. N. Thermal Properties and Magnetic Susceptibility of Hellmann Potential in Aharonov–Bohm (AB) Flux and Magnetic Fields at Zero and Finite Temperatures. *J. Low Temp. Phys.* **2021a**, *202*, 83–105. https://doi.org/10.1007/s10909-020-02533-z

Edet, C. O.; Ikot, A. N.; Onyeaju, M. C.; Okorie, U. S.; Rampho, G. J.; Lekala, M. L.; Kaya, S. Thermo-magnetic properties of the screened Kratzer potential with spatially varying mass under the influence of Aharanov-Bohm(AB) and position-dependent magnetic fields. *Physica E*. **2021b**, 131, 114710. https://doi.org/10.1016/j.physe.2021.114710

Falaye, B. J. Any ℓ-state solutions of the Eckart potential via asymptotic iteration method. *Cent. Eur. Phys.* **2012**, *10* (4), 960–965. https://doi.org/10.2478/s11534-012-0047-6

Falaye, B. J.; Oyewumi, K. J.; Ikhdair, S. M.; Hamzavi, M. Eigensolution techniques, their applications and Fisher's information entropy of the Tietz–Wei diatomic molecular model. *Phys. Scr.* **2014**, *89* (11), 115204. https://doi.org/10.1088/0031-8949/89/11/115204

Falaye, B. J.; Ikhdair, S. M.; Hamzavi, M. Energy States of Some Diatomaic Molecules: The Exact Quantisation Rule Approach. *Zeitschrift für Naturforschung A* **2015a**, *70* (2), 85–90. https://doi.org/10.1515/zna-2014-0232

Falaye, B. J.; Ikhdair, S. M.; Hamzavi, M. Formula Method for Bound State Problems. *Few-Body Syst.* **2015b**, 56, 63–78. https://doi.org/10.1007/s00601-014-0937-9

Greene, R. L.; Aldrich, C. Variational wave functions for a screened Coulomb potential. *Phys. Rev. A* **1976**, *14* (6), 2363. https://doi.org/10.1103/PhysRevA.14.2363

Greiner W. *Relativistic Quantum Mechanics: Wave equations*; Springer, 2000. https://doi.org/10.1007/978-3-662-04275-5

Gu, X.-Y.; Dong, S.-H. Energy spectrum of the Manning-Rosen potential including centrifugal term solved by exact and proper quantization rules. *J. Math. Chem.* **2011**, *49*, 2053. https://doi.org/10.1007/s10910-011-9877-5

Hall, R. L.; Saad, N.; Sen, K. D. Exact normalized eigenfunctions for general deformed Hulthén potentials. *J.*

Math. Phys. **2018**, *59*, 122103. https://doi.org/10.1063/1.5043484

Ikhdair, S. M. An improved approximation scheme for the centrifugal term and the Hulthén potential. *Eur. Phys. J. A* **2009**, *39*, 307–314. https://doi.org/10.1140/epja/i2008-10715-2

Ikhdair, S. M.; Sever, R. Approximate Eigenvalue and Eigenfunction Solutions for the Generalized Hulthén Potential with any Angular Momentum. *J. Math. Chem.* **2007**, *42*, 461–471. https://doi.org/10.1007/s10910-006-9115-8

Ikot, A. N.; Awoga, O. A.; Hassanabadi, H.; Maghsoodi, E. Analytical approximate solution of Schrödinger equation in *D* dimensions with quadratic exponential-type potential for arbitrary *l*-State. *Commun. Theor. Phys.* **2014**, *61* (4), 457. https://doi.org/10.1088/0253-6102/61/4/09

Ikot A. N.; Edet, C. O.; Amadi, P. O.; Okorie, U. S.; Rampho, G. J.; Abdullah, H. Y. Thermodynamic properties of Aharanov–Bohm (AB) and magnetic fields with screened Kratzer potential. *Eur. Phys. J. D* **2020a**, *74*, 159. https://doi.org/10.1140/epjd/e2020-10084-9

Ikot, A. N.; Okorie U. S.; Osobonye G.; Amadi P. O.; Edet C. O.; Sithole M. J.; Rampho G. J.; Sever R. Superstatistics of Schrödinger equation with pseudo-harmonic potential in external magnetic and Aharanov-Bohm fields. *Heliyon* **2020b**, *6* (4), e03738. https://doi.org/10.1016/j.heliyon.2020.e03738

Ita, B. I.; Louis, H.; Akakuru, O. U.; Nzeata-Ibe, N. A.; Ikeuba A. I.; Magu, T. O.; Amos, P. I.; Edet, C. O. Approximate Solution to the Schrödinger Equation with Manning- Rosen plus a Class of Yukawa Potential via WKBJ Approximation Method. *Bulg. J. Phys.* **2018**, 45, 323–333.

Jia, C.-S.; Liu, J.-Y.; Wang, P.-Q. A new approximation scheme for the centrifugal term and the Hulthén potential. *Phys. Lett. A* **2008**, *372* (27–28), 4779–4782. https://doi.org/10.1016/j.physleta.2008.05.030

Landau, L. D.; Lifshitz E. M. *Quantum Mechanics: Non-relativistic Theory*; Pergamon, 1977.

Louis, H.; Iserom, I. B.; Akakuru, O. U.; Nzeata-Ibe, N. A.; Ikeuba, A. I.; Magu, T. O.; Amos, P. I.; Collins, E. O. *l*-state Solutions of the Relativistic and Non-Relativistic Wave Equations for Modified Hylleraas-Hulthen Potential Using the Nikiforov-Uvarov Quantum Formalism. *Orient. J. Phys. Sciences* **2018a**, *3* (1).

Louis H.; Ita B. I.; Magu T. O.; Akakuru U. O.; Nzeata-Ibe, N.; Ikeuba I. A.; Amos I. P.; Edet C. O. Solutions to the Dirac Equation for Manning-Rosen Plus Shifted Deng-Fan Potential and Coulomb-Like Tensor Interaction Using Nikiforov-Uvarov Method. *Int. J. Chem.* **2018b**, *10* (3), 99–106. https://doi.org/10.5539/ijc.v10n3p99

Ma, Z.-Q.; Xu, B.-W. Quantum correction in exact quantization rules. *EPL (Europhysics Letters)* **2005**, *69* (5), 685. https://doi.org/10.1209/epl/i2004-10418-8

Nikiforov, A. F.; Uvarov, V. B. *Special Functions of Mathematical Physics*; Birkhäuser Verlag Basel, 1988.

Okoi, P. O.; Edet C. O.; Magu T. O. Relativistic treatment of the Hellmann-generalized Morse potential. *Rev. Mex. Fis.* **2020**, *66* (1), 1–13. https://doi.org/10.31349/RevMexFis.66.1

Okorie, U. S.; Ikot, A. N.; Onyeaju, M. C.; Chukwuocha, E. O. A study of thermodynamic properties of quadratic exponential-type potential in *D*-dimensions. *Rev. Mex. Fis.* **2018**, *64* (6), 608–614. https://doi.org/10.31349/RevMexFis.64.608

Okorie U. S.; Ikot A. N.; Edet C. O.; Rampho, G. J.; Server, R.; Akpan I. O. Solutions of the Klein Gordon equation with generalized hyperbolic potential in D-dimensions. *J. Phys. Commun.* **2019**, *3* (9), 095015. https://doi.org/10.1088/2399-6528/ab42c6

Okorie U. S.; Edet C. O.; Ikot A. N.; Rampho G. J.; Sever R., Thermodynamic functions for diatomic molecules with modified Kratzer plus screened Coulomb potential. *Indian J. Phys.* **2020**, 95, 411–421. https://doi.org/10.1007/s12648-019-01670-w

Onate, C. A.; Onyeaju, M. C.; Ikot, A. N.; Ojonubah J. O. Eigen solutions, Shannon entropy and fisher information under the Eckart Manning Rosen potential model. *J. Korean Phys. Soc.* **2017**, *70*, 339–347. https://doi.org/10.3938/jkps.70.339

Onate, C. A.; Adebimpe, O.; Adebesin, B. O; Lukman, A. F. Information-theoretic measure of the hyperbolical exponential-type potential. *Turk. J. Phys.* **2018a**, *42* (4), 402–414. https://doi.org/10.3906/fiz-1802-40

Onate, C. A.; Adebimpe, O.; Lukman, A. F.; Adama, I. J.; Okoro, J. O.; Davids, E. O. Approximate eigensolutions of the attractive potential via parametric Nikiforov-Uvarov method. *Heliyon* **2018b**, *4* (11), e00977. https://doi.org/10.1016/j.heliyon.2018.e00977

Onate, C. A.; Ikot, A. N.; Onyeaju, M. C.; Ebomwonyi, O.; Idiodi, J. O. A. Effect of dissociation energy on Shannon and Rényi entropies. *Karbala Int. J. Mod. Sci.* **2018c**, *4* (1), 134–142. https://doi.org/10.1016/j.kijoms.2017.12.004

Qiang, W.-C.; Dong, S.-H. Arbitrary *l*-state solutions of the rotating Morse potential through the exact quantization rule method. *Phys. Lett. A* **2007**, *363* (3), 169–176. https://doi.org/10.1016/j.physleta.2006.10.091

Rampho, G. J.; Ikot A. N.; Edet C. O.; Okorie U. S. Energy spectra and thermal properties of diatomic molecules in the presence of magnetic and AB fields with improved Kratzer potential. *Mol. Phys.* **2021**, *119* (5), e1821922. https://doi.org/10.1080/00268976.2020.1821922

Schiff L. I. *Quantum Mechanics*; McGraw Hill, 1995.

Tezcan, C.; Sever, R. A general approach for the exact solution of the Schrödinger equation. *Intl. J. Theor. Phys.* **2009**, *48*, 337–350. https://doi.org/10.1007/s10773-008-9806-y